

**Experimental Investigation of the Effect of Wall Adaptation on
Flow Over a Cylinder in a Modernized Adaptive-Wall Wind
Tunnel**

by

Michael J. Bishop

A thesis
presented to the University of Waterloo
in fulfillment of the
thesis requirement for the degree of
Master of Applied Science
in
Mechanical Engineering

Waterloo, Ontario, Canada, 2010

© Michael J. Bishop 2010

I hereby declare that I am the sole author of this thesis. This is a true copy of the thesis, including any required final revisions, as accepted by my examiners.

I understand that my thesis may be made electronically available to the public.

Abstract

A renovation of an adaptive-wall wind tunnel was completed to improve flow quality, automate data acquisition, integrate a three-axis traversing mechanism, and regain functionality of an adaptive-wall test section. Redesign of the settling chamber significantly improved flow quality, with the resulting turbulence intensity of 0.3% and flow uniformity of $\pm 0.6\%$ matching characteristics of research-grade wind tunnels. The functionality of the adaptive-wall test section was tested by analyzing the effect of wall adaptation on flow development over a circular cylinder. Experiments were carried out for a Reynolds number (Re_d) of 57,000 for three blockage ratios: 5%, 8%, and 17%. Measurements were made in three wall configurations: geometrically straight walls (GSW), aerodynamically straight walls (ASW), and streamlined walls (SLW). Solid blockage effects were clearly evident in cylinder surface pressure distributions for the GSW and ASW configurations, manifested by an increased peak suction and base suction. Upon streamlining the walls, pressure distributions for each blockage ratio matched distributions expected for low blockage ratios. Wake blockage limited wake growth in the GSW configuration at 7.75 and 15 diameters downstream of the cylinder for blockages of 17% and 8%, respectively. This adverse effect was rectified by streamlining the walls with the resulting wake width development matching that expected for low blockage ratios. Wake vortex shedding frequency and shear layer instability frequency increased in the GSW and ASW configurations with increasing blockage ratio. Invariance of the near wake width with wall configuration suggests that frequency increase is caused by the increased velocity due to solid blockage effects. For all the blockage ratios investigated, the increased wake vortex shedding frequency observed in the ASW and GSW configurations was corrected in the SLW configuration, with the resulting Strouhal numbers of about 0.19, matching that expected for low blockage ratios at the investigated Re_d .

Acknowledgments

First of all, I would like to thank my family for their love and support, not only through my Masters Degree, but throughout my entire academic career. In addition to my family, I would like to acknowledge several people for the unique support that they provided me.

To my supervisor, Professor Serhiy Yarusevych, thank you for your constant support, technical guidance, and thorough editorial services.

To the technical staff at the University of Waterloo, specifically, Jim Merli, Andy Barber, John Potzold, Kwai Chan, and John Boldt, thank you for help in the development of my experimental setup.

To my fellow graduate students, specifically, Chris, Sina, Mike, and Stephen, thank you for all your support and willingness to lend a helping hand.

To my fellow graduate student, Ryan Gerakopolus, thank you for your essential help in the extensive modifications to the wind tunnel. Thank you for all the good times we enjoyed and inevitable challenging times we traversed through. Your hard work, skills, and attention to detail never went unnoticed – thank you.

Finally, thank you to the Ontario Graduate Scholarship Program, Natural Sciences and Engineering Research Council, and the University of Waterloo for their financial support required for my research.

Table of Contents

Authors Declaration.....	ii
Abstract.....	iii
Acknowledgments	iv
Table of Contents	v
List of Figures.....	vii
List of Tables	x
Nomenclature	xi
1 Introduction.....	1
1.1 The Need for Experimental Data	1
1.2 Wind Tunnel Flow Conditioning	2
1.3 Types of Wind Tunnel Blockage	5
1.3.1 Solid Blockage	5
1.3.2 Wake Blockage	6
1.3.3 Horizontal Buoyancy	6
1.4 Methods to Alleviate Blockage Effects.....	7
1.4.1 Post Test Correction Methods.....	7
1.4.2 Specialized Test Sections.....	8
1.5 Objectives.....	10
2 Background: Flow over a Cylinder	11
2.1 Flow Over a Cylinder.....	11
2.2 The Effects of Blockage on Flow over a Cylinder.....	16
2.3 Adaptive-Wall Studies for External Flows	19
3 Experimental Apparatus	22
3.1 University of Waterloo Adaptive-Wall Wind Tunnel.....	22
3.2 Flow Quality Assessment and Settling Chamber Modifications	24
3.3 Velocity Measurements.....	26
3.4 Automated Traverse	28
3.5 Wall Pressure Measurements	29
3.6 Cylinder Model and Model Pressure Measurements	31
3.7 Geometrically Straight Walls (GSW)	33
4 Wall Adaptation Strategy.....	35

4.1	Aerodynamically Straight Walls (ASW).....	35
4.2	Predictive Wall Adaptation Strategy (WAS)	38
4.3	Streamlining Results	43
5	Experimental Results.....	50
5.1	Mean Pressure Distributions on Cylinder and Drag.....	50
5.2	RMS Pressure Distributions on Cylinder	58
5.3	Mean Wake Development.....	59
5.4	RMS Wake Velocity Profiles.....	71
5.5	Vortex Formation Region.....	77
5.6	Wake Vortex Shedding Frequency	81
5.7	Shear Layer Instability Frequency	88
6	Conclusions.....	92
7	Recommendations	95
	References.....	97
	Appendices	
	Appendix A: Settling Chamber Modifications.....	102
	Appendix B: Measurement and Automation	107
	Appendix C: MATLAB Code	114
	Appendix D: Experimental Uncertainty Analysis	136

List of Figures

Figure 2.1 Regions of disturbed flow for a circular cylinder: a) retarded flow, b) accelerated flow, and c) wake.	11
Figure 2.2 Common surface pressure distribution for a circular cylinder (Okamoto & Takeuchi, 1975).	14
Figure 2.3 Cylinder wake definition.	16
Figure 2.4 Pressure coefficient distributions at various blockage ratios for $Re_d = 32,200$ (Okamoto & Takeuchi, 1975).	17
Figure 2.5 Wake width growth at various blockage ratios (Okamoto & Takeuchi, 1975).	18
Figure 3.1 University of Waterloo Adaptive-Wall Wind Tunnel.	22
Figure 3.2 Hardware schematic for wall pressure measurements.	30
Figure 3.3 Cylinder coordinate system.	33
Figure 3.4 Test section wall configurations.	34
Figure 4.1 Wall pressure distributions in an empty test section for the nominal wall configuration.	37
Figure 4.2 Wall pressure distributions in an empty test section for the contracted wall configuration.	37
Figure 4.3 Flow division for wall-adaptation strategy.	38
Figure 4.4 Wall streamlining procedure (Wolf, 1995).	40
Figure 4.5 Wall pressure distributions in the GSW, ASW, and SLW configurations for a) $B=17\%$,	47
Figure 4.6 Wall deflections from GSW in the ASW and SLW configurations for a) $B=17\%$, b) $B=8\%$, and c) $B=5\%$	48
Figure 4.7 Streamwise velocity measured outside the wake for a) $B=17\%$, b) $B=8\%$, and c) $B=5\%$	49
Figure 5.1 Mean cylinder surface pressure coefficient distributions in the GSW, ASW, and SLW configurations for a) $B=17\%$, b) $B=8\%$, and c) $B=5\%$	51
Figure 5.2 Mean cylinder surface pressure coefficient distributions in the SLW configuration for $B=17\%$, 8% , and 5%	57
Figure 5.3 RMS surface pressure coefficient distribution in the GSW, ASW, and SLW configurations for $B=17\%$	59
Figure 5.4 Mean velocity profiles from cross-wire probe for $B=17\%$ in the a) GSW, b) ASW, and c) SLW configurations.	61
Figure 5.5 Mean velocity profiles from cross-wire probe for $B=8\%$ in the a) GSW, b) ASW, and c) SLW configurations.	62

Figure 5.6 Mean velocity profiles from cross-wire probe for B=5% in the a) GSW and b) SLW configurations.	63
Figure 5.7 Mean half wake width growth for B=5% in the GSW and SLW configurations..	64
Figure 5.8 Mean half wake width growth for B=17% in the GSW, ASW, and SLW configurations.	65
Figure 5.9 Mean half wake width growth for B=8% in the GSW, ASW, and SLW configurations.	65
Figure 5.10 Characteristic wake velocity deficits.....	67
Figure 5.11 Mean wake streamwise velocity profiles at $x/d = 1.5$ in the GSW, ASW, and SLW configurations for a) B=17%, b) B=8%, and c) B=5%.	69
Figure 5.12 Mean wake vertical velocity profiles at $x/d = 1.5, 2.5,$ and 4.0 in the GSW, ASW, and SLW configurations for a) B=17%, b) B=8%, and c) B=5%.....	70
Figure 5.13 Streamwise RMS velocity profiles for B=17% in the a) GSW, b) ASW, and c) SLW configurations.	72
Figure 5.14 Streamwise RMS velocity profiles for B=8% in the a) GSW, b) ASW, and c) SLW configurations.	73
Figure 5.15 Streamwise RMS velocity profiles for B=5% in the a) GSW and b) SLW configurations.	74
Figure 5.16 Streamwise RMS velocity profiles for B=17% in the GSW, ASW, and SLW configurations.	75
Figure 5.17 Streamwise RMS velocity profiles for B=8% in the GSW, ASW, and SLW configurations.	75
Figure 5.18 Streamwise RMS velocity profiles for B=5% in the GSW and SLW configurations.	75
Figure 5.19 Vertical RMS velocity profiles for B=17% in the GSW, ASW, and SLW configurations.	76
Figure 5.20 Vertical RMS velocity profiles for B=8% in the GSW, ASW, and SLW configurations.	76
Figure 5.21 Vertical RMS velocity profiles for B=5% in the GSW, ASW, and SLW configurations.	76
Figure 5.22 Evaluation of centerline streamwise RMS velocity with x/d in the GSW, ASW, and SLW configurations for a) B=17%, b) B=8%, and c) B=5%.....	80
Figure 5.23 Velocity spectra for B=17% at $x/d=2.5, y/d=0.5$ based on a) streamwise fluctuating component and b) vertical fluctuating component.	82
Figure 5.24 Velocity spectra for B=8% at $x/d=2.5, y/d=0.5$ based on a) streamwise fluctuating component and b) vertical fluctuating component.	83
Figure 5.25 Velocity spectra for B=5% at $x/d=2.5, y/d=0.5$ based on a) streamwise fluctuating component and b) vertical fluctuating component.	84

Figure 5.26 Strouhal number variation for all wall configurations and blockage ratios investigated.	86
Figure 5.27 Comparison of a) velocity spectrum at $x/d=2.5$ and $y/d=0.5$ and b) pressure spectrum at $\theta=82^\circ$ in the SLW configuration for $B=17\%$	87
Figure 5.28 Velocity spectra obtained in the separated shear layer for the GSW, ASW, and SLW configurations at $x/d = 0.25$, $y/d = 0.62$	89
Figure 5.29 Normalized shear layer instability frequency for the GSW, ASW, and SLW configurations.	91
Figure A.1 Original settling chamber.	102
Figure A.2 Free-stream vertical velocity profile in the original settling chamber at $U_o=15$ m/s.....	103
Figure A.3 New settling chamber.	104
Figure A.4 Free-stream vertical velocity profile in the new settling chamber at $U_o=15$ m/s.....	106
Figure B.1 Typical hot-wire calibration curves for a) normal probe (U vs E), b) cross-wire probe (UE1 vs E1), and c) cross-wire probe (UE2 vs E2).....	108
Figure B.2 Free-stream velocity calibration curves in the a) nominal and b) contracted test sections.....	109
Figure B.3 Drawing summary for wind tunnel control system.	110
Figure B.4 Stepper motor drives for three-axis traverse.....	111
Figure B.5 Electrical housing for ZOC33 hardware.....	112
Figure B.6 Solid state relay board for ZOC33 operation mode selection.....	113
Figure C.1 Flow chart of wall adaptation strategy.....	114

List of Tables

Table 3.1 Estimates of maximum hot-wire errors (Kawall et al., 1983)	28
Table 3.2 Test matrix.	34
Table 5.1 Base pressure coefficient summary for B=17%, 8%, and 5% in the GSW, ASW, and SLW configurations.	53
Table 5.2 Angle of separation summary for B=17%, 8%, and 5% in the GSW, ASW, and SLW configurations.	54
Table 5.3 Pressure drag coefficients summary for B=17%, 8%, and 5% in the GSW, ASW, and SLW configurations.	55
Table 5.4 Summary of RMS surface pressure coefficient distributions in the GSW, ASW, and SLW configurations for B=17%.	59
Table 5.5 Vortex formation lengths for all blockage ratio and wall configuration combinations.	78
Table 5.6 Strouhal numbers for all wall configurations and blockage ratios investigated.	85
Table 5.7 Shear layer instability frequencies for all wall configurations and blockage ratios investigated.	90
Table A.1 Characteristics of screens in original settling chamber.....	102
Table A.2 Characteristics of screens in new settling chamber.	105
Table D.1 List of pressure transducers used in experiment.	137
Table D.2 Total uncertainty associated with free-stream speed and pressure measurements.	138
Table D.3 Error estimates for velocity measurements.....	139

Nomenclature

ASW	aerodynamically straight walls
B	model blockage ratio, d/h
Bi	Bias error
C_p	surface pressure coefficient, $(P-P_o)/(0.5\rho U_o^2)$
C_{pw}	wall surface pressure coefficient, $(P_w-P_o)/(0.5\rho U_o^2)$
C_p'	surface pressure coefficient based on RMS pressure fluctuations
d	cylinder diameter [m]
d_w	screen wire diameter [mm]
E_{pp}	normalized energy spectrum of p
E_{uu}	normalized energy spectrum of u
E_{vv}	normalized energy spectrum of v
f_v	vortex shedding frequency [Hz]
f_{sl}	shear layer instability frequency [Hz]
f_t	turbulence reduction factor
GSW	geometrically straight walls
h	vertical height of the test section with GSW [m]
K	screen pressure drop coefficient
L	test section length [m]
M	screen mesh spacing [mm]
Ma	mach number
P	mean pressure on cylinder surface [Pa]
p	fluctuating pressure on cylinder surface [Pa]
P_o	free-stream static pressure [Pa]
P_w	mean pressure along test section walls [Pa]
r	correlation coefficient
Re_d	Reynolds number based on cylinder diameter, $U_o d/\nu$
Re_{dw}	Reynolds number based on screen wire diameter, $U_o d_w/\nu$
RMS	Root Mean Square
S	Precision error
St	Strouhal number based on f_v , $f_v d/U_o$

SLW	streamlined walls
T_u	turbulence intensity
U_o	free-stream velocity in x direction [m/s]
U_o^*	streamwise velocity at edge of wake [m/s]
U	streamwise mean velocity [m/s]
u	streamwise fluctuating velocity component [m/s]
u'	RMS of streamwise velocity [m/s]
U_x	real flow field velocity [m/s]
V	vertical mean velocity [m/s]
v	vertical fluctuating velocity component [m/s]
v'	RMS of vertical velocity [m/s]
V_x	imaginary flow field velocity [m/s]
x, y	streamwise and vertical coordinates, respectively [m]
β	screen open area ratio
ρ	density of air [kg/m ³]
θ	positive angle measured from stagnation point of cylinder [°]
ν	kinematic viscosity of air [m ² /s]

1 Introduction

1.1 The Need for Experimental Data

Fundamental research in fluid mechanics and the development of relevant engineering applications rely extensively on experimental testing (e.g., Pope, 1966). In addition to its significance in engineering design, experimental data also serve to validate the results from computational fluid dynamics (CFD) simulations, the counter-part to experimental fluid mechanics. Rising computing power has allowed for an increase in complexity and apparent accuracy of CFD-based models. This, in turn, has placed an added emphasis on the need for high quality experimental data required for validation.

In fluid mechanics, the combinations of experiments and facilities are broad. This study is focused on testing of external flows conducted in a wind tunnel, which is one of the most common testing facilities. Ideally, to experimentally model flow around an object, tests have to be performed in an infinitely large flow field. In reality, however, fluid mechanic experiments are usually conducted within the confines of a testing facility, e.g., a closed test section of a wind tunnel. The presence of test section walls gives rise to blockage effects, which can adversely affect experimental data. In addition, parameters such as, free-stream turbulence intensity and flow uniformity, inherent to testing facilities, can influence the flow around a given model. Depending on the severity of these influencing parameters, flow development in a testing facility can deviate appreciably from what would occur in an unbounded flow.

This thesis is focused on two central topics: i) wind tunnel flow conditioning and ii) mitigation of blockage effects. More specifically, a design was developed for an inlet section

of an existing wind tunnel to reduce free-stream turbulence intensity and improve free-stream uniformity. Secondly, the effect of blockage on flow development over a circular cylinder was investigated. The circular cylinder was chosen since this relatively simple geometry, common to many engineering applications, has been studied extensively in the past (e.g., see reviews by Roshko, 1993; Williamson, 1996; Norberg, 2003).

1.2 Wind Tunnel Flow Conditioning

The wind tunnel is one of the most common experimental testing facilities for the testing of fluid flow (e.g., Pope, 1966; Tavoularis, 2005). The quality of results from experimental measurements obtained around a model in a wind tunnel is dependent on the quality of the free-stream flow. Assuring a high quality free-stream flow is of particular interest for investigations of external flows involving separated shear layers, e.g., separation on a wing, or wake of a bluff body (Mehta & Bradshaw, 1979). The quality of the flow in a wind tunnel is mainly characterized by two features, namely, flow uniformity and turbulence intensity. Along with wind tunnel geometry, such as contraction ratio, these flow features are controlled by turbulence manipulating devices, which are usually located upstream of the test section. The two most effective turbulence manipulators are honeycomb and mesh screens, each of which serves a specific purpose (Mehta & Bradshaw, 1979).

The main function of the honeycomb is to reduce transverse velocity fluctuations in the incoming flow, which are especially prevalent in open-return wind tunnels. Relative to the mesh screens, the pressure drop across the honeycomb is small. Ideally, the size of each cell within the honeycomb should be smaller than the expected transverse length scale of incoming flow structures. Although this length scale is difficult to measure, it is

recommended by Mehta & Bradshaw (1979) that the optimal ratio of cell length to height should be in the range of 5-8.

A main function of a mesh screen is to induce a significant pressure drop, which serves to improve flow uniformity. In addition, the mesh screen generates fine scale turbulence that acts to enhance dissipation of turbulent kinetic energy, resulting in an overall decrease in turbulence intensity after a particular downstream distance from the screen. Important physical parameters of a screen are its wire diameter (d_w), mesh spacing (M), and open area ratio (β). Several investigations have been dedicated to studying the effect of screen geometry on flow, e.g., Corrsin (1963), Laws & Livesey (1978), Tan-Atichat & Najib (1982), and Groth & Johansson (1988). Screens that operate above the laminar flow regime ($Re_{dw} > 40$) generate turbulence immediately downstream of the mesh followed by a region of turbulence decay. Tan-Atichat & Najib (1982) conducted a study to identify the length of the turbulence decay region as a function of the Reynolds number (Re_{dw}). Downstream of the turbulence decay region, the turbulence intensity is below that in the free-stream. Thus, care must be taken to ensure that the spacing between consecutive screens is greater than the turbulence decay region over the whole range of achievable Re_{dw} in a given facility.

The reduction in turbulence intensity for flow through a screen is a function of the screen's pressure drop coefficient (K), which can be calculated using the following formula developed by Wieghardt (1953), as recommended by Bradshaw & Mehta (2003).

$$K = 6.5 \left(\frac{1-\beta}{\beta^2} \right) \left(\frac{Ud}{\beta\nu} \right)^{-\frac{1}{3}} \quad (1.1)$$

Turbulence reduction increases with the pressure drop coefficient. As shown in Eq. 1.1., K increases with decreasing β ; however, Bradshaw & Mehta (2003) state that for $\beta < 0.58$ flow

non-uniformities start to develop. Therefore, optimal turbulence reduction is achieved when multiple screens of relatively high open area ratio ($\beta > 0.58$) are utilized in series. The level of turbulence reduction of an individual turbulence manipulating device is classified by the turbulence reduction factor (f_t). This factor is defined by the ratio of downstream to upstream turbulence intensities measured relative to the turbulence manipulating device (Eq. 1.2).

$$f_t = \frac{Tu_{\text{downstream}}}{Tu_{\text{upstream}}} \quad (1.2)$$

Correlations have been developed by Prandtl (1933) and Dryden & Schubauer (1947), to predict turbulence reduction factors as a function of the screen pressure drop coefficient. For turbulence manipulators in series, Scheiman & Brooks (1981) experimentally compared several turbulence reduction factor correlations and found that the relationship developed by Prandtl (1933) most closely agrees with experimental results for estimating the reduction in streamwise turbulence intensity. Using this relationship, the turbulence reduction factor for two turbulence manipulators (A and B) in series is given by Eq 1.3. It should be noted that turbulence manipulators, A and B, could be either honeycomb or a screen.

$$f_{t,AB} = \left(\frac{1}{1 + K_A} \right) \left(\frac{1}{1 + K_B} \right) \quad (1.3)$$

Given the relationships discussed above, the performance of a screen can be assessed based solely on screen geometry and free-stream speed. Previous studies (e.g., Scheiman & Brooks, 1981; Mehta & Bradshaw, 1979) suggest, however, that a critical factor influencing screen performance is the quality of the installed screen, which is determined by uniformity of the

mesh and the uniformity of tension across the screen's area. Also, in a practical sense, screens must be cleaned regularly to avoid a decrease in β and the flow non-uniformities associated with $\beta < 0.58$. Pertinent information regarding flow conditioning for the current study can be found in Appendix A.

1.3 Types of Wind Tunnel Blockage

In a closed test section, the presence of walls influences the flow around the model. The magnitude of wall effects on experimental data scales with blockage ratio (Pope, 1966). Model blockage ratio (B) is defined as the ratio of model projected area to the cross-sectional area of the test section. For a circular cylinder, the blockage ratio (B) is the ratio of cylinder diameter (d) to test section height (h). Understanding the effects of blockage and methods to avoid them and/or correct the experimental data is of extreme importance in experimental fluid mechanics. The three most common types of blockage are solid blockage, wake blockage, and longitudinal (or horizontal) buoyancy (Tavoularis, 2005).

1.3.1 Solid Blockage

When a model is mounted in a closed test section of a wind tunnel, the open area of the test section is reduced in the locations above and below the model. By continuity, the velocity in these local areas is in excess of the free-stream velocity observed at a location well upstream of the model. The increase in local velocity alters the pressure distribution along the surface of the model, which yields a bias in aerodynamic forces. For example, solid blockage increases drag and moments about the model (Tavoularis, 2005). Although always present,

solid blockage can be minimized by reducing the size of experimental models relative to the test section dimensions.

1.3.2 Wake Blockage

The region of retarded flow downstream of a model is referred to as the wake. In an unbounded flow, the width of the wake increases with downstream location, until the free-stream velocity is recovered. However, in a closed test section, the physical presence of walls can alter the wake development. Specifically, the presence of walls acts to speed up flow outside the wake and to decrease pressure in it (Pope, 1966). In addition, solid walls limit the wake growth (Okamoto & Takeuchi, 1975). The combined effect of these phenomena is referred to as wake blockage (Pope, 1966). The effect of wake blockage becomes more pronounced when high-drag models are tested, since they produce a wide wake. Thus, it is important to account for wake blockage in studies concerned with wake development of bluff bodies (e.g., a circular cylinder).

1.3.3 Horizontal Buoyancy

A boundary layer develops on each wall in a closed test section. The height of the boundary layer, which grows with increasing streamwise distance, effectively reduces the core cross-sectional area of the free-stream flow. The reduction in core area causes a velocity increase, which yields a negative pressure gradient along each wall. This gives rise to a blockage effect, referred to as horizontal buoyancy (Pope, 1966). A consequence of the pressure drop between a location upstream and a location downstream of the model is an increase in drag. Tavoularis (2005) refers to this drag increase as “longitudinal buoyancy drag” or “buoyancy drag”. For a fixed test section height, the effects of horizontal buoyancy become more

pronounced at low Reynolds numbers, since the rate of boundary layer growth increases with decreasing velocity.

1.4 Methods to Alleviate Blockage Effects

1.4.1 Post Test Correction Methods

The discussed blockage effects are common to most wind tunnel facilities and have to be accounted for. As previously mentioned, blockage effects can be minimized by using small models relative to the test section dimensions. This approach, however, is not ideal since it limits the effective range of Reynolds numbers achievable in a given facility. Another method to account for blockage effects is to implement post-test data correction methods (Pope, 1966). To eliminate all effects of blockage, a post-test correction method would have to account for all blockage types; namely, solid blockage, wake blockage, and horizontal buoyancy. Early correction models, such as a pioneering model by Fage (1929), were aimed to accommodate only for solid blockage effects (Zdravkovich, 2003). Subsequent correction methods, which started to account for wake blockage, are Allen & Vincenti's (1948) source model and Maskell's (1963) correction method. Allen & Vincenti's model is based on potential flow theory and involves replacing the model and its wake by a source at the model location, while replacing the walls with a series of sources separated by the test section height. Conversely, Maskell's correction method is based on momentum balance and relies on empirically developed factors. Modi & El-Sherbiny (1971) implemented these correction methods for a range of blockage ratios for flow over a circular cylinder and concluded that drag was corrected adequately only when blockage ratios were less than 20%. Thus, there are limitations on the implementation of post-test correction methods. Although the limitation

and accuracy of the post-test correction methods are debated between researchers (West & Apelt, 1982; Modi & El-Sherbiny, 1971; Zdravkovich, 2003), West and Apelt (1982) indicate that common blockage correction methods cannot adequately correct measured pressure distributions over a cylinder for blockage ratios greater than 6%.

1.4.2 Specialized Test Sections

An alternative method to minimize blockage effects involves building facilities with specialized test sections. The discussion of specialized facilities aimed to minimize blockage effects is limited here to closed test section wind tunnels, since open-jet test section wind tunnels do not have walls to create blockage. Aerodynamic measurements in an open-jet test section design are not void of experimental error however, as flow entrainment from outside of the test section jet yields an underestimation of aerodynamic forces (Pope, 1966). Examples of specialized facilities for closed-section wind tunnels are those that incorporate ventilated test sections or adaptive-wall test sections. The fundamental difference between ventilated and adaptive-wall test sections is that the former is a passive design and the latter is active (Wolf, 1995). Ventilated test sections are simply slotted or perforated to alleviate some interference at wall boundaries. There is no manipulation of the walls required during a test. Adaptive-wall wind tunnels, on the other hand, require an algorithm to actively configure walls based on model-specific measured wall interferences. For both types of facilities, the aim is to manipulate flow at the wall boundaries so as to mimic the conditions of an unbounded flow.

The original concept of streamlining wind tunnel walls originated at the National Physical Laboratory in England, and the first adaptive test section was built in 1938 (Ewald, 1998). Progress in adaptive-wall research continued until the 1950's, at which point

researchers slowed the development of the technology due to the extensive hardware and labour required for its operation. Instead, attention was shifted to ventilated test sections, since the method was inherently simpler due to its passive nature (Wolf, 1995). By the mid 1960's to 1970's the need for high quality experimental data was prevalent, and attention was moved back to adaptive-wall research. Since it involves non-trivial computations, the resurgence of adaptive-wall technology was made possible by advancements in computing power. One of the most notable contributions in the field was made by Judd (e.g., Judd et al., 1981), who developed the first predictive wall adjustment strategy. Throughout the 1980's and 1990's several institutions built wind tunnel sections with adaptive-walls (Ewald, 1998). The most common wall adaptation strategy used was that developed by Wolf & Goodyer (1988). Wolf (1995) listed details of 23 adaptive-wall wind tunnels currently in operation throughout the world. Included in that list was the University of Waterloo Adaptive-Wall Wind Tunnel, which at the time had the longest adaptive-wall test section.

Recently, Meyer & Nitsche (2004) developed a hybrid technique, referred to as 'Adaptive Slots'. This technique is a combination of the adaptive-wall and ventilated test section techniques. The adaptive slot approach incorporates four slotted test section walls and two flexible liners to allow wall adaptation. A disadvantage of conventional slotted tunnel designs is that, while wall interference is reduced, residual wall interference typically remains due to the lack of active control. Meyer & Nitsche (2004) indicate that conventional slotted test sections can be modified to incorporate adaptive slots, and thus eliminate residual wall interference. To this day, adaptive wall technologies have been mostly limited to research institutions and have yet to enter the large-scale applications of industry (Ewald, 1998).

1.5 Objectives

The success of any experimental investigation is dependent on the adequacy of the experimental setup. Prior to this work, the latest graduate experiment conducted in the University of Waterloo Adaptive-Wall Wind Tunnel was in 1994 (16 years ago). To that end, it was necessary to implement upgrades aimed at improving flow quality in the wind tunnel and install modern software and hardware to utilize the adaptive-wall test section. With an adaptive-wall strategy implemented, its functionality had to be proven. For this purpose, the study of flow over a circular cylinder was selected as this geometry has important practical engineering applications and is well studied. Specifically, the two objectives of this thesis are to:

- 1) Upgrade the existing wind tunnel to a modern research-grade testing facility
 - i. Improve flow quality:
 - Streamwise Turbulence Intensity $< 0.5\%$
 - Flow Uniformity within $\pm 1.0\%$ or better
 - ii. Automate velocity and wall pressure measurements
 - iii. Implement an adaptive-wall strategy to utilize the functionality of the adaptive-wall test section.

- 2) Identify the effect of wall adaptation on the flow development over a circular cylinder.

2 Background: Flow over a Cylinder

2.1 Flow Over a Cylinder

The goal of this section is to provide a basic background of flow over a circular cylinder so as to establish a reference for the second objective, which is to identify the effect of wall-adaptation on the very flow development described in this section. The short review provided here is by no means exhaustive, and the reader is referred to more extensive reviews by Roshko (1993), Williamson (1996), Zdravkovich (1997, 2003), and Norberg (2003).

Flow over a circular cylinder is common to many engineering applications. Examples range from flows over cylindrical support beams, such as structural columns in an off-shore oil rig or the tower of a wind turbine, to flows over heat exchanger tubes. As a free-stream flow passes over a cylindrical body, distinguishable regions of disturbed flow can be identified. Following the classification proposed by Zdravkovich (1997), these regions are shown in Fig. 2.1.

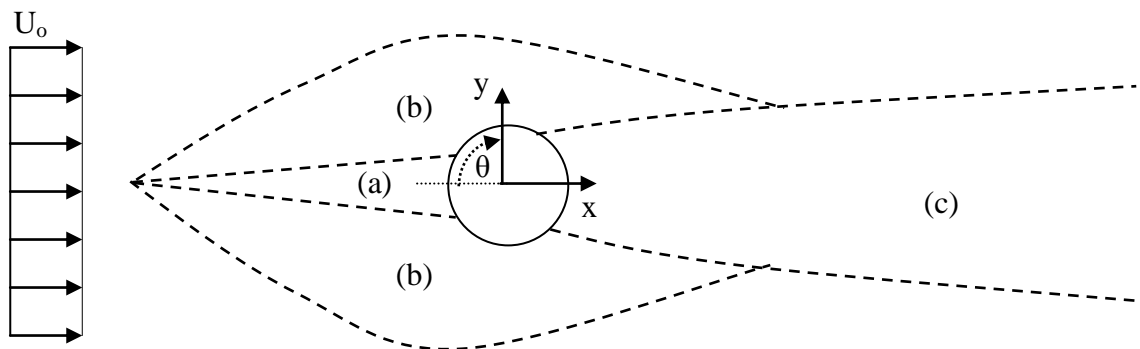


Figure 2.1 Regions of disturbed flow for a circular cylinder: a) retarded flow, b) accelerated flow, and c) wake.

The region (a), immediately in front of the cylinder, is characterized by retarded flow, i.e., $U < U_o$. The incoming flow stagnates at the front of the cylinder surface, so that pressure on the surface of the cylinder at $\theta = 0^\circ$ is equal to the stagnation pressure. In region (b), flow is accelerated ($U > U_o$), as it is being deflected by the cylinder. A boundary layer is formed on the surface of the cylinder starting from the stagnation point. The boundary layer eventually faces an adverse pressure gradient, and flow separates from the surface of the cylinder. As a result, a region of retarded flow forms behind the cylinder, which is referred to as the wake and is marked (c) in Fig. 2.1.

The distinct behavior of the flow in the described regions is reliant on flow being laminar, turbulent, or in a transitional state, which is dependent on the Reynolds number (Re_d) (Zdravkovich, 1997). As originally observed by Roshko & Fiszdon (1969), distinct flow regimes can be identified based on Re_d . These flow regimes are briefly discussed here and a more detailed discussion can be found in Williamson (1996) and Zdravkovich (1997).

At low Reynolds numbers ($5 < Re_d < 49$), flow separates from the cylinder and a closed wake forms containing two recirculating eddies above and below the cylinder axis. This regime is referred to as the laminar closed wake regime (Zdravkovich, 1997) or laminar steady regime (Williamson, 1996). As the Reynolds number is increased ($49 < Re_d < 200$), the wake becomes unstable resulting in periodic laminar vortex shedding (Zdravkovich, 1997). The two rows of staggered eddies are collectively referred to as the von-Karman vortex street (Zdravkovich, 1997; Williamson, 1996). For Reynolds numbers $200 < Re_d < 400$, transition to turbulence occurs in the wake, however, wake vortex shedding persists. For $400 < Re_d < 200,000$ transition to turbulence occurs in the separated shear layers (Zdravkovich, 1997). Within this flow regime, shear layer instability causes roll-up of the

shear layer into transition eddies (Bloor, 1964). For $Re_d > 200,000$, transition occurs in the attached boundary layer on the surface of the cylinder (Zdravkovich, 1997). The turbulent boundary layer is more resilient to the adverse pressure gradient, resulting in the separation point moving downstream and the pressure drag decreasing significantly (Williamson, 1996). This flow regime is commonly referred to as the supercritical regime (Williamson, 1996).

The primary focus of this study is on the shear layer transition regime, as this regime pertains to a wide range of Reynolds numbers ($400 < Re_d < 200,000$) and is common to many engineering applications (Norberg, 2003). The development of the turbulent wake and the associated flow structures are of particular interest. For example, large alternating lateral forces are created due to vortex shedding, which is of critical importance in structural design (Williamson, 1996).

By analyzing the pressure distribution on the surface of the cylinder, the location of separation can be estimated and pressure drag can be calculated. The measured pressure distribution is commonly represented by the pressure coefficient (C_p) distribution, with C_p given by Eq. 2.1:

$$C_p = \frac{P - P_o}{\frac{1}{2}\rho U_o^2} \quad (2.1)$$

where P is the surface pressure, ρ is air density, P_o and U_o are the free-stream static pressure and velocity, respectively. A common surface pressure distribution on a circular cylinder for $Re_d = 32,000$ (Okamoto & Takeuchi, 1975) is contrasted with that from potential flow theory in Fig. 2.2. Maximum suction, i.e., minimum pressure, occurs around $\theta \approx 70^\circ$. Downstream, flow separates at an angle which can be identified by an inflection point on the C_p curve

(Zdravkovich, 1997). The exact location of flow separation varies with Re_d , being within the range of $70^\circ < \theta < 81^\circ$ for a laminar separation (Okamoto & Takeuchi, 1975).

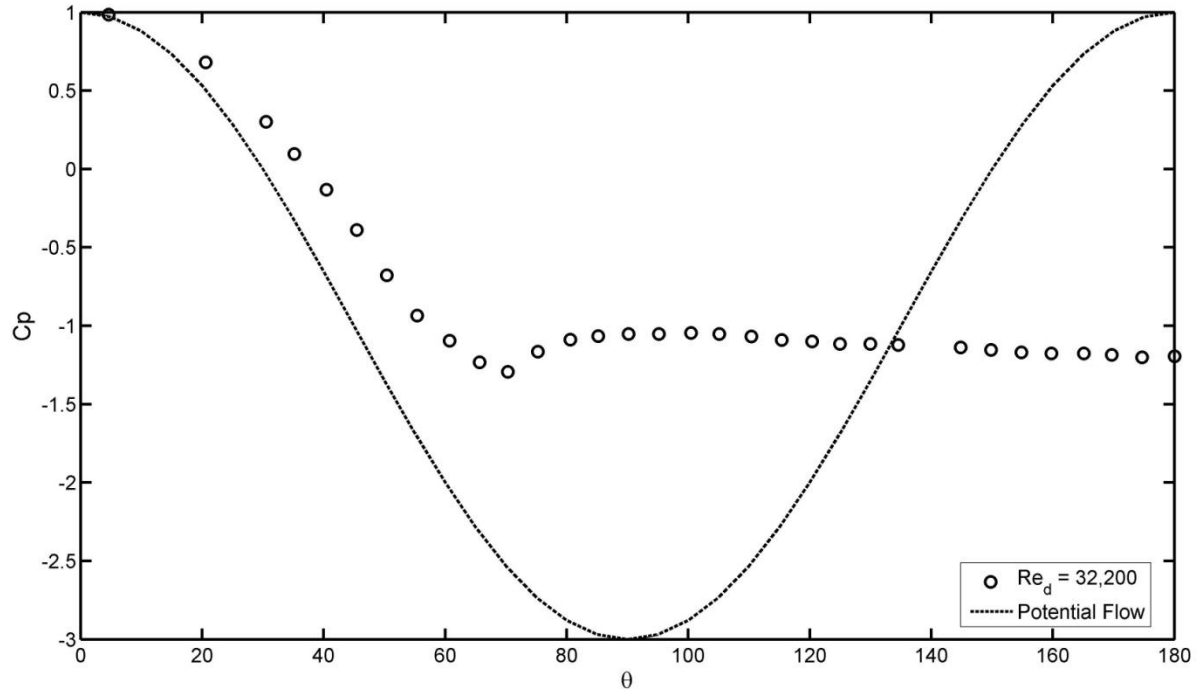


Figure 2.2 Common surface pressure distribution for a circular cylinder (Okamoto & Takeuchi, 1975).

When flow separates from the surface of the cylinder a shear layer is formed (Bloor, 1964). In the shear layer transition regime, transition to turbulence occurs within the separated shear layer and the exact location of the transition depends on Re_d , with the transition point moving upstream with increasing Re_d (Bloor, 1964). Prior to transition, small scale vortices form in the separated shear layer (e.g., Zdravkovich, 1997; Bloor, 1964). The frequency of these small-scale vortices is referred to as the shear layer instability frequency.

The von-Karman vortices, or wake vortices, are shed in an alternating fashion from the top and bottom surfaces of the cylinder. This alternating vortex shedding pattern creates an oscillating transverse force, which has been the focus of a number of studies due to its importance in structural design (e.g., Norberg, 2003). The wake vortices are fully developed

at the end of the vortex formation region. The length of the vortex formation region is defined as the distance from the cylinder axis to the point at which the alternating wake vortices, shed from the upper and lower surface of the cylinder, meet at the central vertical axis of the cylinder (Bloor, 1964). It is commonly determined based on the downstream location of maximum turbulence intensity measured along the centerline of the cylinder (Williamson, 1996). The Strouhal number (St) is a non-dimensional parameter used to characterize the shedding frequency of the wake vortices.

$$St = \frac{f_v d}{U_o} \quad (2.1)$$

where f_v is the frequency of wake vortices, d is the cylinder diameter, and U_o is the free-stream velocity. The Strouhal number is a function of the Reynolds number, and Norberg (2003) presents a chart of the $St-Re_d$ relationship for a wide range of Re_d . A common method for detecting the frequency of the wake vortices is to conduct a spectral analysis of the streamwise fluctuating component of velocity. This method relies on a velocity measurement technique capable of time-resolved measurements.

In addition to time-resolved measurements, time-averaged velocity measurements are important and can classify such features as wake shape and wake width. The wake development is an important aspect in engineering applications. Common characteristics in the wake are the mean half-width (b) and the mean velocity deficit ($U_o - U_{y=0}$). These characteristics can be identified based on a streamwise velocity profile, as shown in Fig. 2.3.

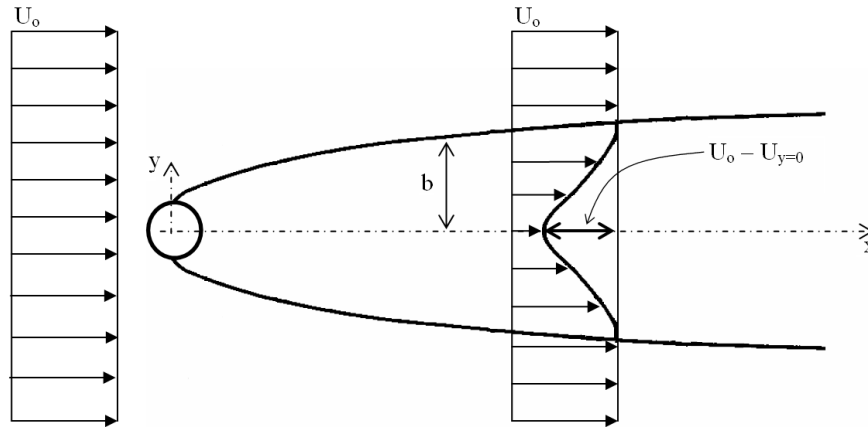


Figure 2.3 Cylinder wake definition.

Due to the growth of b with the downstream distance, the wake vortices diffuse away from the centerline of the cylinder axis within the wake. Schlichting (1930) conducted a study on the development of the far wake and concluded that the mean wake half-width (b) is proportional to $x^{1/2}$, while the mean velocity deficit ($U_0 - U_{y=0}$) is proportional to $x^{-1/2}$.

2.2 The Effects of Blockage on Flow over a Cylinder

Flow development over a circular cylinder, detailed above, is ideally governed by Re_d alone. However, blockage effects can alter flow development. Previous experimental studies, e.g., Okamoto & Takeuchi (1975), West & Aplet (1982), and Ramamurthy & Ng (1973), show that wind tunnel blockage alters flow over a cylinder from what would be expected in an unbounded flow. Specifically, these studies indicate that increasing the blockage ratio increases drag, limits wake growth, and increases vortex shedding frequency.

Okamoto & Takeuchi (1975) conducted an experimental investigation to identify the effect of wind tunnel side walls on flow development over a circular cylinder. The experiments were carried out for $Re_d = 32,000$ and $Re_d = 58,000$, corresponding to the shear layer transition regime (Zdravkovich, 1997), and model blockage ratios (B) ranging from 4%

to 30%. The surface pressure distributions for various model blockage ratios obtained by Okamoto & Takeuchi (1975) are shown in Fig. 2.4. The authors conclude that increasing blockage ratio increases peak suction and reduces base pressure, i.e., pressure drag increases with blockage ratio. Specifically, for $B=30\%$, the total drag coefficient was approximately 50% greater than the expected value published for small blockage ratios. Throughout the range $10\% < B < 30\%$, total drag increases steadily with model blockage ratio. For $B < 4\%$, the effect of blockage ratio on surface pressure distributions was found to be negligible. Supporting these findings, West & Apelt (1982) also conclude that increasing model blockage ratio increases peak suction and reduces base pressure. The authors note that, over the blockage range of $6\% < B < 16\%$, the shape of the pressure distribution curve is altered. Based on the obtained results, they conclude that common post-test blockage correction methods are unsuccessful at mitigating blockage effects.

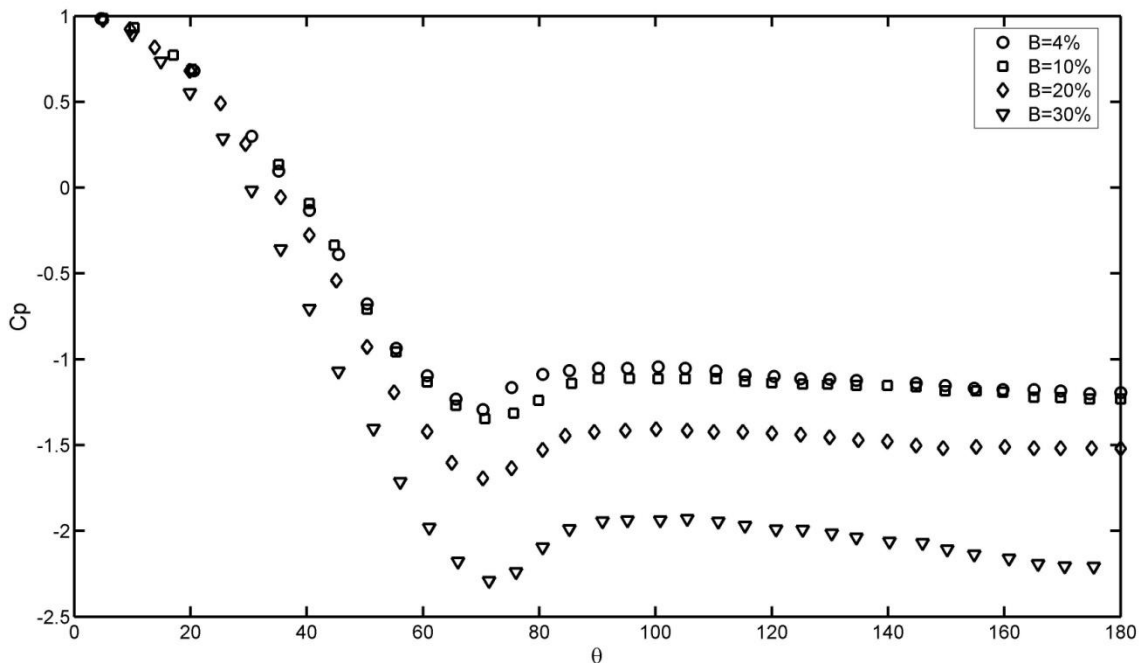


Figure 2.4 Pressure coefficient distributions at various blockage ratios for $Re_d = 32,200$ (Okamoto & Takeuchi, 1975).

In addition to the alteration of surface pressure distribution, blockage also affects wake growth. The effect of model blockage ratio on half wake width (b) is illustrated in Fig 2.5. Okamoto & Takeuchi (1975) found that for low blockage ratios ($B < 5\%$), the wake width growth was uninhibited up to and including the streamwise location $x/d = 40$. This growth is evident in Fig. 2.5, as wake width (b) grows with each increasing streamwise location (x/d). However, for higher blockage ratios, the location at which the wake width growth is limited moves upstream. This limitation is particularly evident for the $B=20\%$ and $B=30\%$ curves, as b reaches a maximum at $x/d < 10$ and decreases for all x/d locations downstream of its maximum.

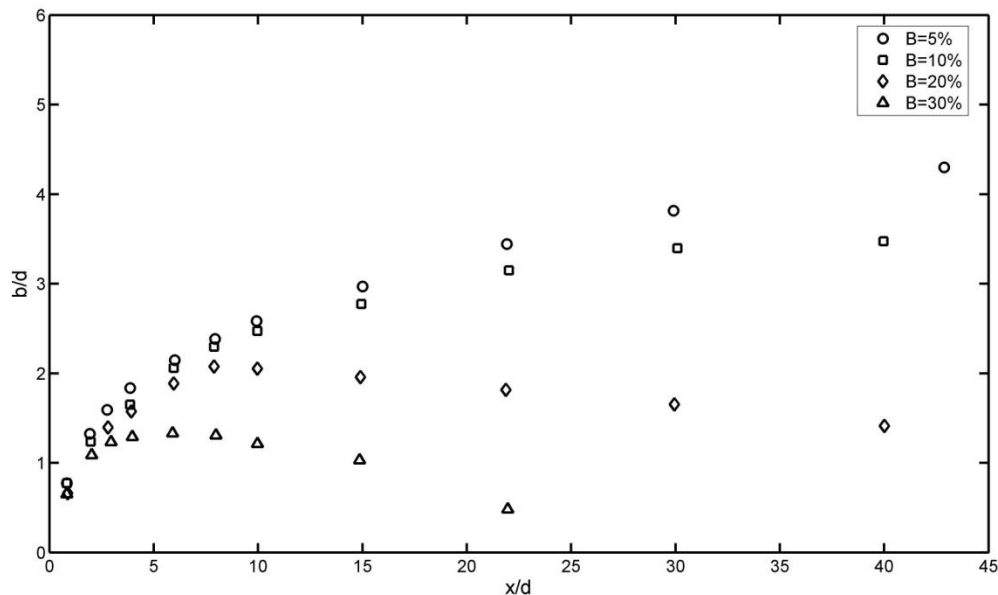


Figure 2.5 Wake width growth at various blockage ratios (Okamoto & Takeuchi, 1975).

Okamoto & Takeuchi (1975) investigated the effect of the blockage ratio on the vortex shedding frequency. The authors conclude that the Strouhal number is virtually independent of model blockage ratio. Contrary to that result, Ramamurthy & Ng (1973) found that increasing the model blockage ratio increases the frequency of shedding vortices,

hence the Strouhal number. This trend was also confirmed by Hiwada & Mabuchi (1981) and Goodyer & Saquib (2007). On the basis of a comprehensive review of several studies, Zdravkovich (2007) suggests that the increase in shedding frequency is related to the decrease in near wake width.

2.3 Adaptive-Wall Studies for External Flows

The majority of investigations involving two-dimensional models in adaptive-wall wind tunnels have been focused on lifting bodies (Wolf, 1995). For example, Russo et al. (1995) and Bottin et al. (1997) studied flow over an airfoil in an adaptive-wall wind tunnel. Specifically, Russo et al. (1995) identified the effect of wall adaptation on flow over a NACA 0012 airfoil for flows up to a Mach number (Ma) of 0.4. Airfoils with chord lengths of 100 mm, 150 mm, and 200 mm were used with corresponding blockage ratios of 6%, 9%, and 12% at zero angle of attack. Walls were streamlined using two different wall-adaptation strategies; namely, the Wall Adaptation Strategy (WAS) by Judd et al. (1981) and the 'FLEXWALL' strategy by Everhart (1983). Judd's method is based on representing the walls as a series of vortices. The aim of the strategy is to reduce the strength of the vortices to zero, which indicates walls are streamlined. The FLEXWALL approach is more mathematically intensive and relies on determining a complex velocity at the wall boundaries via the Cauchy integral formula. Measurements were conducted in the streamlined wall configurations predicted by each strategy, and the results were contrasted. To identify the effect of wall adaptation, analysis included the calculation of pressure drag, based on surface pressure measurements, and the determination of lift curves for angles of attack between 0° and 8°. The results show that increasing blockage increases pressure drag as well as the slope of the lift curves. The results obtained for the 'WAS' and 'FLEXWALL' streamlined

configurations were very similar. For example, the differences between the surface pressure distributions obtained for the ‘WAS and ‘FLEXWALL’ strategies for the angle of attack of 8° and $Ma = 0.4$ were within experimental uncertainty of the study. The lift curves determined using both strategies were consistent with published lift curves obtained at low blockage ratios.

Similar to the investigation by Russo et al. (1995), Bottin et al. (1997) conducted an investigation to identify the effect of wall adaptation on flow over a NACA 0012 airfoil with a chord length of 100 mm. Tests were conducted at a Reynolds number (based on the chord length) of 612,000 and a blockage ratio of 10% at zero angle of attack. The authors conclude that wall interference is essentially removed for angle of attack up to and including 4° .

Recently, Goodyer & Saquib (2007) investigated the upper-limit of blockage ratio for which the drag and Strouhal number can be adequately predicted for a circular cylinder in an adaptive-wall wind tunnel. Tests were conducted for $Re_d = 52,000$ and model blockage ratios ranging from 20% to 100%. Measurements were limited to characterizing the effect of wall adaptation on mean surface pressure distributions and shedding frequencies. Test section walls were streamlined using the predictive wall adjustment strategy of Wolf & Goodyer (1988). Consistent with the results of Okamoto & Takechi (1975) and West & Apelt (1982), Goodyer & Saquib (2007) show that pressure drag significantly increases with model blockage ratio when measured in straight (i.e., non-streamlined) walls. Agreeing with Zdravkovich (2007), the Strouhal number is also reported to increase with model blockage ratio when measured in non-streamlined walls. The increased drag coefficient was reduced slightly when the walls were set to a wall configuration that removes horizontal buoyancy. Also, in this wall configuration, the vortex shedding frequency decreased; however, the

corresponding Strouhal numbers were still in excess of the expected range of $0.18 < St < 0.19$ for the investigated Re_d (Norberg, 2003). Upon streamlining the walls, adequate estimates of the drag were achieved at model blockage ratios up to and including $B=50\%$. Streamlining the walls also resulted in reasonable estimates of the Strouhal number up to and including $B=85\%$.

Another investigation aimed at studying the effect of wall streamlining on flow development over a circular cylinder was carried out at the University of Waterloo. Kankainen et al. (1994) studied flow over a circular cylinder with a blockage ratio of 30% for $Re_d = 500,000$, which corresponds to the supercritical flow regime. The results show that the solid blockage effects were eliminated from the surface pressure distribution when walls were streamlined using the predictive wall adjustment strategy of Wolf & Goodyer (1988). All velocity and pressure measurements obtained in their investigation were time-averaged, thus the determination of shedding frequency via spectral analysis was not possible.

All examples of adaptive-wall studies summarized above involve two-dimensional wall-adaptation for two-dimensional flows. With proper implementation, two-dimensional wall-adaptation strategies can be applied to three-dimensional flows (Wolf, 1995). For example, at the University of Waterloo, Sumner (1994) conducted an investigation into the effectiveness of two-dimensional wall adaptation for three-dimensional flows over disks and spheres of various sizes. For the cases investigated, the mitigation of blockage effects using a two-dimensional wall adaptation strategy (Wolf & Goodyer, 1988) for the three-dimensional models was promising. Specifically, for the sphere, the effect of blockage on pressure drag was removed with streamlined walls for blockages up to $B = 21\%$.

3 Experimental Apparatus

3.1 University of Waterloo Adaptive-Wall Wind Tunnel

All experiments were conducted in the University of Waterloo Adaptive-Wall Wind Tunnel. Originally built in 1963, the tunnel was extensively upgraded in 1991 by extending the test section and incorporating two flexible walls (Kankainen, 1994). The current set of experiments is the first since Sumner (1994) to utilize the adaptive-wall test section.

A schematic of the wind tunnel is shown in Fig. 3.1. This open-return, suction-type tunnel has a 6-m-long test section, comprised of rigid vertical side walls and flexible top and bottom walls. Flow enters the tunnel through a settling chamber, described in Section 3.2, followed by a fixed contraction ratio of 9.55. The nominal rectangular cross-section of the test section has a height of 0.89 m and a width of 0.61 m. In the nominal test section, free-stream speed can be varied from 2 to 40 m/s, with a background turbulence intensity of less than 0.3%. Flow exits through the diffuser and fan section and is recirculated through the laboratory air space to the inlet of the tunnel.

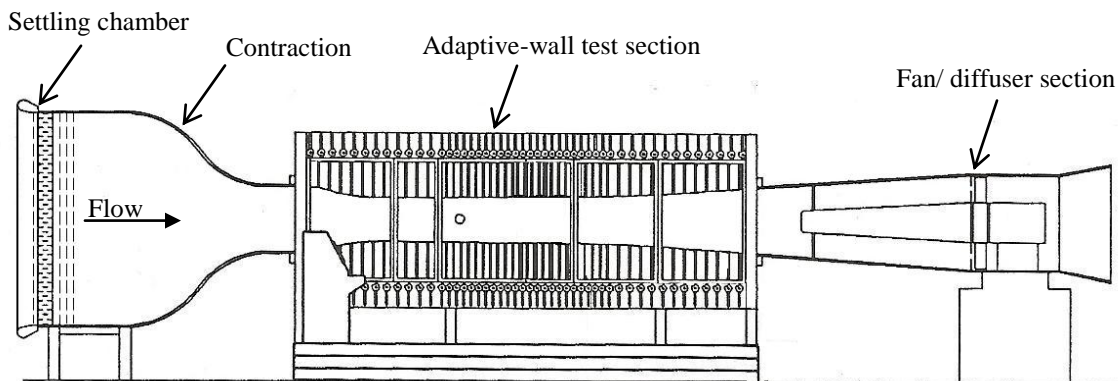


Figure 3.1 University of Waterloo Adaptive-Wall Wind Tunnel.

Vertical Side Walls

The length of the test section is comprised of rigid vertical side walls. One side wall is made of 25.4 mm thick particle board panels, painted matte black, mounted to interchangeable steel frames. The opposing vertical side wall is comprised of 25.4 mm thick clear cast acrylic panels mounted to similar steel frames. The clear cast acrylic was chosen to allow viewing access to the model and traversing mechanism as well as to allow flow visualization, e.g., smoke wire flow visualization (Yarusevych et al., 2008).

Flexible Walls

Flexible top and bottom walls are made of lexan polycarbonate plastic sheets, spanning the entire length of the test section. The shape of each flexible wall can be adjusted by a total of 48 rack and pinions, which are more densely spaced in the vicinity of the model location to allow for an increased radius of curvature. To the same end, the thickness of the lexan polycarbonate sheets is thinner in the central region (3.18 mm versus 4.76 mm) to allow for a more refined adjustment. Course adjustment of the rack and pinion is completed by rotating a disk concentrically connected to the pinion in increments of 15° . Fine adjustment is controlled by a lever which can rotate the pinion with an accuracy of 0.5° . As a result, the rack and pinions can position the walls to within 0.1 mm of the desired location. Based on required wall deflections, the position of each jack, i.e., the disk and lever angles, is determined by a MATLAB program. Since the wall movement is a manual process, the time required to set all of the 96 jacks is approximately 1.5 hours.

In order to facilitate the movement of the flexible walls relative to the stationary vertical side walls, while maintaining a tight seal during testing, the edges of the flexible

walls are lined with inflatable rubber seals. When moving the walls, the seals are deflated; conversely, during testing, the seals are inflated to a pressure of 150 kPA (~22 psi) to ensure an air-tight seal at the flexible wall – stationary wall junctions.

To enable wall pressure measurements required for streamlining the walls, each flexible wall is equipped with 70 pressure taps along its centerline. Nominally, the centerline taps are spaced 152.4 mm apart; however, in the vicinity of the model location, the taps are spaced 50.8 mm apart. Each pressure tap has a diameter of 1.0 mm and is connected to 3.18 mm (outer diameter) flexible tubing.

3.2 Flow Quality Assessment and Settling Chamber Modifications

Prior to settling chamber modifications, the streamwise turbulence intensity and flow uniformity was measured to be 0.6% and 1.2%, respectively, in the nominal test section configuration. Measurement of axial turbulence intensity and flow uniformity, with the original settling chamber, are detailed in Appendix A. According to the objectives outlined in Section 1.5, an upgrade to the settling chamber was required to improve free-stream flow quality. Specifically, three primary objectives of the settling chamber modifications were to:

- i) Achieve axial turbulence intensity < 0.5 %
- ii) Achieve free-stream flow uniformity within $\pm 1\%$
- iii) Enable cleaning of screens once installed

Prior to the construction of a new settling chamber, the original settling chamber consisted of one honeycomb and two screens. The characteristics of the original honeycomb and screens are included in Appendix A. The design characteristics of the original settling chamber were evaluated in accordance with the flow conditioning guidelines by Mehta &

Bradshaw (1979). Primary concerns were the small ratio of honeycomb length to diameter and the small open area ratio of the first of two screens. The ratio of honeycomb length to diameter was measured to be 4.9, outside the recommended range of 6-8 (Mehta & Bradshaw, 1979). In addition, the open area ratio of the upstream screen was measured to be $\beta = 56\%$, below the minimum of $\beta = 58\%$ suggested by Mehta & Bradshaw (1979). Furthermore, the design of the original settling chamber did not allow for the screens to be cleaned, thus the open area ratio of $\beta = 56\%$ was most likely even lower due to blockage caused by particle entrapment.

A new settling chamber was designed based on design guidelines proposed by Mehta & Bradshaw (1979). Additionally, empirical formulae developed by Wieghardt (1953) and Prandtl (1933) were utilized in order to predict streamwise turbulence intensity. The new settling chamber (Fig. 3.1 above) contains one honeycomb and four screens, one screen upstream and three screens downstream of the honeycomb. The honeycomb is 101.6 mm long, composed of 12.7 mm aluminum hexagonal cells, with a 0.127 mm wall thickness. This geometry corresponds to a honeycomb length to (hydraulic) diameter ratio of 8. The screens are a woven stainless steel mesh, often referred to as bolting cloth. The screen upstream and the screens downstream the honeycomb have open area ratios of 64.8% and 62.4%, respectively. Appendix A includes characteristics of the honeycomb and screens and details of construction.

With the new settling chamber installed, flow uniformity in the test section was measured to be within $\pm 0.6\%$ at a free-stream speed of 15 m/s. At the same free-stream speed, streamwise turbulence intensity is less than 0.3%. These flow measurements satisfy

the set objectives listed in Section 1.5. Detailed results from free-stream measurements are included in Appendix A.

3.3 Velocity Measurements

Free-Stream Velocity

The free-stream velocity (U_o) in the test section was set by measuring the pressure drop across the wind tunnel contraction (9.55 ratio), which was calibrated against a pitot-static tube positioned in the mid-span of an empty test section at the streamwise location of the model central axis. The static pressure difference across the contraction and the dynamic pressure from the pitot-static tube were measured using two identical Lucas Schaevitz 0-2”H₂O pressure transducers. The calibration curves, which plot the dynamic pressure of the free-stream versus contraction pressure drop, are included in Appendix B. The total uncertainty of the free-stream speed measurements is estimated to be less than 2.5%.

Cylinder Wake Velocity Measurements

The cylinder wake was traversed with three velocity measurement devices: a pitot-static tube (U measurement), a normal hot-wire probe (U, u' measurements), and a cross-wire probe (U, V, u', v' measurements). Each device was spaced equally in the vertical direction, shared the same spanwise axis, and was housed in a lexan rake holder. The normal and cross-wire probes were operated using a Dantec 56C16 constant temperature anemometry (CTA) bridge and a pair of Dantec 56C17 CTA bridges, respectively. All analog signal outputs were digitized using a National Instruments PCI-6259 data acquisition card and stored to a PC for post processing.

The hot-wire probes were calibrated against a pitot-static tube, either in an empty test section or well outside the cylinder wake. Calibration curves were approximated by a 4th order polynomial fit to the calibration data. The calibration procedure and typical calibration curves are included in Appendix B.

Estimates of the errors associated with hot-wire measurements are based on the work of Kawall et al. (1983) and a full description of uncertainty analysis can be found in Appendix D. The accuracy of hot-wire velocity measurements decreases with increasing turbulence intensity. Based on this fact, the error associated with normal and cross-wire probes is minimum in the free-stream and is maximum in the near wake of the cylinder. Specifically, for a normal probe, the total errors associated with the measurements of the mean (U) and RMS (u') streamwise velocities with are 2.1% and 2.4%, respectively, in the free-stream, and increase to 5.2% and 3.4% when the probe is located in the near wake of the cylinder ($x/d \leq 9$). The cross-wire probe is more susceptible to high turbulence intensities, with the errors in mean (U) and RMS (u') streamwise velocities being 5.5% and 3.1%, respectively, in the near wake. Therefore, when only instantaneous streamwise velocity was required (e.g., for determining vortex formation length), measurements from the normal hot-wire probe were used. However, in the very near wake ($x/d < 4$), the normal hot-wire probe over predicts velocity in the wake due to a non-negligible vertical velocity component (Ong & Wallace, 1996; Bishop et al., 2009). To that end, the cross-wire probe was used in order to resolve streamwise (U) and vertical (V) velocity components. Table 3.1 shows estimates of the total errors associated with all types of hot-wire measurements conducted in this study. Appendix D contains an expanded version of this table in which hot-wire errors are listed for specific figures throughout the main body.

Table 3.1 Estimates of maximum hot-wire errors (Kawall et al., 1983)

Type of Measurement	Probe	Error (%)
Mean streamwise velocity (outside wake)	Normal	2.1
	Cross-wire	2.2
Mean streamwise velocity (inside wake, $x/d \leq 9$)	Normal	5.2
	Cross-wire	10.8
Mean streamwise velocity (inside wake, $x/d > 9$)	Normal	2.9
	Cross-wire	4.8
Mean vertical velocity (outside wake)	Cross-wire	2.1
Mean vertical velocity (inside wake, $x/d \leq 9$)	Cross-wire	48.0
Mean vertical velocity (inside wake, $x/d > 9$)	Cross-wire	3.9
RMS streamwise velocity (outside wake)	Normal	2.4
	Cross-wire	2.7
RMS streamwise velocity (inside wake, $x/d \leq 9$)	Normal	3.4
	Cross-wire	3.8
RMS streamwise velocity (inside wake, $x/d > 9$)	Normal	2.4
	Cross-wire	2.4
RMS vertical velocity (outside wake)	Cross-wire	2.6
RMS vertical velocity (inside wake, $x/d \leq 9$)	Cross-wire	14.1
RMS vertical velocity (inside wake, $x/d > 9$)	Cross-wire	5.3

3.4 Automated Traverse

Included in the objective to modernize the wind tunnel was the development of a traversing mechanism capable of accurately positioning velocity measurement instruments in the test section. Such a device was designed and built entirely in the laboratory (Gerakopoulos, 2008). The design incorporates three-axis motion, driven by three individually controlled high precision stepper motors. The software and electrical hardware required to automate the traverse was developed solely by the author. All software was written in Labview Virtual Instruments and the main hardware consists of:

- Three Gecko stepper driver units (model G210)
- National Instruments data acquisition card (model PCI-6024E)
- Six Honeywell roller limit switches (model MICRO 11SM1-T)

- One 20 VDC, 20 AMP unregulated direct current power supply

Specific details of traverse control and automation are included in Appendix B.

The traverse has a vertical range of 0.27 m, a spanwise range of 0.40 m, and a streamwise range of 1.8 m. The positioning accuracy of the traverse is ± 0.1 mm for the vertical and spanwise directions, and ± 0.2 mm for the streamwise direction (Appendix D). To facilitate movement in the streamwise direction, a slot was cut in the vertical particle board side wall of the test section. In order to move the traverse and seal the slot simultaneously, a slot sealing mechanism was designed and fabricated. This custom slot sealing device consists of polyurethane belting, two bearing idlers, and two torsional spring-loaded belt housings. Smoke tests indicated no leakage along the length of the slot for speeds up to and including 20 m/s.

3.5 Wall Pressure Measurements

Static pressure measurements along the test section walls are key to implementing the wall adaptation strategy. In line with modernizing the wind tunnel, an automated system was required to acquire measurements from the 140 centreline wall taps. Such a system was implemented utilizing two electronic pressure scanner modules (Scanivalve ZOC33). The ZOC33 module is capable of measuring pressures within the range of 0–5" H₂O. Peripheral electrical and pneumatic systems were required to interface each pressure scanner module with the PC, and a list of the required hardware is included below. Figure 3.2 shows how the peripheral components are integrated with one pressure scanner module.

- Two Scanivalve electronic pressure scanners modules (model ZOC33PxX2)
- National Instruments data acquisition card (model PCI-6259)

- One 3-way and six 2-way solenoid valves
- Custom solid state relay (SSR) board to control 7 solenoid valves required for activation of 65 psi pneumatic control lines
- Two custom TTL to CMOS boards to convert 5V digital logic from PCI-6259 to 15V digital logic required for ZOC33 binary addressing
- Custom cables to facilitate custom boards
- Custom chassis to house custom boards

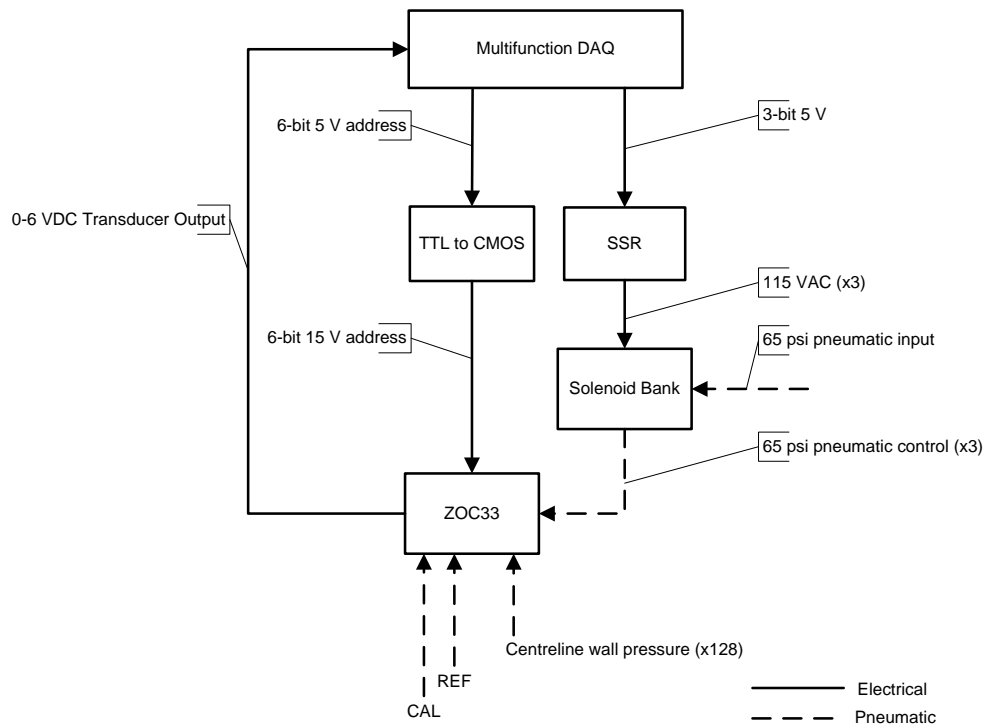


Figure 3.2 Hardware schematic for wall pressure measurements.

Each ZOC33 module houses 64 piezo-resistive differential pressure sensors, each of which is duplexed (i.e., the sensor can be connected to one of two pneumatic lines). Thus, each module can be used to sequentially measure pressure from up to 128 pneumatic inputs. Two modes of operation were employed for the ZOC33 units: calibrate and operate. The calibrate mode is used to generate calibration curves for each sensor. In this mode, each

sensor is connected to a reference pressure (REF) and a calibration pressure (CAL). By varying the differential pressure (CAL – REF) and recording the corresponding voltages, a unique calibration curve is generated for each of the sensors. Calibration mode not only allows calibration of the unit, but also enables the determination of temperature based zero-offset voltages by equalizing the CAL and REF pressures and measuring the corresponding offset voltage. The zero-offset voltage can be determined while the tunnel is running, which is advantageous from an operating perspective. In operate mode, which is used to measure wall pressure distributions, each sensor is connected to an individual pneumatic input and a reference pressure (REF) that is common to all sensors in the module.

Modes of operation are selected via 65 psi pneumatic control lines operated in a binary logic state. The activation of the pneumatic control lines are controlled through a solenoid bank. The output from the desired sensor is accessed through a 6-bit 15 V CMOS digital address. Since the digital output from the data acquisition card is 5 V (TTL logic), a TTL to CMOS board was fabricated. Detailed drawings for this board, as well as other hardware required to interface the ZOC33 modules to the wind tunnel PC are fully detailed in Appendix B. All of the required software to control hardware was developed solely by the author in Labview.

All 128 pressure sensors in both ZOC33 modules were calibrated using a GE Precision Portable Pressure Calibrator DPI 610. The uncertainty associated with the wall pressure measurements is estimated to be $C_{pw} \pm 0.022$, as detailed in Appendix D.

3.6 Cylinder Model and Model Pressure Measurements

In this study, two plastic circular cylinders, of diameter 0.043 m and 0.089 m, were used. To allow surface pressure measurements, each cylinder was equipped with a single 0.8 mm

diameter pressure tap drilled at its midspan. In order to make a connection to the pressure tap, each cylinder was spliced through its diameter at a location 50.8 mm from its midspan. Each spliced section of the cylinder was polished in a lathe with sand paper of decreasing grit. The cylinders were reassembled via a machined central plug, ensuring concentricity of the assembled sections. The cylinders were outfitted with end caps to facilitate model mounting in the test section. Both cylinders, centered in the test section, spanned the width of the test section.

The aspect ratio (L/d) for the 0.043 m and 0.089 m cylinders was 14 and 7, respectively. Experimental studies (West & Apelt, 1982; Norberg, 1994) show that the aspect ratio has an influence on flow development over a circular cylinder. To achieve two-dimensional flow, a cylinder of an infinite aspect ratio is required. However, for finite aspect ratios, three-dimensional flow is observed near a model-wall interface, giving rise to wall interference effects. For instance, West & Apelt (1982) showed that pressure drag increases as the aspect ratio decreases. It is of interest to note that decreasing the aspect ratio has the same effect on drag as increasing the blockage ratio. Zdravkovich (2003) notes that decreasing the aspect ratio elongates the vortex formation region. Despite its influence on drag and vortex formation length, aspect ratio has negligible effect on Strouhal number. Although the effect diminishes with increasing L/d , West & Apelt (1982) indicate that aspect ratio can alter flow development at values as high as $L/d = 40$. Therefore, based on these results, it is expected that the pressure distribution curves measured for the $L/d = 7$ cylinder will be lower as compared to those for the $L/d = 14$ cylinder. In addition, the formation length behind the $L/d = 7$ cylinder is expected to be longer than that measured for the $L/d =$

14 cylinder. Thus, the difference in the aspect ratio should be taken into account when comparing measurements conducted with different cylinders.

Surface pressure distributions were acquired by rotating the cylinder using a model-support mechanism, providing an angular resolution of 0.1° (Appendix D). The coordinate system used for data presentation is shown in Fig. 3.3.

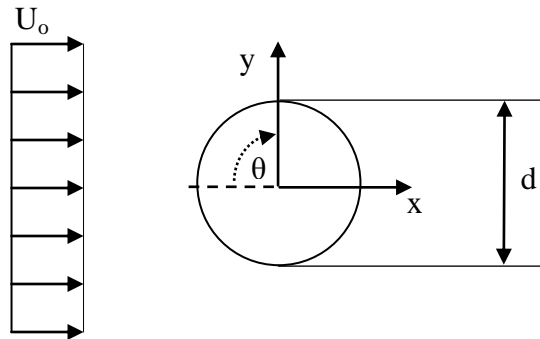


Figure 3.3 Cylinder coordinate system.

The pressure tap of the large cylinder was connected directly to a miniature fast-response pressure transducer (All Sensors 1-INCH-D2-4V-MINI). Embedding a pressure sensor inside the cylinder allowed for time-resolved pressure measurements. In contrast, due to space constraints, the pressure tap of the small cylinder was connected to an external pressure transducer (Lucas Schaevitz P3061-2WD). The employed pressure transducers were calibrated using a precision portable pressure calibrator (General Electric DPI-610). The uncertainty associated with surface pressure measurements is estimated to be $C_{pw} \pm 0.022$, as detailed in Appendix D.

3.7 Geometrically Straight Walls (GSW)

In order to investigate a range of blockage ratios, experiments were conducted with two wall configurations. In addition to the nominal cross section (0.89 m x 0.61 m), a contracted cross

section (0.53 m x 0.61 m) was used to achieve higher blockage ratios. Both wall configurations are shown in Fig. 3.4, and Table 3.2 details the corresponding test matrix. Except for the contraction and diffuser in the contracted test section, the upper and lower flexible walls are spaced by a fixed vertical distance (h) for the entire length of the test section. In this configuration, the walls are termed ‘Geometrically Straight Walls’ (GSW). The flexible contraction in Fig. 3.4 has a contraction ratio of 1.7 and was designed based on the recommendations of Sumner (1994). The length of the test section was limited in order to achieve a diffuser angle which does not promote flow separation. The diffuser, shown in Fig. 3.4, has a diffuser angle of 6° , which is below the angle which causes separation for subsonic flows (Bradshaw & Mehta, 2003).

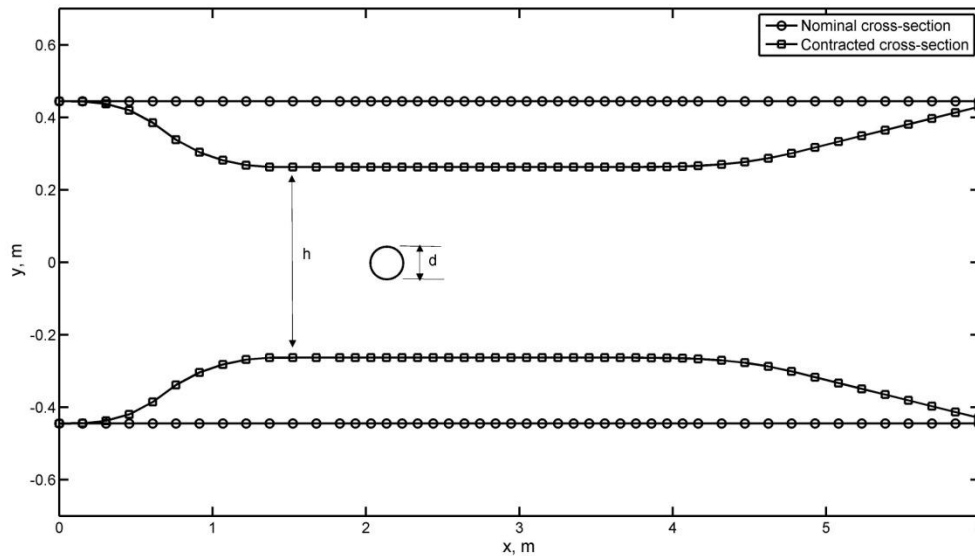


Figure 3.4 Test section wall configurations.

Table 3.2 Test matrix.

Wall Configuration	h , m	d , m	L/d	B , %
Nominal	0.890	0.043	14	4.7
Contracted	0.527	0.043	14	8.0
Contracted	0.527	0.089	7	16.9

Throughout the discussion of results, the corresponding blockages listed in Table 3.2 will be rounded to 5%, 8%, and 17%.

4 Wall Adaptation Strategy

4.1 Aerodynamically Straight Walls (ASW)

A boundary layer forms on each of the four test section walls. Based on the range of free-stream speeds used in this study, a turbulent boundary is expected to occupy the majority of the test section wall length. Assuming a $1/7^{\text{th}}$ power law velocity distribution in the boundary layer and conducting an integral analysis on the boundary layer control volume, the thickness of the boundary layer (δ) can be calculated by Eq. 4.1 (White, 2008).

$$\frac{\delta(x)}{x} \approx \frac{0.16}{\text{Re}_x^{\frac{1}{7}}} \quad (4.1)$$

The boundary layer growth with streamwise distance (x) gives rise to a negative pressure gradient and an increase in streamwise velocity within the test section (see Section 1.3.3). To mimic an unbounded flow, the walls need to be adjusted such that the pressure gradient is removed and the free-stream velocity remains constant with streamwise distance. Such a wall configuration is referred to as ‘Aerodynamically Straight Walls’ (ASW).

The presence of the boundary layer deflects an otherwise parallel incoming streamline by a distance referred to as the displacement thickness (δ^*) (White, 2008). A mathematical relationship for the displacement thickness can be determined by control volume analysis of the boundary layer region and the result is shown in Eq. 4.2. Furthermore, the displacement thickness can be related to the boundary layer thickness by assuming a $1/7^{\text{th}}$ power law velocity distribution and integrating Eq. 4.2, which gives Eq. 4.3.

$$\delta^*(x) = \int_0^{\delta} \left(1 - \frac{U(y)}{U_o} \right) dy \quad (4.2)$$

$$\delta^*(x) \approx \frac{1}{8} \delta(x) \quad (4.3)$$

With the displacement thickness determined as a function of boundary layer thickness, Eq. 4.1 can be substituted into Eq. 4.3 to yield boundary layer thickness as a function of the streamwise distance (x) and the Reynolds number (Re_x), as shown in Eq. 4.4.

$$\frac{\delta^*(x)}{x} \approx \frac{1}{8} \frac{0.16}{\text{Re}_x^{\frac{1}{7}}} \quad (4.4)$$

Theoretically, for unbounded flow over a single wall, contouring the wall to δ_x^* (Eq. 4.4) will remove the effects of horizontal buoyancy. In the test section, however, the rigid vertical side walls cannot be adjusted. Thus, a residual increase in free-stream speed remains even after the flexible roof and floor have been contoured to Eq. 4.4. To account for this, an empirical multiplication factor is applied to increase displacement so as to remove the residual pressure gradient. This method is similar to that employed by Sumner (1994) and additional details can be found in Appendix C.

Wall pressure distributions measured in the GSW and ASW configurations, with an empty test section, are shown in Figs. 4.1 and 4.2 for the nominal and contracted test sections, respectively. As shown in Fig. 4.1, the roof and floor have a negative pressure gradient along the entire test section length of 6m, attributable to boundary layer growth. With the walls set to the ASW configuration, the negative pressure gradient is removed and $C_{pw} = 0$ throughout the test section. With the pressure gradient removed, the free-stream speed is constant for all streamwise locations and thus, horizontal buoyancy is alleviated. For the contracted test section, only the region of $1.4 \text{ m} < x < 4.6 \text{ m}$ is available for wall adaptation ($x < 1.4 \text{ m}$ and $x > 4.6 \text{ m}$ are used for the flexible contraction and diffuser, respectively). Similar to the nominal wall configuration, a negative pressure gradient exists in

the contracted test section for the GSW configuration. This pressure gradient is removed in the ASW configuration, i.e., $C_{pw}(x) = 0$. It should be noted that a noticeable change in slope at $x \approx 2.7$ m in the contracted test section for the GSW configuration is due to the presence of the traversing mechanism. With the model installed, the traverse was moved to a downstream location during wall adaptation so as to not affect predicted wall contours. The presence of the traverse is not seen in the nominal test section configuration (Fig. 4.1) since the corresponding distances between the flexible roof and floor to the traverse are much larger than those in the contracted test section.

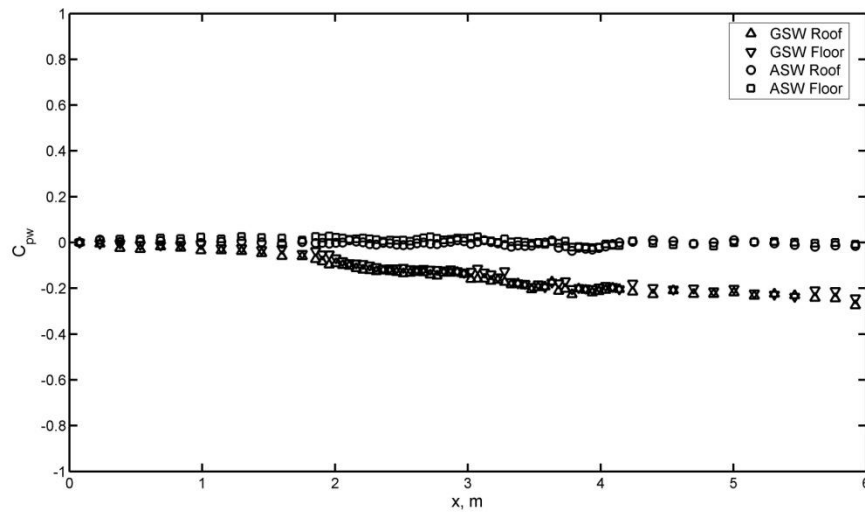


Figure 4.1 Wall pressure distributions in an empty test section for the nominal wall configuration.

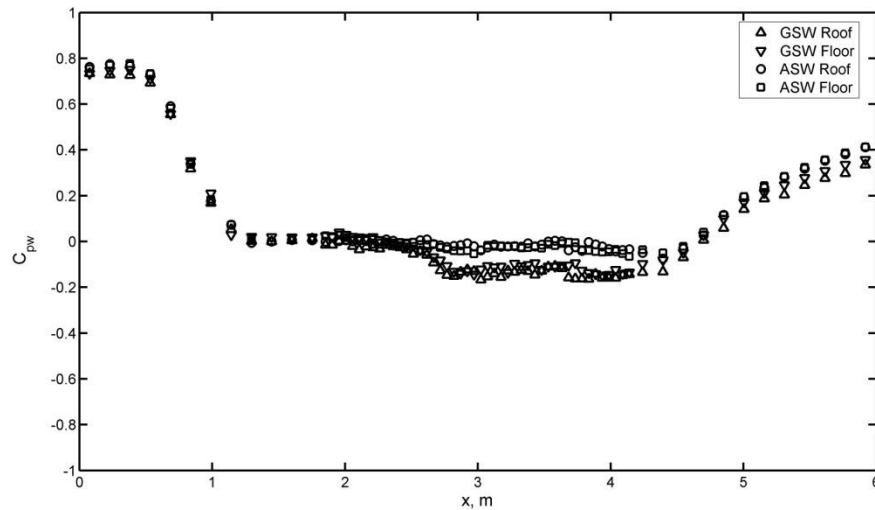


Figure 4.2 Wall pressure distributions in an empty test section for the contracted wall configuration.

4.2 Predictive Wall Adaptation Strategy (WAS)

An effective adaptive-wall strategy is a key to mitigating blockage effects in any adaptive-wall wind tunnel. For two-dimensional flow studies, only the position of two parallel test section walls need to be adjusted, e.g., the top and bottom walls for a horizontally mounted model (Wolf, 1995). In the present investigation, the predictive wall adjustment strategy of Wolf & Goodyer (1988) is utilized. This strategy has been successfully implemented in a number of studies, e.g., Russo et al. (1995) and Goodyer & Saquib (2007), involving two-dimensional, subsonic flows. For this study, the original FORTRAN routine of Wolf & Goodyer (1988) was converted, with required modifications, into MATLAB and implemented into the control system of the University of Waterloo Adaptive-Wall Wind Tunnel. An overview of the adaptive-wall strategy is presented in this section, but the reader is referred to Wolf & Goodyer (1988) for a more exhaustive description, including empirical scaling and coupling factors required for an improved convergence rate.

The goal of the strategy is to shape the flexible walls into streamlines so as to eliminate blockage effects caused by the presence of the model. To achieve this, the strategy considers two distinct regions away from the tested model: (i) a real flow in the test section and (ii) an imaginary flow outside the flexible walls of the test section (Fig. 4.3).

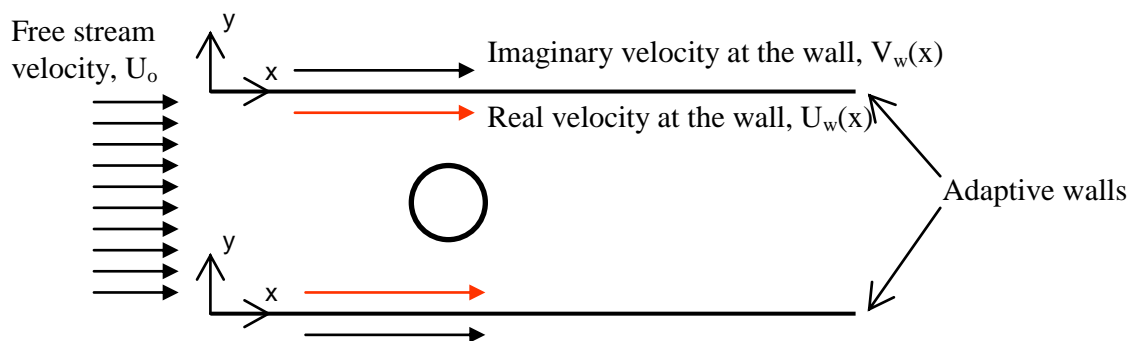


Figure 4.3 Flow division for wall-adaptation strategy.

The imaginary flow field, treated as an inviscid flow, models the flow that would have been observed away from the model in an unbounded flow. The wall is representative of a streamline when velocity along the wall (i.e., the streamline) computed in the imaginary flow field (V_w) matches that computed based on the measured wall pressure distribution in the real flow. At the inlet to the test section, the free-stream velocity (U_o) is common to both the imaginary and real flow fields. In a straight wall test section, the real flow field deviates from the imaginary flow field due to blockage effects, resulting in the velocity imbalance along the wall (i.e., $U_w - V_w \neq 0$). The adaptive wall strategy iteratively adjusts the position of the walls to negate this velocity imbalance. Specifically, the wall is represented as a vortex sheet, with the local strength of vorticity directly related to the velocity imbalance at the wall. A potential flow integral is then employed to calculate local vertical velocity component perpendicular to the wall. Finally, wall deflection required to negate the perpendicular velocity component are computed. In subsequent iterations of the adaptive wall strategy, the imaginary flow field velocity along the wall is computed based on previous values of U_w and V_w as described later in this section. When the velocity imbalance along the walls is removed, the walls are considered to be streamlined. Figure 4.4 shows the basic procedure of the adaptive wall strategy and is described in more detail below.

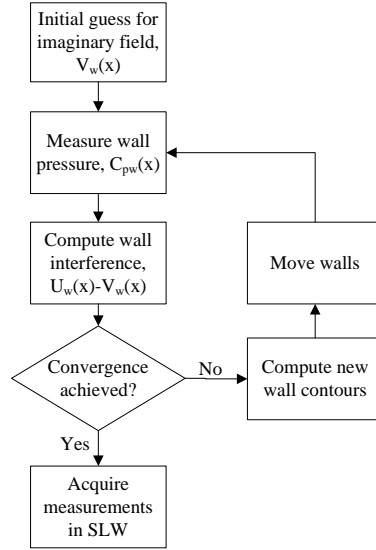


Figure 4.4 Wall streamlining procedure (Wolf, 1995).

The process of the streamlining procedure relies on the division of the continuous wall length into discrete computing points (x_c). For the current study, each computing point corresponds to a jack location. The first jack location is the anchor point (i.e., $x=0$, $y=0$ location in Fig. 4.3), where wall pressure is equal to the static pressure in the incoming free-stream flow, i.e., $P_w(x=0) = P_o$. The anchor point does not move throughout the streamlining algorithm.

An initial guess for the imaginary velocity along the wall is required. For all the blockage ratios investigated, the initial guess was $V_w(x)/U_o = 1$, or a zero pressure gradient, which is representative of an inviscid flow velocity along a nearly horizontal wall. With the model installed and free-stream velocity set, the streamlining procedure commences with the measurement of the wall pressure distributions. The pressures measured at each tap location are transposed to computing points (i.e., jack locations) using a least squares cubic curve fit. The real velocity distribution, $U_w(x)$, is calculated directly from the measured pressure distribution $C_{pw}(x)$ using Eq. 4.5.

$$\frac{U_w}{U_o} = \sqrt{1 - C_{pw}} \quad (4.5)$$

The wall is considered to be loaded, i.e., non-streamlined, if a velocity imbalance between the real and imaginary flow fields exists at any computing point along the wall. The velocity imbalance between the real and imaginary flow fields at a given computing point (x_c) is quantified by a “notional vorticity” of strength, Γ .

$$\Gamma(x_c) = U(x_c) - V(x_c) \quad (4.6)$$

At every computing point, a piecewise cubic vorticity distribution is fit using the vorticity strength at the current computing point (x_c) along with vorticity strengths at one immediate upstream and two immediate downstream computing points. The piecewise cubic curve fit acts to smooth out the vorticity distribution, which is otherwise susceptible to scatter due to uncertainty associated with wall pressure measurements (see Appendix D). The notional vorticity at a given computing point is approximated using Eq. 4.7.

$$\Gamma(x) = ax^3 + bx^2 + cx + d \quad (4.7)$$

A non-zero notional vorticity creates an induced velocity normal to the wall. For a given location, the local induced velocity is influenced by the vorticity distribution along the entire wall ($0 < x < L$). The local induced velocity is calculated at every middle location between adjacent computing points, i.e., “midjack” locations. For a given midjack location, the local induced velocity, $v(x_o)$, is calculated using the potential flow integral, which calculates the contributions of all notional vortices along the wall to the induced velocity at location x_o (Eq. 4.8).

$$v(x_o) = \frac{1}{2\pi} \int_0^L \frac{\Gamma(x)}{x_o - x} dx \quad (4.8)$$

With the induced velocities calculated at each midjack location, the next step is to determine the wall slope required to negate the induced velocity. Assuming a small wall deflection, the approximate change in slope required to negate the induced velocity normal to the wall is given by Eq. 4.9.

$$\frac{dy}{dx}(x_o) = -\frac{v(x_o)}{U_o} \quad (4.9)$$

Using Eq. 4.9, the slope is calculated for each midjack location. For a given midjack location, a quadratic fit (Eq. 4.10) is used to approximate local slope variation based on slope at this location and the slopes at the neighbouring midjack locations. The curve fit acts to smooth out the required wall slope distribution.

$$\frac{dy(x)}{dx} = Ax^2 + Bx + C \quad (4.10)$$

To determine the required change in wall deflection at a given midjack location, each quadratic curve is integrated (Eq. 4.11) between the immediate upstream jack (X1) and downstream jack (X2) surrounding the midjack location.

$$\Delta y = \int_{x_1}^{x_2} (Ax^2 + Bx + C) dx \quad (4.11)$$

This calculation is completed for each midjack location, and, thus, the required displacement between each jack location can be determined, starting from the anchor jack location whose location is fixed.

This process is completed for each wall and the walls are moved to incorporate the predicted wall displacements. Following the wall adjustment, the determination of a new imaginary velocity field is required. With walls adjusted to remove the induced velocity normal to the wall, the imaginary velocity at a given computing point (x_c) is adjusted from its previous value using Eq. 4.12.

$$V_{w,new}(x) = V_{w,old}(x) + 0.8 \left(\frac{U_{w,old} - V_{w,old}}{2} \right) + 0.35(V_{w,old,opposite} - U_{w,old,opposite}) \quad (4.12)$$

The values of 0.8 and 0.35 are empirical scaling and coupling factors, which accelerate the convergence of the streamlining procedure (Wolf & Goodyer, 1988). These empirical factors accommodate simultaneous adjustment of the opposite wall. The walls are considered to be streamlined when the differences between the real and imaginary velocities along the walls are within the corresponding experimental uncertainty of the wall pressure measurements. The number of iterations required for convergence is based on the initial wall contours and imaginary flow field guess. With the wall interference removed, the resulting wall configuration is referred to as ‘Streamlined Walls’ (SLW).

4.3 Streamlining Results

The model was installed with the walls set to the ASW configuration. As discussed in Section 4.2, $V_w(x)/U_o = 1$ was used as an initial guess for the imaginary velocity along the walls. The wall pressures along the roof and floor are then measured, converted to pressure coefficients, and entered as an input into the wall adaptation strategy for the prediction of new wall contours. In the contracted test section, since the flexible walls need to blend

smoothly with an inlet contraction and an outlet diffuser, only the region of $-8.6 \leq x/d \leq 15$ is used in the adaptive-wall strategy. The wall adaptation strategy is executed via the MATLAB program, "WAS.m". Appendix C contains the code of this program as well as supporting functions. For all blockage ratios investigated, convergence was achieved within three iterations.

For a two-dimensional unbounded flow, only streamlines in the relative vicinity of the cylinder are affected by its presence. In the regions of disturbed flow around the cylinder (Fig. 2.1), the velocity and pressure distributions along a given streamline are functions of the streamwise coordinate (x). In the regions sufficiently far from the cylinder, streamlines are unaffected by the cylinder's presence. Thus, for a fixed-height test section, a larger cylinder will have a more pronounced effect on C_{pw} , while a small enough cylinder may not affect C_{pw} at all. For the current study, the vertical distance between the flexible walls and the cylinder axis is $3.0d$, $6.2d$, and $10.5d$, for blockage ratios of 17%, 8%, and 5%, respectively. Due to the close proximity of the walls, for $B=17\%$, the influence of blockage effects on wall distributions should be the greatest relative to the smaller blockage ratios. With the model installed, wall pressure distributions and corresponding wall displacements for each wall configuration are shown in Fig. 4.5 and Fig. 4.6, respectively, for all the blockage ratios investigated. In addition to these plots, streamwise velocity traverses (Fig. 4.7), measured outside the wake highlight the effect of blockage on velocity gradients.

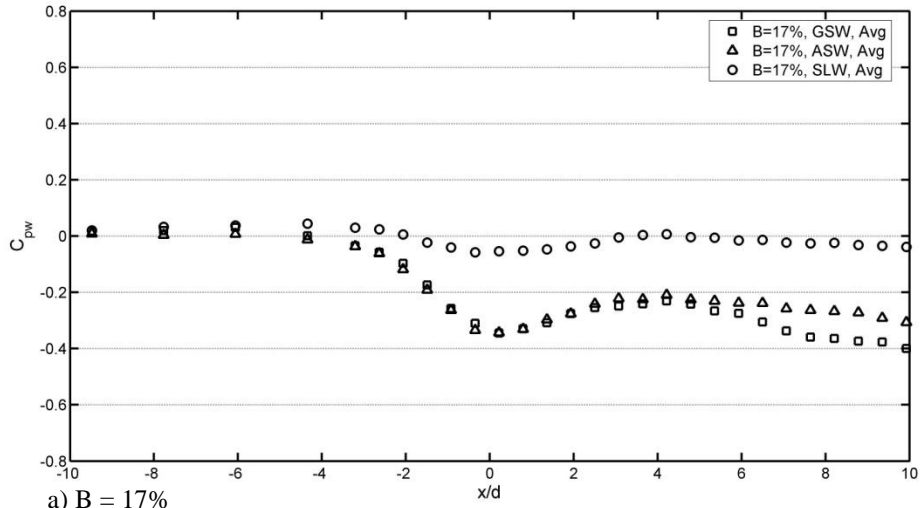
For a blockage of 17%, the proximity of the cylinder is evident in the wall pressure distributions measured in the GSW configuration (Fig. 4.5a), with the largest suction peak appearing at $x/d = 0$ compared to those in the ASW and SLW configurations. This large peak is attributed to a significant velocity increase around the cylinder due to solid blockage

effects. For the ASW configuration (Fig. 4.5a), the wall pressure distribution contains a suction peak at $x/d = 0$ comparable to that measured in the GSW configuration. This result shows that solid blockage is dominant compared to horizontal buoyancy near the cylinder for $B=17\%$. Despite the similar wall pressure distributions in the GSW and ASW configurations within the initial region of the test section, a difference occurs for $x/d > 4$. This difference is attributable to the effects of horizontal buoyancy, which become more pronounced with increasing streamwise location due to boundary layer growth. Upon streamlining the walls, a suction peak at $x/d = 0$ is still present in the SLW configuration, although significantly reduced when compared to the peaks in the GSW and ASW configurations. In addition to the suction peak, a positive pressure gradient exists upstream of the cylinder. Given the close proximity of the flexible walls to the cylinder axis ($y/d = 3$), the observed shape of the pressure distribution is consistent with what would be expected along the corresponding streamline in an unbounded flow. When comparing the pressure distributions for each wall configuration, an interesting feature in the GSW and ASW configurations is the significant pressure gradient observed for $x/d > 5$. It is expected that this negative pressure gradient corresponds to an increase in velocity outside of the wake of the cylinder. Indeed, a positive velocity gradient is observed for $x/d > 5$ in the free-stream velocity profiles (Fig. 4.7a) for $B = 17\%$ in the GSW and ASW configurations. It is speculated that this velocity increase outside the wake is attributable to wake blockage, which will be investigated in Section 5.3.

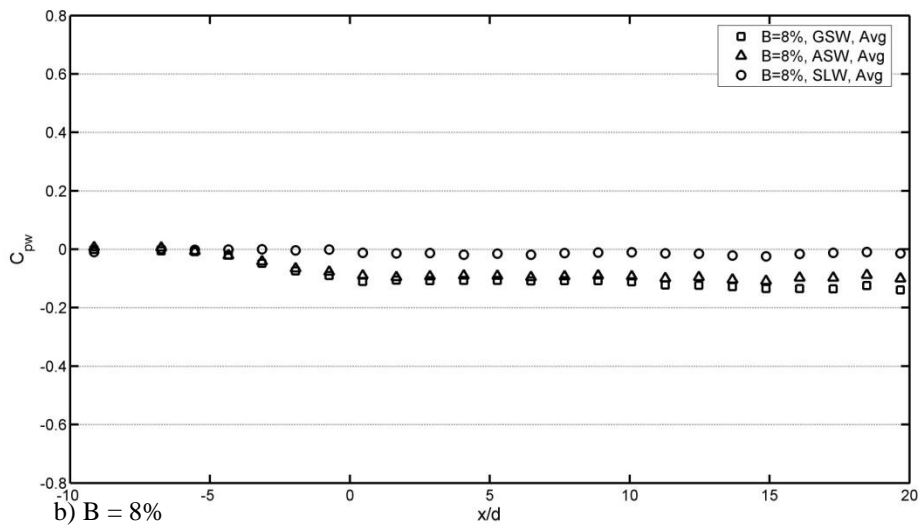
For a blockage of 8%, a decrease in wall surface pressure is evident near the cylinder for the GSW and ASW configurations (Fig 4.5b). The pressure reaches a minimum at $x/d=0$, similar to $B=17\%$, but a defined suction peak is not present. Instead, the negative wall surface pressure coefficient remains reasonably constant for all locations starting at $x/d=0$ for

both the GSW and ASW configurations, being slightly lower in the former configuration. The constant negative pressure coefficient is associated with a velocity outside the wake being greater than the free-stream velocity (U_o). This can be seen in the streamwise velocity profiles in Fig. 4.7b. Specifically, the velocity outside the wake is 3.2% and 5.6% greater than the free-stream speed (U_o) for the ASW and GSW configurations, respectively. Upon streamlining the walls, the wall pressure coefficient approaches zero, within experimental uncertainty, and the speed outside of the wake is equal to U_o , as shown in Fig 4.5b and Fig. 4.7b, respectively.

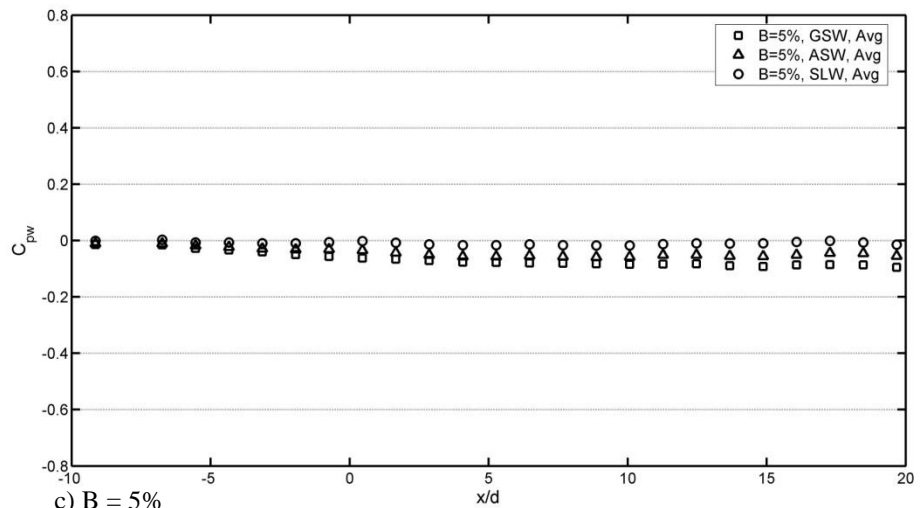
For 5% blockage, the presence of the cylinder in the ASW and GSW configurations still influences the wall surface pressure distributions, resulting in negative pressure gradients observed in Fig. 4.5c. Similar to the pressure distributions for $B=8\%$, the pressure coefficient remains relatively constant downstream of the cylinder axis. From Fig. 4.7c, the speed outside the wake in GSW is 4.2% greater than U_o . With the walls in the SLW configuration, the wall surface pressure coefficient is approximately zero for all streamwise locations. The streamwise velocity profile for the SLW configuration in Fig. 4.7c indicates that the velocity outside the wake is about 2% less than the free-stream velocity (U_o). This difference, however, is within the experimental uncertainty of the free-stream velocity measurements, thus the difference is not statistically significant.



a) $B = 17\%$



b) $B = 8\%$



c) $B = 5\%$

Figure 4.5 Wall pressure distributions in the GSW, ASW, and SLW configurations for a) $B=17\%$, b) $B=8\%$, and c) $B=5\%$.

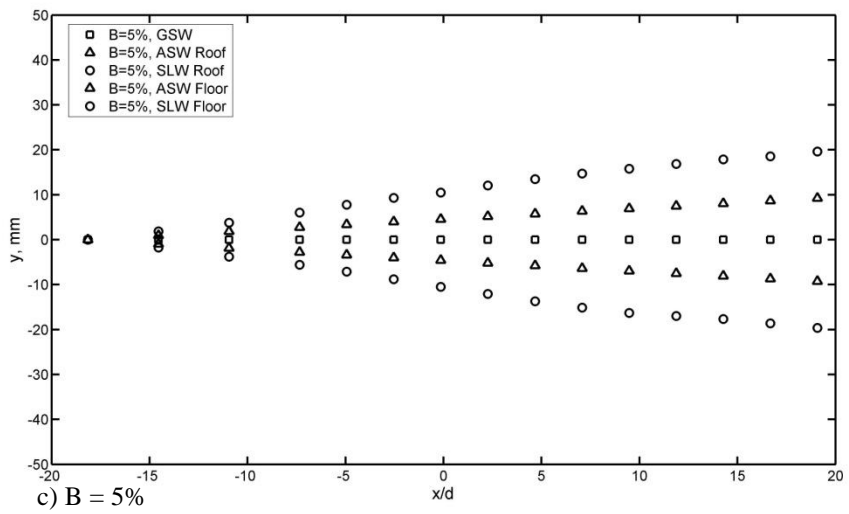
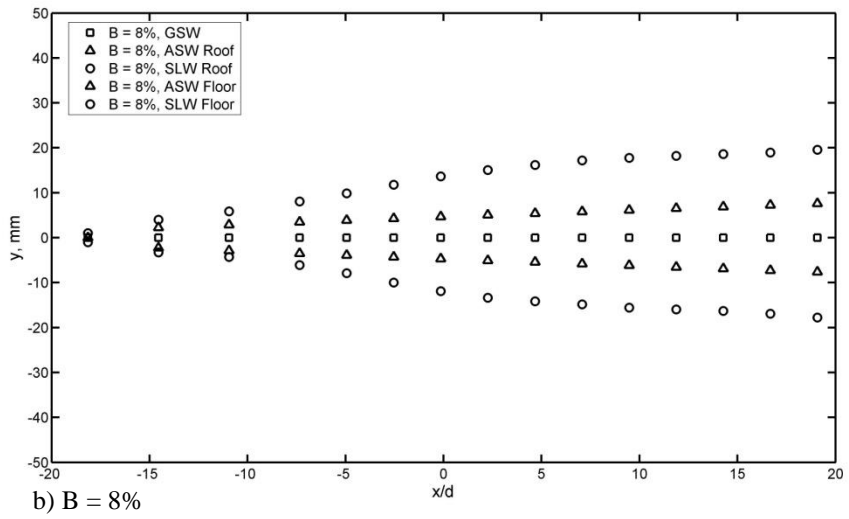
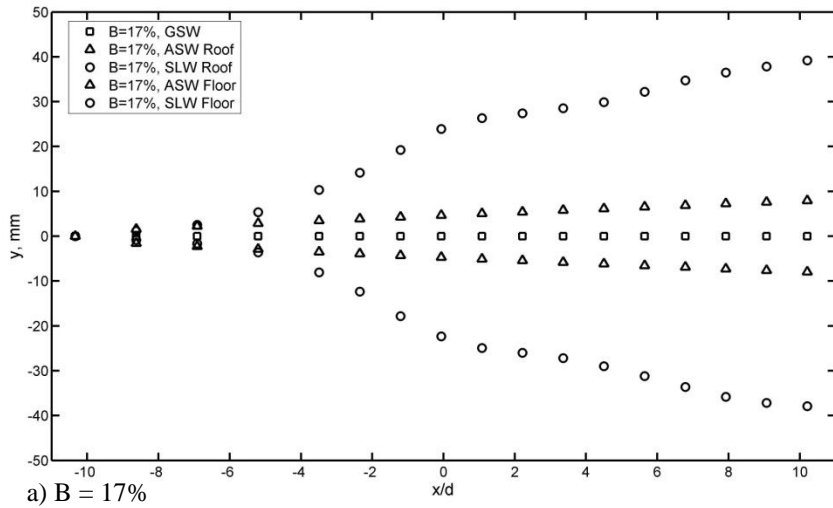


Figure 4.6 Wall deflections from GSW in the ASW and SLW configurations for a) $B=17\%$, b) $B=8\%$, and c) $B=5\%$.

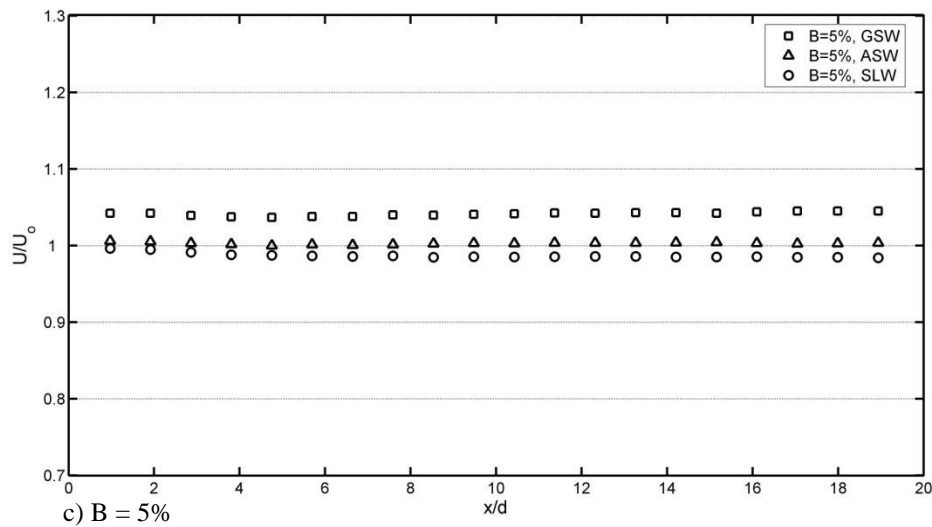
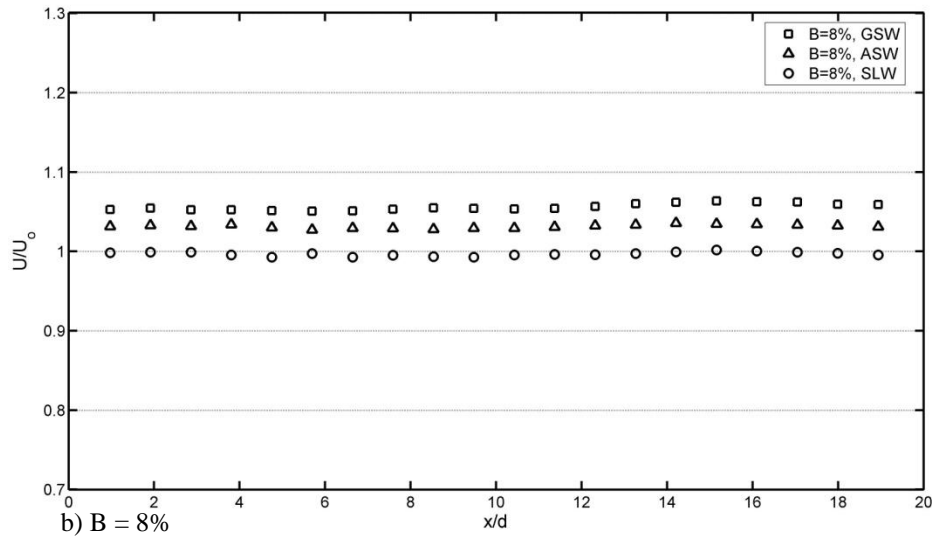
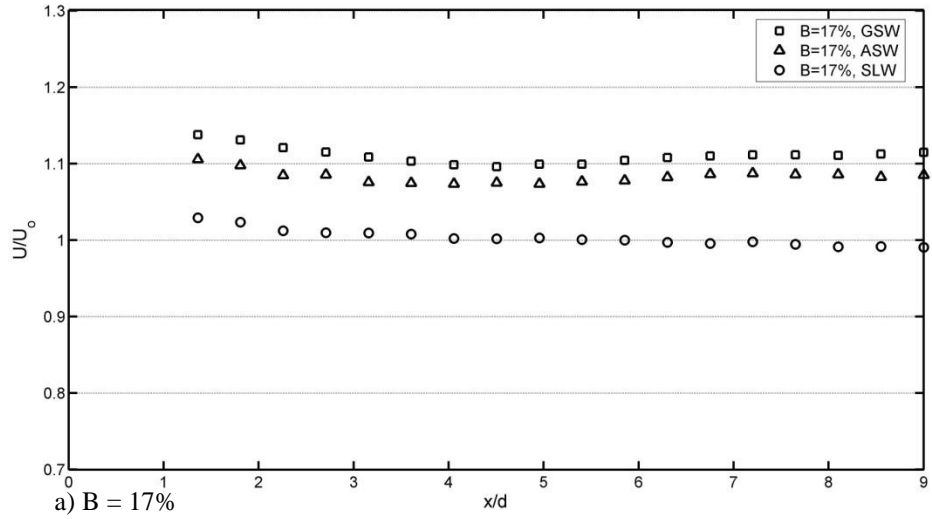


Figure 4.7 Streamwise velocity measured outside the wake for a) $B=17\%$, b) $B=8\%$, and c) $B=5\%$.

5 Experimental Results

All experiments were conducted for $Re_d \approx 5.7 \times 10^4$, which corresponds to a free-stream velocity (U_o) of approximately 20 m/s and 9.7 m/s when testing the small ($d = 0.043$ m) and large ($d = 0.089$ m) cylinder, respectively. To investigate the effect of wall adaptation on the flow development over the circular cylinder model, surface pressure measurements and wake velocity measurements were carried out in the GSW, ASW, and SLW configurations for all the blockage ratios tested. Surface pressure measurements on the cylinder serve to determine pressure drag, base suction, and the angle of flow separation. Velocity measurements in the wake aim to characterize vortex development through the determination of vortex formation length, shear layer instability frequency, and wake vortex shedding frequency. In addition, velocity measurements serve to identify the time-averaged wake development.

5.1 Mean Pressure Distributions on Cylinder and Drag

The goal of this section is to identify the effect of wall adaptation on mean cylinder surface pressure distributions. Surface pressure distributions were measured in the GSW, ASW, and SLW configurations and are shown in Figs. 5.1a, 5.1b, and 5.1c, for blockages of 17%, 8%, and 5%, respectively. Due to symmetry of the model, only the pressure on the upper half of the cylinder was measured. Pressure at 70 angular positions was measured throughout the range of $0^\circ \leq \theta \leq 180^\circ$ (refer to Fig. 3.3, pg. 33 for coordinate system). The spacing between measurement locations was 1° in regions of interest (e.g., stagnation, peak suction, separation) and was increased to 5° for $90^\circ \leq \theta \leq 180^\circ$, since this region is categorized by a nearly constant pressure (e.g., Okamoto & Takeuchi, 1975). At each angular location, the pressure transducer signal was sampled at 5000 Hz and averaged over 20 seconds.

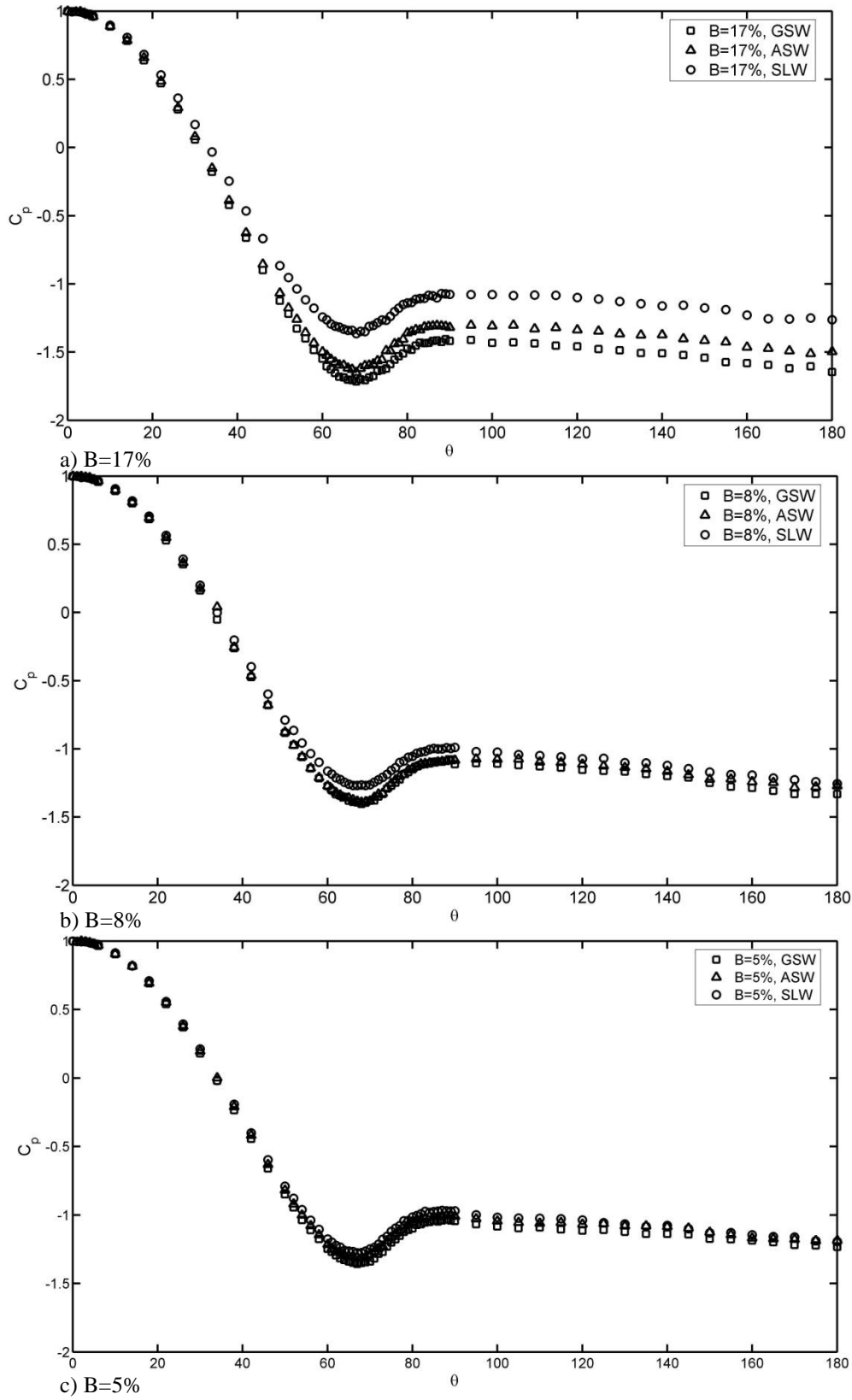


Figure 5.1 Mean cylinder surface pressure coefficient distributions in the GSW, ASW, and SLW configurations for a) $B=17\%$, b) $B=8\%$, and c) $B=5\%$.

The most substantial effects of wall adaptation on pressure distributions occur for $B=17\%$ (Fig. 5.1a). For this blockage, the magnitude of the suction peak at $\theta \approx 68^\circ$ in the GSW configuration is the highest, and is substantially decreased in the SLW configuration. The suction peak in the ASW configuration is alleviated slightly relative to the GSW configuration; however, it is still significantly higher than that obtained in the SLW configuration. Similar to the results of wall pressure distributions, the increase in suction on the surface of the cylinder is predominantly due to solid blockage. The measured base pressure coefficients (C_p at $\theta = 180^\circ$) for all configurations and blockage ratios are shown in Table 5.1. For $B=17\%$, the base pressure coefficient is -1.65 in the GSW configuration, which is 28% greater than the expected base pressure coefficient of -1.29 , measured in low blockage studies (e.g., Roshko, 1993). In the ASW configuration, the measured base pressure coefficient increases relative to that in the GSW configuration; however, it is still lower than the expected value from Roshko (1993). Upon implementing the adaptive wall strategy, the base pressure coefficient measured in the SLW configuration is within 3% of the Roshko (1993) value. The trend of decreasing base pressure coefficient is an important observation, since the base pressure is related to the length of the vortex formation region. Williamson (1996) suggests that a decrease in base suction results in an increase in vortex formation length. The length of the vortex formation region is discussed in Section 5.5.

The same trends evident for 17% blockage are also observed for $B=8\%$; however, they are less pronounced, as seen in Fig. 5.1b. The base pressure coefficient of -1.33 in the GSW configuration increases to -1.27 and -1.26 in the ASW and SLW configurations, respectively. The percentage difference between the base pressures measured in the GSW and SLW configurations for $B=8\%$ is only 5%, as compared to the 24% difference for the

same wall configurations at 17% blockage. On the average, the percentage difference in pressure at each angular position between the GSW and SLW distributions is 9%. The pressure distributions for the ASW and GSW configurations are very similar.

For 5% blockage, the pressure distributions measured in each wall configuration are very similar; however, it is still noticeable that the C_p curve measured in the GSW configuration is lower than that measured in the ASW configuration and even more so relative to the SLW configuration. In fact, on the average, the GSW pressure distribution is 5% lower than the distribution measured in the SLW configuration. The uncertainty of the base pressure coefficient measurement is approximately 2.0% (or $C_p \pm 0.022$), therefore, the relatively small difference between the GSW and SLW curves is still statistically significant.

Table 5.1 Base pressure coefficient summary for B=17%, 8%, and 5% in the GSW, ASW, and SLW configurations.

B [%]	GSW	ASW	SLW
17	-1.65	-1.50	-1.26
8	-1.33	-1.27	-1.26
5	-1.23	-1.19	-1.16

The time averaged separation angle was estimated based on the location of the inflection point on the surface pressure distribution curve downstream of the suction peak (Zdravkovich, 1997). For $65^\circ \leq \theta \leq 90^\circ$, a 4th order polynomial curve was fit to each of the nine pressure distributions shown in Figs. 5.1 a-c, and the point of inflection for each polynomial was numerically calculated. Separation angles for all wall configuration and blockage ratio combinations are shown in Table 5.2. The uncertainty of the separation angle calculations is less than 0.5°. For $Re_d = 32,200$, Okamoto & Takeuchi (1975) show that the separation angle moves from 76° to 80° when the blockage ratio increases from B=10% to B=30%. Thus, it is expected that, for a given blockage, streamlining walls would move separation upstream, since blockage effects are being alleviated. Indeed, the result pertaining

to 17% blockage show the separation point determined in the SLW configuration moved 0.7° upstream relative to the separation angle calculated for the GSW configuration (Table 5.2).

For a blockage of 8%, the separation angle calculated in the GSW configuration is located farther downstream relative to its position in the ASW and SLW configurations, which are virtually identical. At 5% blockage, differences in separation angles calculated for each of the three wall configurations are negligible. The separation angles calculated for each of the nine pressure distributions shown in Fig. 5.1 a-c are within the range of $70^\circ < \theta < 81^\circ$, expected for laminar separation (Okamoto & Takeuchi, 1975). The effect of wall adaptation on separation angle is of further interest since previous experimental studies suggest it is related to the width of the near wake. Zdravkovich (1997) indicates that the near wake width decreases as the separation point moves downstream. Wake widths are investigated in Section 5.3.

Table 5.2 Angle of separation summary for B=17%, 8%, and 5% in the GSW, ASW, and SLW configurations.

B [%]	GSW	ASW	SLW
17	75.9	75.8	75.2
8	75.1	74.5	74.6
5	74.0	73.9	74.0

It is of interest to identify the effect of wall adaptation on pressure drag. In general, total drag is comprised of friction drag and pressure drag (White, 2008). For flow over a cylinder at this Reynolds number, friction drag only contributes about 1.4% to the total drag (Okamoto & Takeuchi, 1975). Thus, for this investigation, only pressure drag is calculated. Pressure drag coefficient was calculated by integrating surface pressure distributions shown in Fig. 5.1 a-c. Numerical integration of the pressure distributions was conducted using the trapezoid rule and the source code for this procedure was written in MATLAB. The calculated pressure drag coefficients for all wall configuration and blockage ratio

combinations are shown in Table 5.3. Consistent with previous straight-wall blockage investigations, e.g., Okamoto & Takuechi (1975) and West & Apelt (1982), pressure drag increases with increasing blockage ratio in the GSW configuration. Specifically, for B=17%, the pressure drag coefficient of 1.40 is 17% greater than the expected total drag value of 1.20, reported at low blockage ratios (e.g., Lim & Lee, 2004). Although the pressure drag in the ASW configuration is reduced by 9% from the value in the GSW configuration, it is still above the value expected for low blockage ratios. Upon streamlining the walls, the pressure drag is reduced to 1.18, which is within 2% of the reported value at low blockage ratios.

For B=8%, the pressure drag is the highest in the GSW configuration, followed by the ASW and SLW configurations. Although a difference in drag did occur in the wall configurations at B=8%, only a 4% difference separates the pressure drag in the GSW configuration from that in the SLW configuration.

For B=5%, wall streamlining has a negligible effect on the pressure drag. Thus, pressure drag is invariant with wall configuration for a blockage ratio of 5%. This finding supports the result of Okamoto & Takeuchi (1975) and West & Apelt (1982), who conclude that drag is unaffected for blockages less than 4% and 6%, respectively.

Table 5.3 Pressure drag coefficients summary for B=17%, 8%, and 5% in the GSW, ASW, and SLW configurations.

B [%]	GSW	ASW	SLW
17	1.40	1.30	1.19
8	1.22	1.20	1.17
5	1.17	1.15	1.15

The above discussion is based on the analysis of pressure distributions which are grouped as a function of blockage ratio. It is of interest to directly compare the pressure distributions measured in the SLW configuration for each blockage ratio along with a pressure distribution measured at a low blockage ratio. Figure 5.2 shows the pressure

distributions measured in the SLW configuration for blockages of 5%, 8% and 17%. In addition, the pressure distribution measured by Okamoto & Takeuchi (1975) at $Re_d = 32,200$ and $L/d = 24$ is shown as a reference.

As shown in Fig. 5.2, the pressure distribution obtained at low blockage ratio by Okamoto & Takeuchi (1975) deviates slightly from the pressure distribution measured for $B=5\%$ in the SLW configuration. Specifically, the Okamoto & Takeuchi (1975) pressure curve is higher than that obtained for $B=5\%$ in the SLW configuration. However, the discrepancy is relatively minor and is likely attributed to the difference in Re_d and L/d . Specifically, the increased pressure may be in part due to a higher aspect ratio of the cylinder used in the Okamoto & Takeuchi (1975) study as compared to that for $B=5\%$ ($L/d=24$ versus $L/d=14$). In addition, the Reynolds number used in the Okamoto & Takeuchi (1975) investigation is lower than the current study. In light of the variance in influencing parameters, the small discrepancies between the Okamoto & Takeuchi (1975) and $B=5\%$ pressure distributions are reasonable, and the Okamoto & Takeuchi (1975) is considered to be a valid reference for the current investigation.

It is of particular interest to compare the pressure distributions measured in the SLW configuration for each of the blockage ratios. This comparison is imperative since it determines the effectiveness and repeatability of the adaptive wall strategy for the removal of blockage effects. As shown in Fig. 5.2, the pressure distribution for $B=5\%$ and $B=8\%$ are virtually identical, although a small discrepancy occurs in the region of $\theta \approx 160^\circ$. The average error between $B=5\%$ and $B=8\%$ at each angular position is 1.9%, which is within the experimental uncertainty of the pressure measurements. The aspect ratio and Reynolds

number for $B=5\%$ and $B=8\%$ are identical, so the equality of the two curves is anticipated assuming the effectiveness of the adaptive-wall strategy.

From Fig. 5.2, it is clear that the pressure distribution measured in the SLW configuration for $B=17\%$ is lower than that measured for $B=8\%$ and $B=5\%$. For $B=17\%$, a stronger suction is evident, as well as a lower base pressure coefficient. This discrepancy may be attributed to the influence of the aspect ratio. The small diameter cylinder ($L/d = 14$) was used for $B=5\%$ and $B=8\%$, while the large diameter cylinder ($L/d = 7$) was used for $B=17\%$. As discussed in Section 3.6, West & Apelt (1982) conclude that decreasing aspect ratio lowers the pressure distribution curves. This trend is evident in Fig. 5.2 and therefore the influence of aspect ratio is quite possibly the reason for the deviation between the pressure distributions obtained for $B=5\%$ and 8% versus that obtained for $B=17\%$. Thus, based on the results of Fig. 5.2, it can be concluded that the adaptive-wall strategy effectively removes blockage effects when all other influencing parameters are held constant.

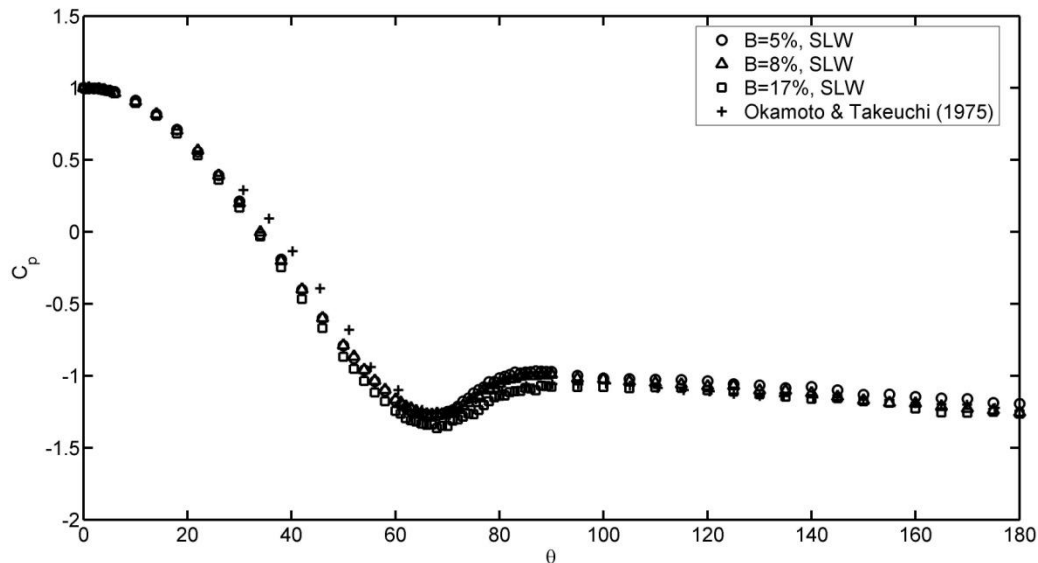


Figure 5.2 Mean cylinder surface pressure coefficient distributions in the SLW configuration for $B=17\%$, 8% , and 5% .

5.2 RMS Pressure Distributions on Cylinder

In addition to important parameters derived from mean cylinder surface pressure distributions (e.g., drag, separation angle), fluctuating pressure distributions are also important, as they relate to fluctuating forces, critical in structural design. The goal of this section is to identify the effect of wall adaptation on time-resolved surface pressure distributions, represented here by normalized RMS surface pressure fluctuations. The large cylinder ($d = 0.089$ m) contained an embedded pressure transducer (All Sensors, 4V-D2-MINI). A tube of 8 mm length with an internal diameter of 1.02mm was used to connect the pressure tap to the piezoresistive transducer. The frequency response of the sensor was measured and its natural frequency was determined to be 890Hz. The frequency response curve indicated that the transducer is capable of resolving low frequencies (e.g., wake vortex shedding), but not capable of detecting high frequencies (e.g., instability frequency). The signals from the transducer were sampled at 5000 Hz for a duration of 20 seconds. The same angular spacing used in the mean pressure measurements was utilized for the time-resolved measurements. The RMS surface pressure coefficient is defined as the RMS of the differential pressure ($P - P_o$) divided by the dynamic pressure of the free-stream ($0.5\rho U_o^2$).

The distribution of RMS surface pressure coefficient ($C_{p'}$) pertaining to the three wall configurations investigated at $B=17\%$ are shown in Fig. 5.3. For all wall configurations, $C_{p'}$ increases from a minimum at the stagnation point to a maximum located near the separation angle, agreeing with previous experimental results presented by Norberg (2003). The angles corresponding to maximum $C_{p'}$ are shown in Table 5.4 along with results obtained by Norberg (2003). The angle of max $C_{p'}$ calculated for the GSW configuration was 1° downstream of the angles calculated for the ASW and SLW configurations. This trend

suggests that separation is delayed in the GSW configuration, agreeing with the results for the separation angles detailed in Section 5.1. It is concluded that wall configuration has little effect on C_p magnitude, but streamlining the walls causes separation to move 1° upstream.

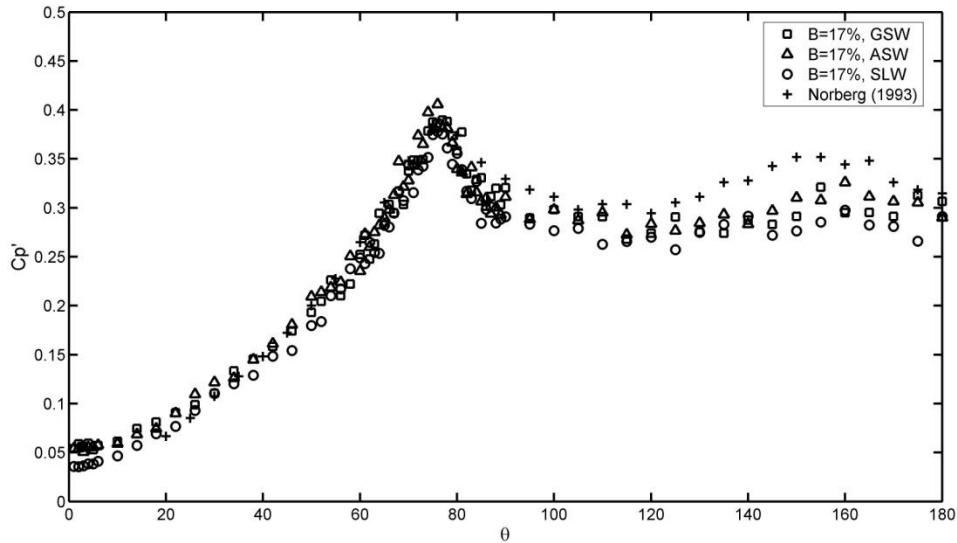


Figure 5.3 RMS surface pressure coefficient distribution in the GSW, ASW, and SLW configurations for $B=17\%$.

Table 5.4 Summary of RMS surface pressure coefficient distributions in the GSW, ASW, and SLW configurations for $B=17\%$.

	$Re / 10^4$	$C_{p', \max}$	θ ($^\circ$) at $C_{p', \max}$
GSW	5.8	0.39	77
ASW	5.8	0.40	76
SLW	5.8	0.38	76
Norberg (2003)	6.1	0.38	77

5.3 Mean Wake Development

The goal of this section is to determine the effect of wall adaptation on mean wake velocity development. For each wall configuration, the three probe rake holder was traversed in the wake to obtain mean wake velocity profiles. The probes were traversed with a vertical pitch of $y/d = 0.05$ and $y/d = 0.09$ for streamwise locations $x/d \leq 9.0$ and $x/d > 9.0$, respectively. At each spatial location, the hot-wire signals were sampled at a rate of 5000 Hz for a duration of 20 seconds. From the mean wake velocity profiles, wake shape, wake width, and wake

velocity deficits were determined. Only the upper half of the wake was measured due to flow symmetry. Wake profiles obtained for $B=17\%$, 8% , and 5% are shown in Figs. 5.4, 5.5, and 5.6, respectively. To facilitate a comparison of the results, each mean velocity profile is normalized by the local free-stream velocity, U_o^* (i.e., each profile is normalized such that the normalized velocity outside the wake is unity).

In the near wake ($x/d < 4$) for $B=17\%$, the results show that the profiles measured in the GSW configuration (Fig 5.4a) and those measured in the ASW configuration (Fig. 5.4b) are shallower than those measured in the SLW configuration (Fig. 5.4c), i.e., the velocity increases with vertical direction at a higher rate for the GSW and ASW configurations relative to the SLW configuration. In addition, no significant difference is observed between wake velocity profiles measured in the GSW and ASW configurations for $x/d = 6.5$ and $x/d = 9.0$ at vertical locations of $y/d > 1.5$. This suggests that the wake growth is limited for $x/d \geq 6.5$, which is an indication of wake blockage. In contrast, the results show that the wake continues to expand in the SLW configuration for $x/d > 6.5$, which suggests that streamlining the walls enables wake growth, otherwise limited in the ASW and GSW configurations.

As shown in Fig. 5.5 for $B=8\%$, the wake is allowed to expand with increasing x/d for each wall configuration. This indicates that wake blockage is not as significant for $B= 8\%$ compared to $B=17\%$. Similar to 8% blockage, measurements made at $B=5\%$ indicate that the wake is allowed to grow uninhibited for all streamwise locations in the GSW and SLW configurations as shown in Fig. 5.6. Thus, it can be concluded that effects of wake blockage are negligible at this blockage ratio. Given the small effects of blockage observed in the pressure distributions for $B=5\%$ between the ASW and SLW configurations, velocity profiles in the ASW configuration for $B=5\%$ were not obtained.

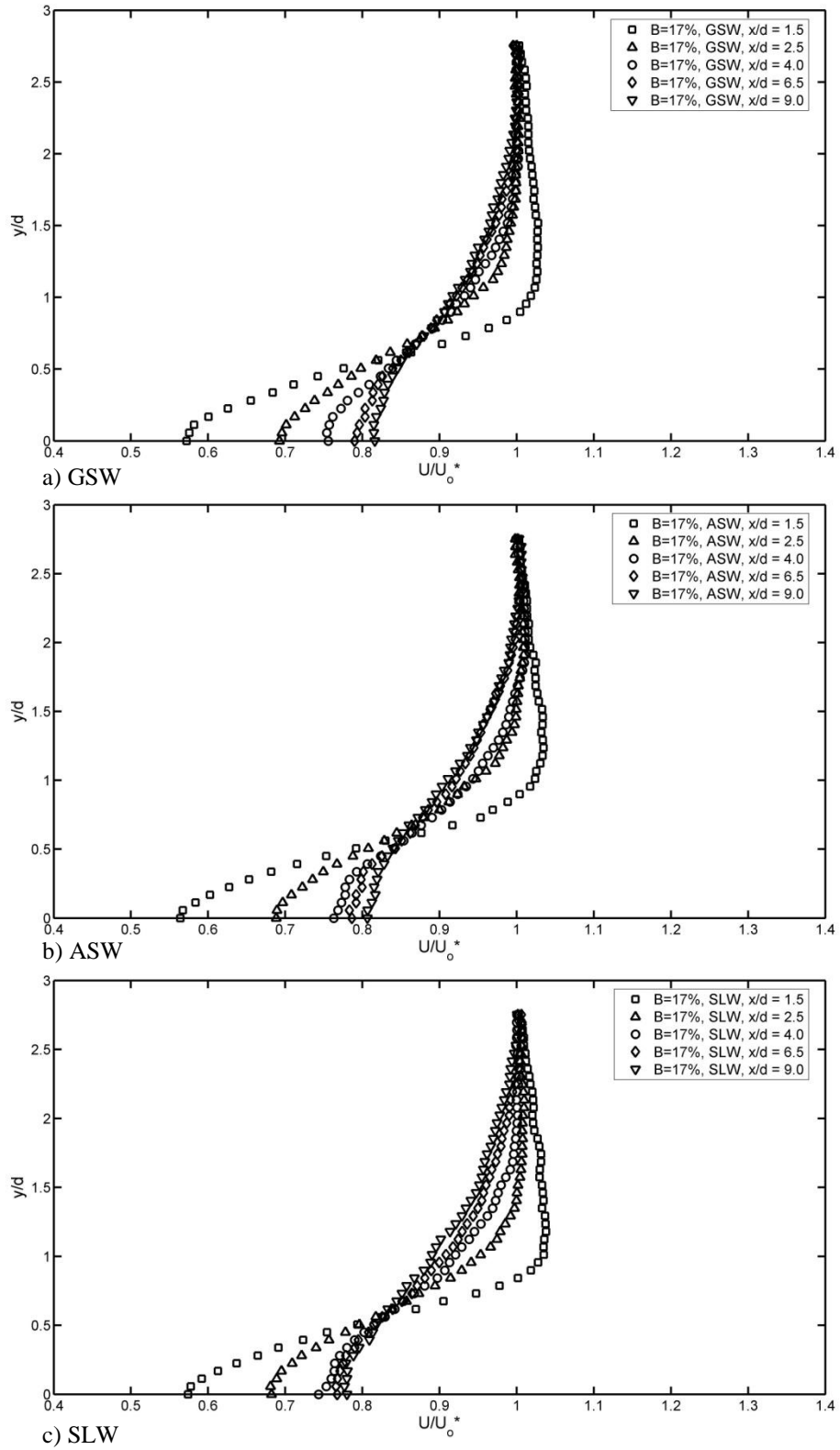


Figure 5.4 Mean velocity profiles from cross-wire probe for $B=17\%$ in the a) GSW, b) ASW, and c) SLW configurations.

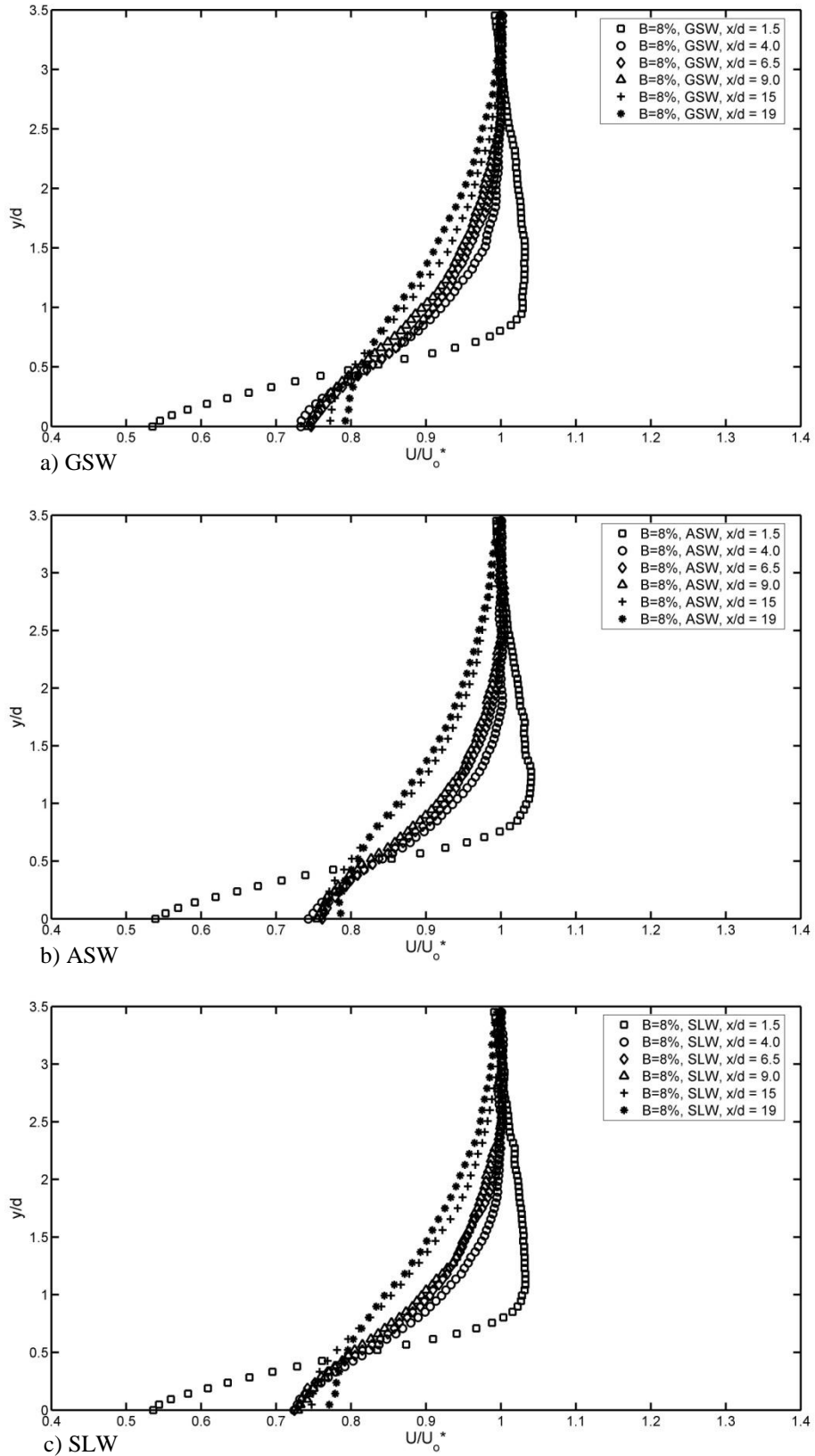


Figure 5.5 Mean velocity profiles from cross-wire probe for $B=8\%$ in the a) GSW, b) ASW, and c) SLW configurations.

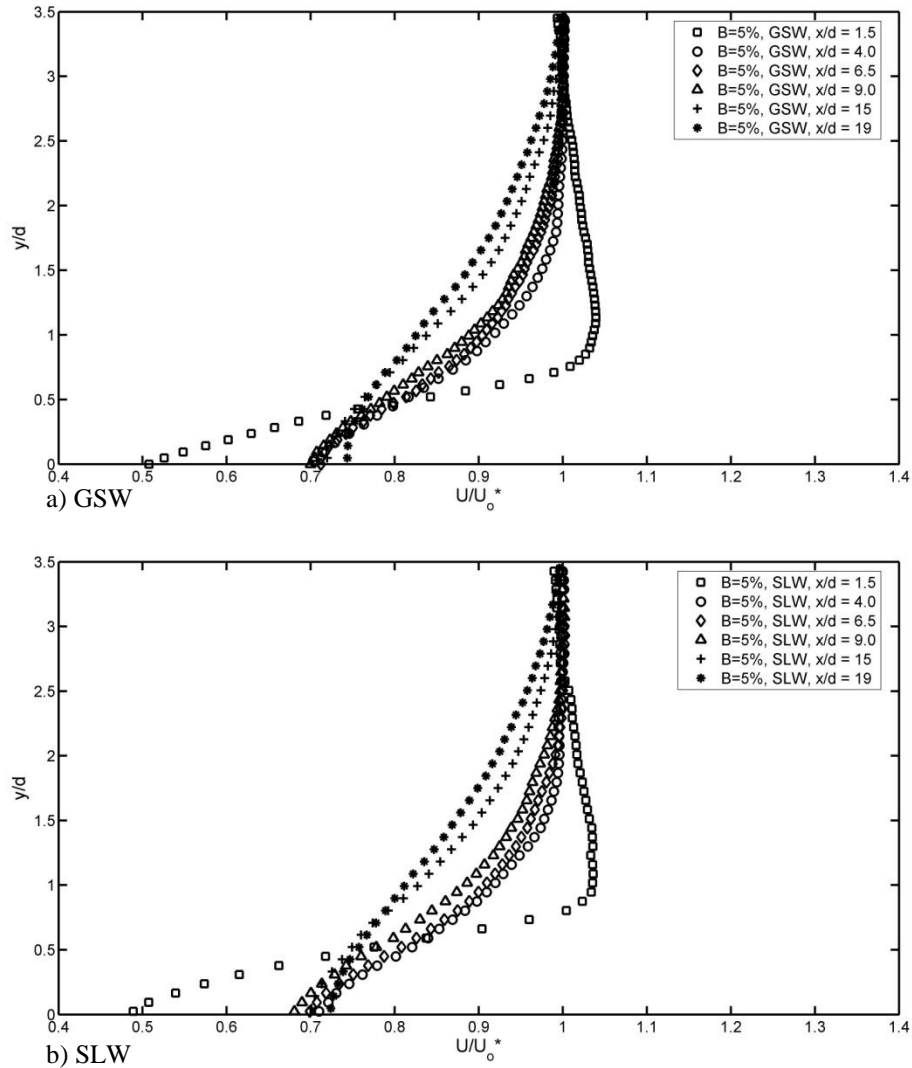


Figure 5.6 Mean velocity profiles from cross-wire probe for B=5% in the a) GSW and b) SLW configurations.

To further classify mean wake velocity development, the mean half wake width (b) for each velocity profile was determined and plotted against the streamwise distance (x/d). For estimating the normalized mean half wake width (b/d), the edge of the wake was defined as the y/d location corresponding to $U/U_0^* = 0.98$. The value of $U/U_0^* = 0.98$ was chosen since it represents a difference greater than experimental uncertainty of the free-stream velocity. As shown in Fig. 5.7, the wake growth for B=5% has no significant differences between the GSW and SLW configurations.

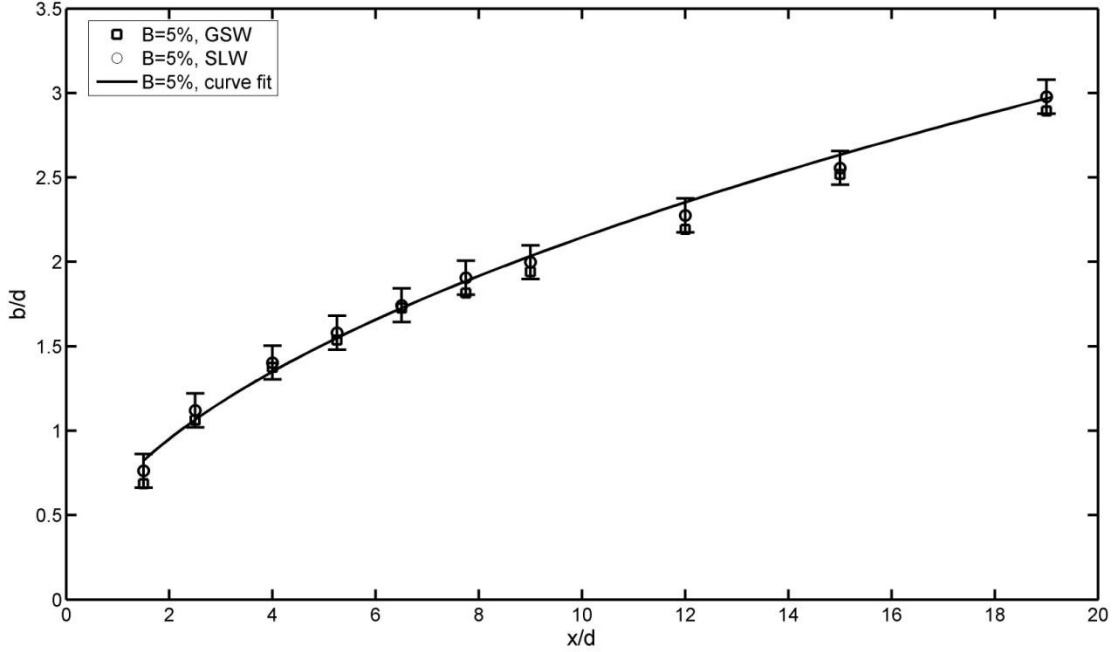


Figure 5.7 Mean half wake width growth for B=5% in the GSW and SLW configurations.

For low blockages, Schlichting (1930) determined that the mean half wake width (b) is proportional to $x^{0.5}$. Based on the wake width pertaining to the SLW configuration, a power-law curve shown in Fig. 5.7 is given by Eq. 5.1.

$$\frac{b}{d} = 0.67 \left(\frac{x}{d} \right)^{0.51} \quad (5.1)$$

Thus, the results suggest that b is proportional to $x^{0.51}$, which is in agreement with the result from Schlichting (1930) and confirms that wake blockage is negligible for $B \leq 5\%$.

The downstream growth of the mean half wake width is shown in Figs. 5.8 and 5.9 for $B=17\%$ and $B=8\%$, respectively. The curve fit obtained for $B=5\%$ in the SLW configuration (Eq. 5.1) is shown for comparison in Figs. 5.8 and 5.9.

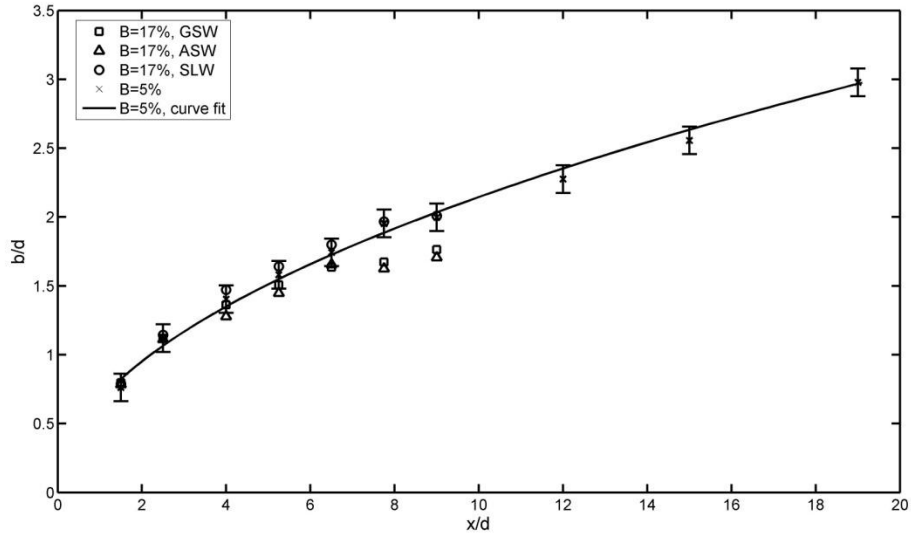


Figure 5.8 Mean half wake width growth for B=17% in the GSW, ASW, and SLW configurations.

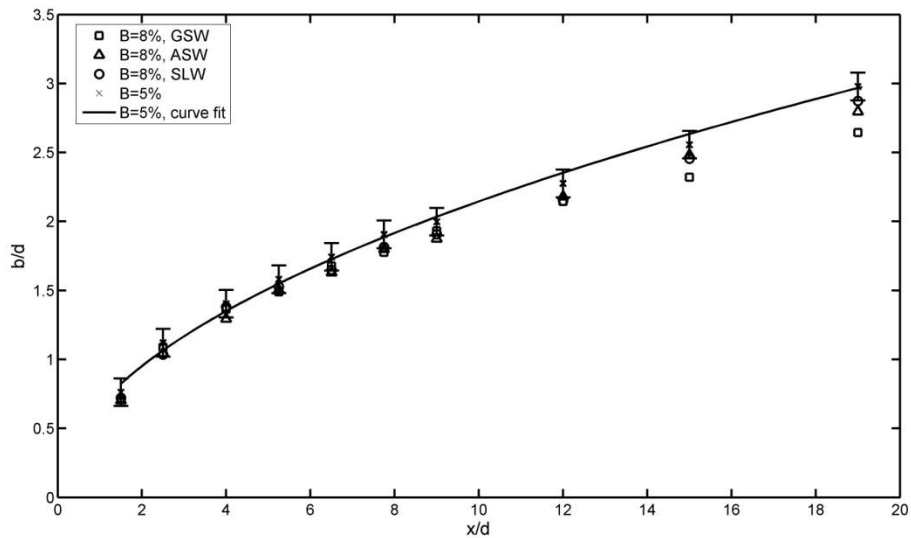


Figure 5.9 Mean half wake width growth for B=8% in the GSW, ASW, and SLW configurations.

For B=17%, the GSW, ASW, and SLW configurations show little difference in wake width for $x/d < 6.5$. However, at $x/d = 7.75$ and $x/d = 9.0$, the mean half wake widths deviate significantly from the curve obtained for $B = 5\%$. This indicates that wake blockage has a prominent influence on the wake development for $B = 17\%$. This limitation in wake growth is likely related to the increase in free-stream velocity outside the wake for $x/d > 6.5$. This increase in free-stream velocity can be deduced from the wall pressure distribution shown in Fig. 4.5a and the free-stream streamwise velocity profile shown in Fig. 4.7a. Upon

streamlining the walls, the wake is allowed to grow uninhibited and the growth rate matches that measured for $B=5\%$.

For 8% blockage (Fig. 5.9), the deviations between mean half wake widths measured in the GSW, ASW, and SLW configurations were within experimental error for $x/d \leq 9$. Fig. 5.9 shows that wake growth is limited starting at $x/d=15$ in the GSW configuration. Fig. 5.9 also suggests that wake width growth is checked starting at $x/d = 19$ in the ASW configuration. Similar to the results obtained for $B = 17\%$, streamlining the walls for $B=8\%$ results in a wake width development matching that measured for $B=5\%$. Based on these results, it can be concluded that streamlining walls using the wall adaptation strategy adequately corrects the growth of the wake for streamwise locations of $x/d \leq 19$ and blockages of up to and including 17%.

Another important characteristic in the cylinder wake is the velocity deficit. From Figs. 5.4-5.6, it is interesting to note that, for a given streamwise location, the characteristic velocity deficit, i.e., $(U_o^* - U_{y=0})/ U_o^*$, increases as the wall configuration is changed from GSW to ASW and to SLW. To more clearly illustrate this trend, the characteristic velocity deficit is plotted versus streamwise location (x/d) in Fig. 5.10 for all the combinations of wall configurations and blockage ratios investigated. The results show that for a given blockage ratio, the characteristic velocity deficit increases as walls are streamlined. This could be a consequence of wake blockage effects, as Zdravkovich (2003) states that wake blockage tends to decrease pressure inside the core of the wake, which would correspond to a higher velocity. Therefore, it would be expected that velocity would decrease in the core of the wake when wake blockage effects are removed, i.e., as walls are streamlined. An interesting observation is that the velocity deficit measured in the SLW configurations at each blockage

ratio do not converge to the same curve. Based on the results in Fig. 5.10, a definitive conclusion for the effect of wall adaptation on mean velocity deficit cannot be reached.

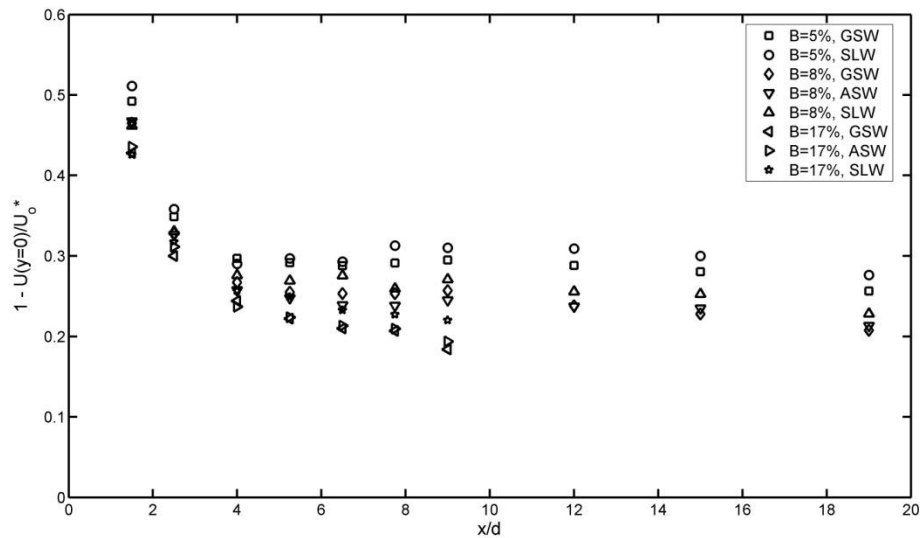


Figure 5.10 Characteristic wake velocity deficits.

The near wake development is of particular interest since it relates to wake vortex formation. Zdravkovich (2003) suggests that the width of the near wake is inversely proportional to the Strouhal number, i.e., as wake width decreases, Strouhal number increases and vice versa. To identify the effect of wall adaptation on near wake velocity profiles, mean streamwise velocity profiles obtained at $x/d = 1.5$ in the GSW, ASW, and SLW configurations are shown in Fig. 5.11a, 5.11b, and 5.11c, for blockages of $B=17\%$, 8% , and 5% , respectively. To highlight the effect of solid blockage, each mean velocity profile is normalized by the free-stream velocity (U_0) measured at the entrance of the test section. The results show that solid blockage increases flow speed outside the wake in the GSW configurations for all blockage ratios. The increase in speed is especially prevalent in the GSW configuration for $B=17\%$, as the flow reaches a maximum speed of $U/U_0 = 1.18$ versus 1.10 and 1.09 measured for $B=8\%$ and $B=5\%$, respectively.

As a method to categorize the shape of the near wake, linear curves were fit to the region of $0.25 \leq y/d \leq 0.80$ and resulting equations and corresponding square of the correlation coefficients (r^2) are shown in Fig. 5.11. For $B=17\%$, the maximum velocity gradient ($\Delta U / \Delta y$) is 10% greater in the GSW configuration relative to the SLW configuration, which indicates that streamlining walls alleviates high velocity gradients caused by solid blockage. The differences in gradients between the GSW and SLW configurations for $B=8\%$ and $B=5\%$ were reduced relative to $B=17\%$ and calculated to be 3%, and 0.8%, respectively. From these plots, it can be concluded that, for high blockages ($B=17\%$), wall adaptation affects the development of the wake velocity profiles.

In addition to mean streamwise velocity profiles, mean vertical velocity profiles were obtained to further classify the effect of wall adaptation on near wake development. Vertical velocity profiles are shown in Figs. 5.12a, 5.12b, and 5.12c, for $B=17\%$, 8%, and 5%, respectively, at streamwise locations of $x/d = 1.5, 2.5,$ and 4.0 . Similar to the streamwise velocity profiles, the vertical velocity profiles are normalized by the free-stream velocity (U_0). As shown in Figs. 5.12a and 5.12b, vertical velocity reaches a maximum magnitude in the GSW configuration for $B=17\%$ and $B=8\%$. For both of these blockages, the magnitude of the maximum vertical velocity is reduced when walls are streamlined. For a blockage of 5%, the maximum vertical velocity is the same for the GSW and SLW configuration, although some deviation begins to occur as y/d increases due to solid blockage effects. The magnitude of the vertical velocity components are reduced at $x/d=2.5$ relative to $x/d=1.5$, but are still significant. By the streamwise location of $x/d=4.0$, the V component approaches zero, which indicates that the contribution of vertical velocity is only prevalent in the very near wake of the cylinder. From these results, it is clear that solid blockage not only increases streamwise

velocity across the wake, but also increases the vertical velocity component across the wake (for $x/d < 4$), especially for $B=17\%$ and $B=8\%$. For all blockages, the vertical location of the maximum vertical velocity is relatively invariant with wall configuration.

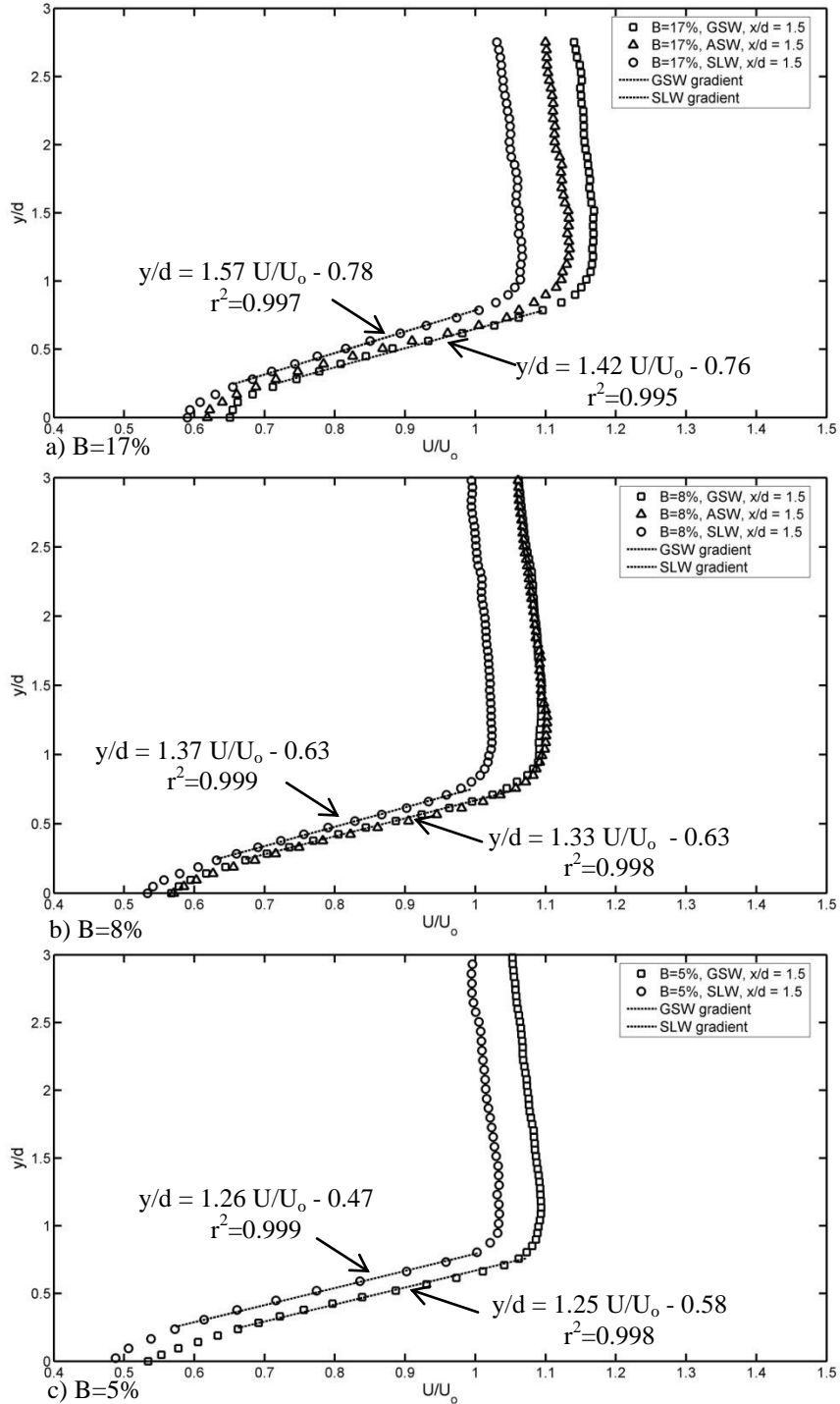


Figure 5.11 Mean wake streamwise velocity profiles at $x/d = 1.5$ in the GSW, ASW, and SLW configurations for a) $B=17\%$, b) $B=8\%$, and c) $B=5\%$.

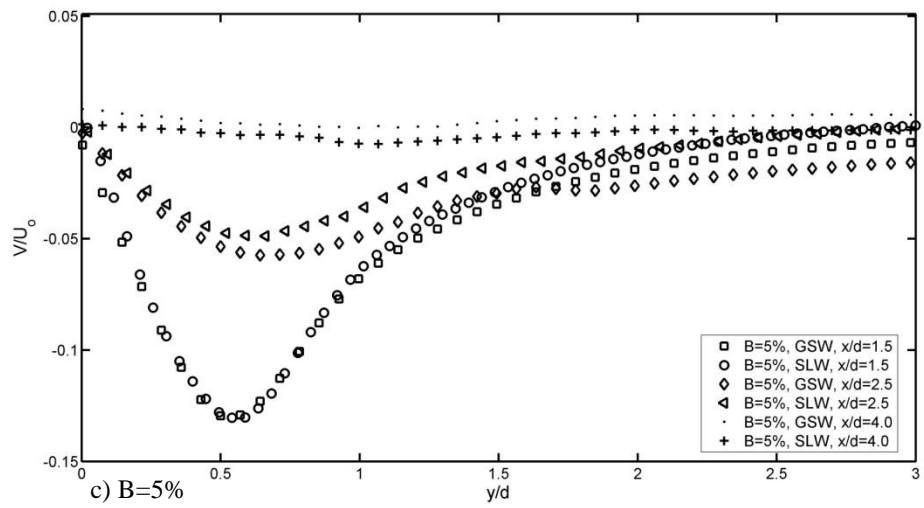
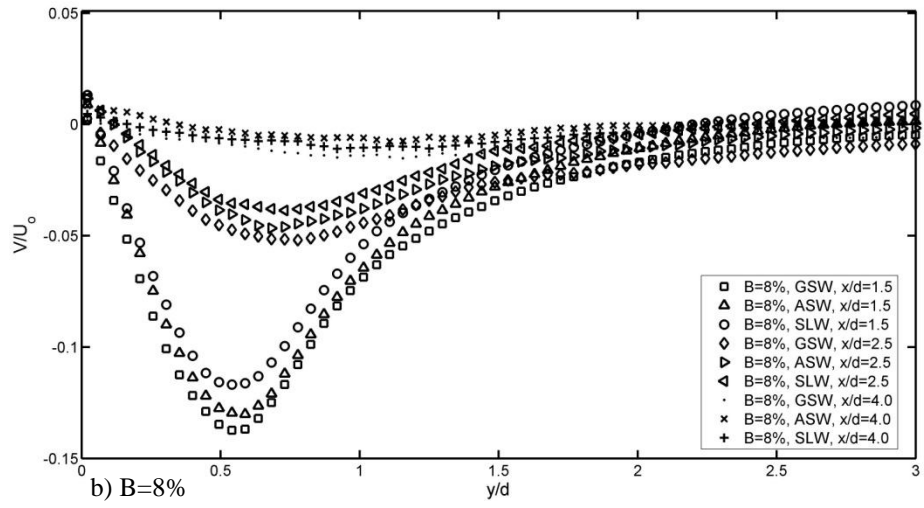
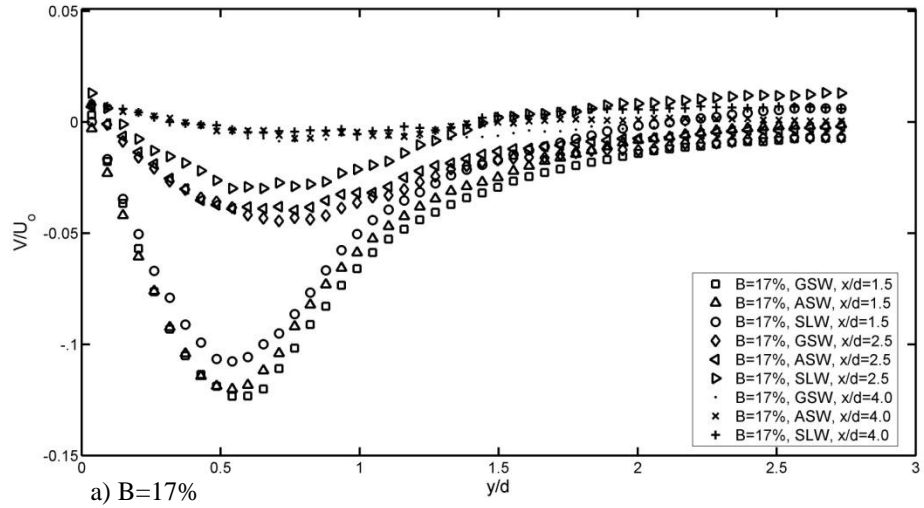


Figure 5.12 Mean wake vertical velocity profiles at $x/d = 1.5, 2.5,$ and 4.0 in the GSW, ASW, and SLW configurations for a) $B=17\%$, b) $B=8\%$, and c) $B=5\%$.

5.4 RMS Wake Velocity Profiles

The value and location of maximum RMS velocity in the wake profiles relates to the strength and diffusion of the wake vortices (Thomson & Morrison, 1971). RMS velocity profiles obtained for $B=17\%$, $B=8\%$, and $B=5\%$ are shown in Figs. 5.13, 5.14, and 5.15, respectively. Each profile is normalized by the free-stream velocity. For all blockages investigated, the magnitude of the maximum u'/U_o decreases as walls are streamlined. This is due to the alleviation of increased velocity caused by solid blockage. For $x/d \leq 4$, a peak in u'/U_o above $y/d = 0$ is evident in all wall configurations for each blockage. The location of this peak ($y/d \approx 0.52$) is constant for all combinations of wall configuration and blockage ratio.

The strength of a wake vortex can be related to two characteristic dimensions in the wake (Okamoto & Takeuchi, 1975). The first dimension is the streamwise distance between consecutive vortices on either side of the vortex street. The second dimension is the vertical distance between a wake vortex shed from the top surface of the cylinder and a consecutive vortex shed from the bottom surface. The determination of these two dimensions from wind tunnel measurements has historically proven to be difficult and typically requires flow visualization (Okamoto & Takeuchi, 1975). In the current study, utilizing flow symmetry of the cylinder, the vertical distance between wake vortices is estimated as twice the distance from $y/d=0$ to the location of maximum u'/U_o . From Figs. 5.16-5.18, it can be seen that this value remains the same for the investigated combinations of wall configurations and blockage ratios. For all the cases, the peak in RMS velocity profile occurs at $y/d \approx 0.52$. This suggests that the vertical spacing between wake vortices is not affected by blockage effects for $B \leq 17\%$. This finding agrees with the observed invariance of the wake width with the blockage ratio in the near wake, as shown in Figs. 5.7-5.9.

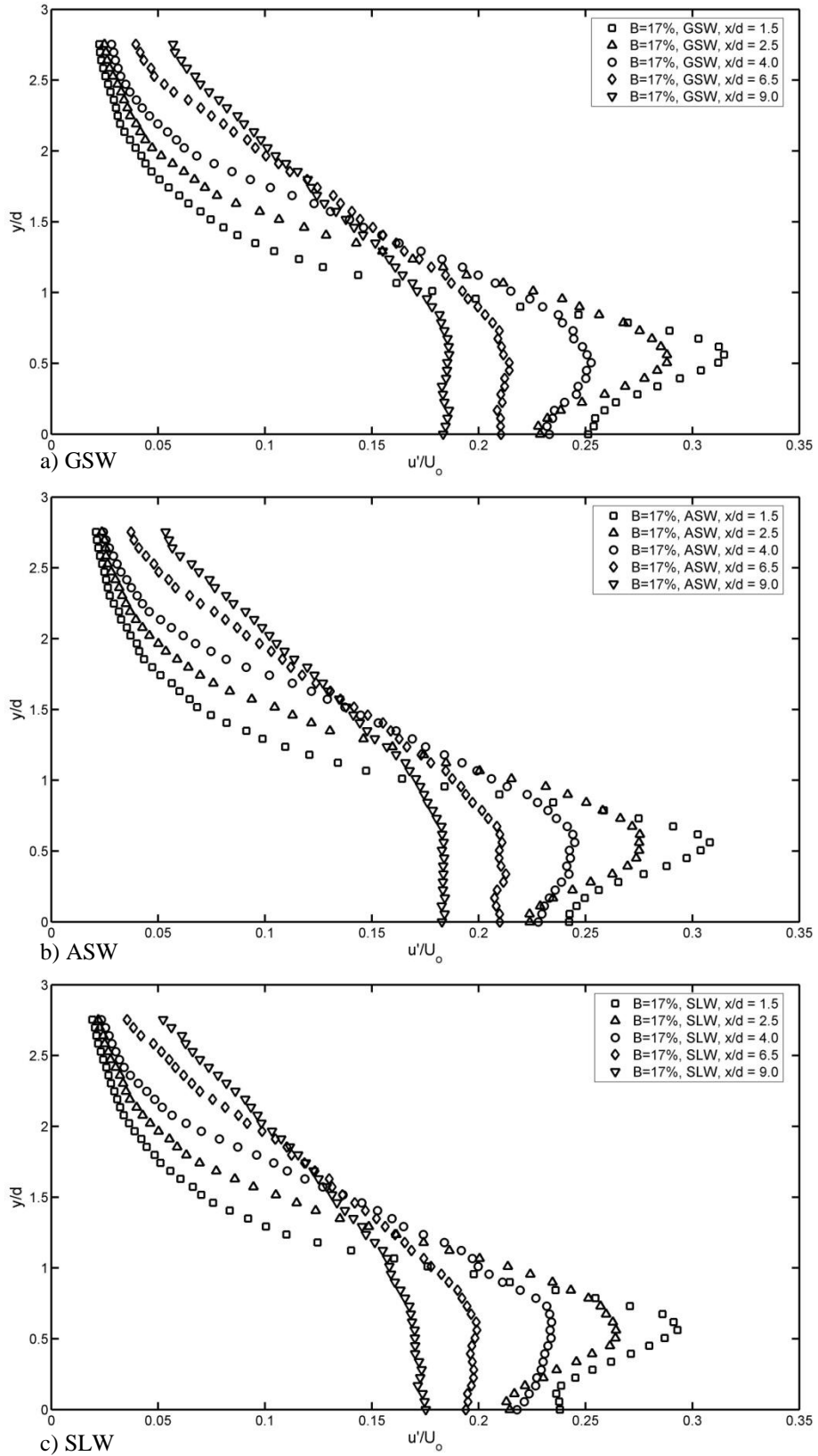


Figure 5.13 Streamwise RMS velocity profiles for $B=17\%$ in the a) GSW, b) ASW, and c) SLW configurations.

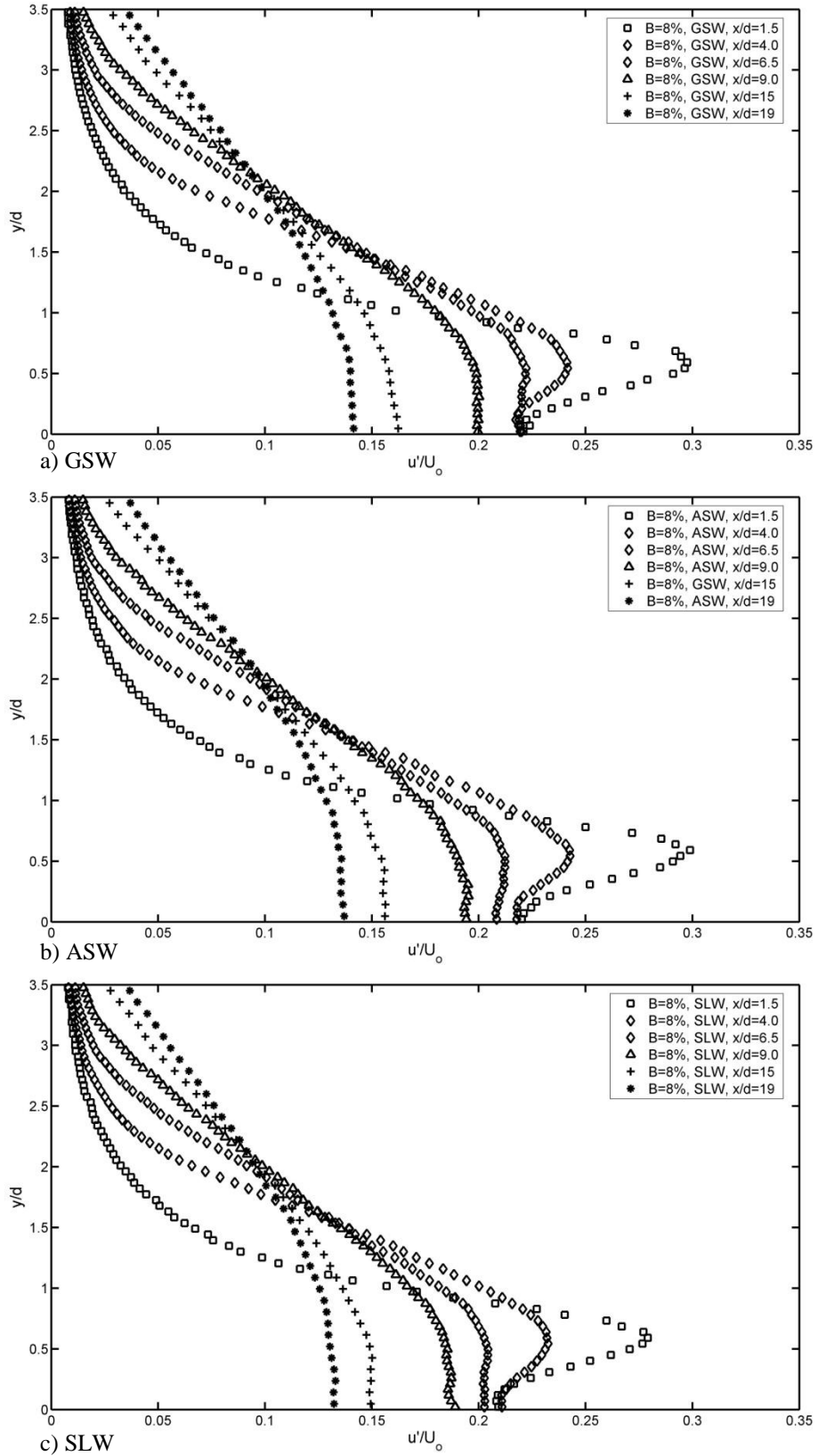


Figure 5.14 Streamwise RMS velocity profiles for $B=8\%$ in the a) GSW, b) ASW, and c) SLW configurations.

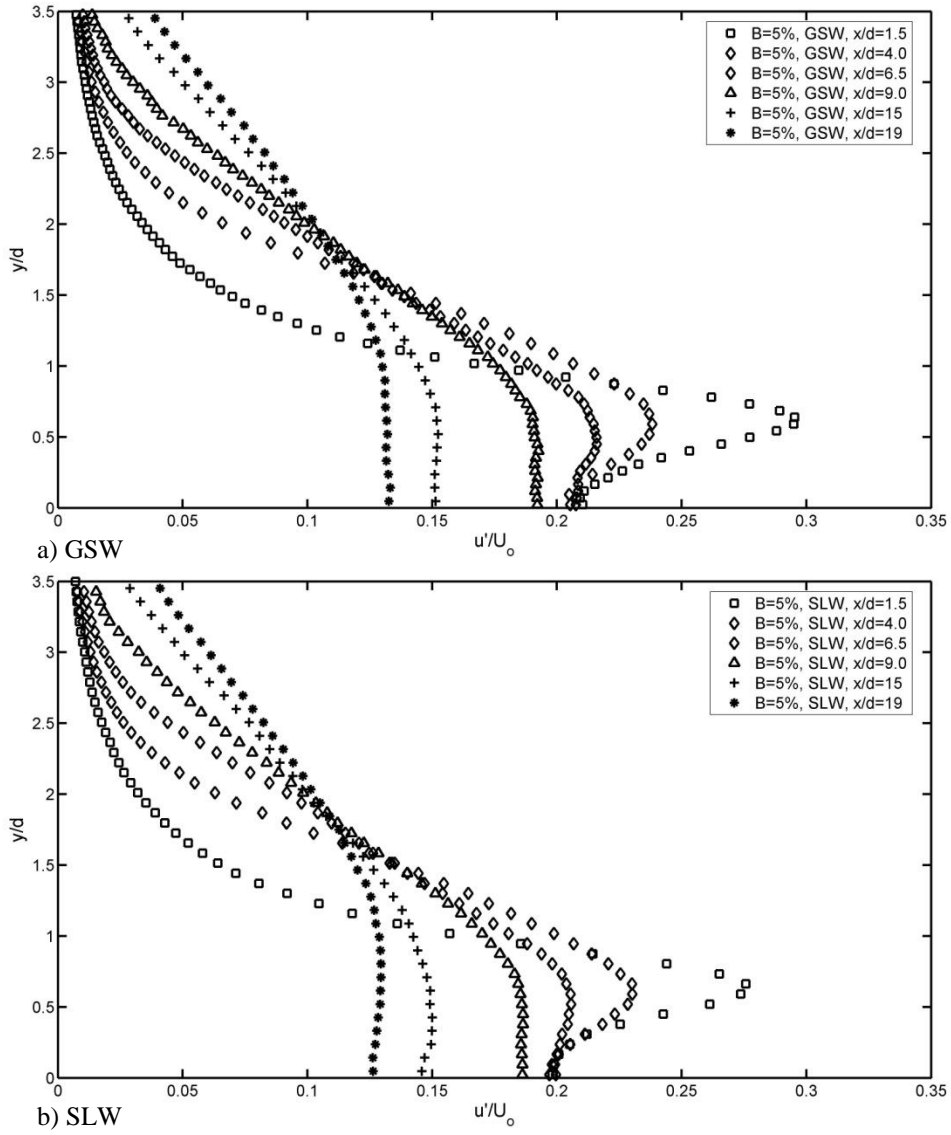


Figure 5.15 Streamwise RMS velocity profiles for $B=5\%$ in the a) GSW and b) SLW configurations.

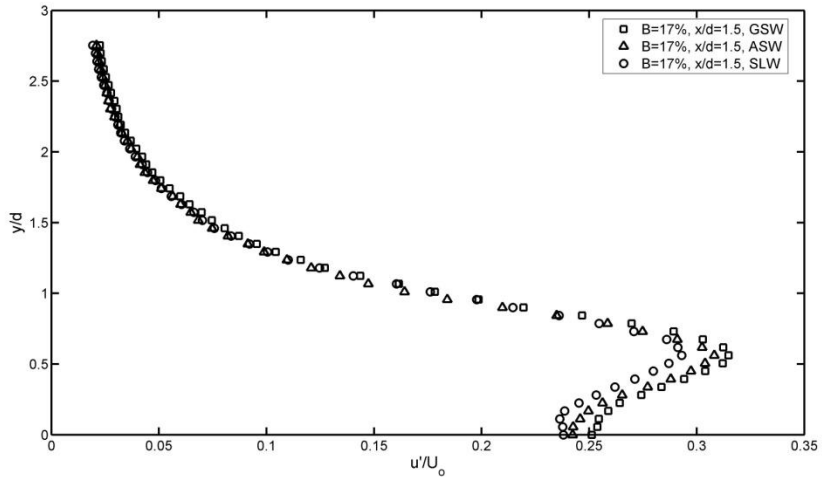


Figure 5.16 Streamwise RMS velocity profiles for B=17% in the GSW, ASW, and SLW configurations.

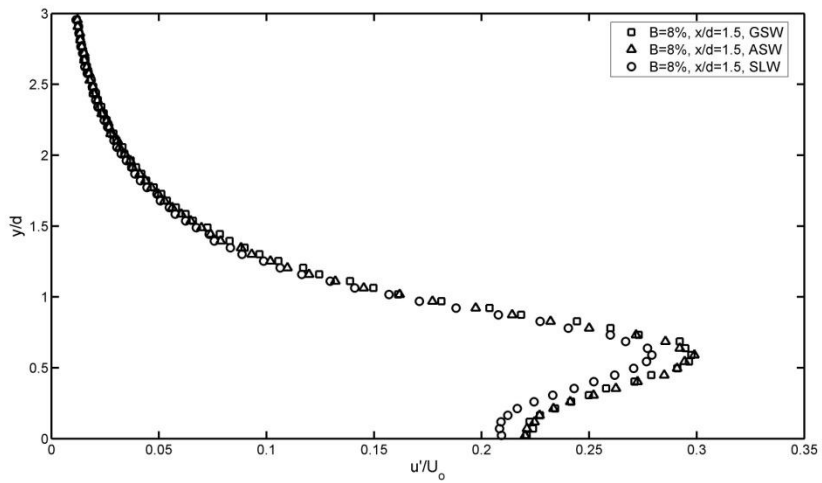


Figure 5.17 Streamwise RMS velocity profiles for B=8% in the GSW, ASW, and SLW configurations.

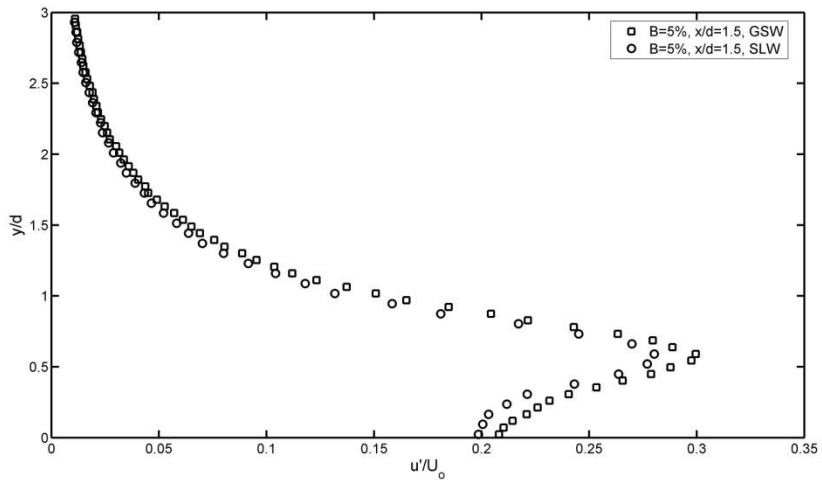


Figure 5.18 Streamwise RMS velocity profiles for B=5% in the GSW and SLW configurations.

In addition to streamwise RMS velocity profiles, vertical RMS velocity profiles obtained at $x/d=1.5$ are plotted in Figs. 5.19, 5.20, and 5.21 for $B=17\%$, 8% , and 5% , respectively.

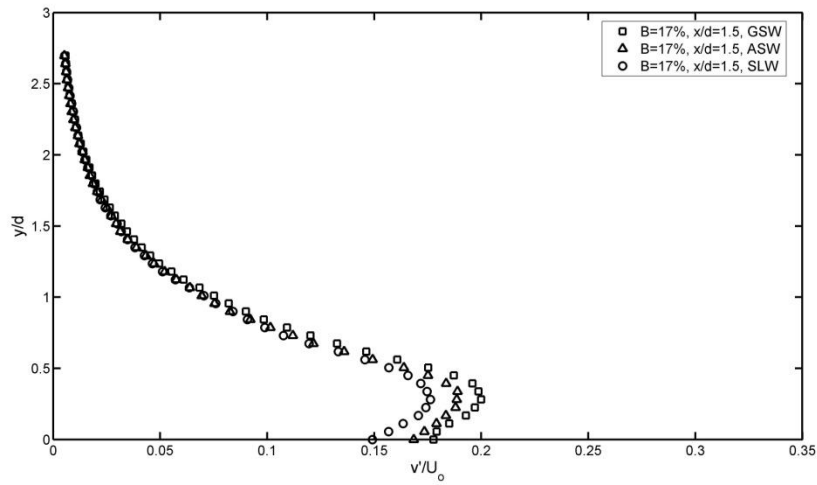


Figure 5.19 Vertical RMS velocity profiles for $B=17\%$ in the GSW, ASW, and SLW configurations.

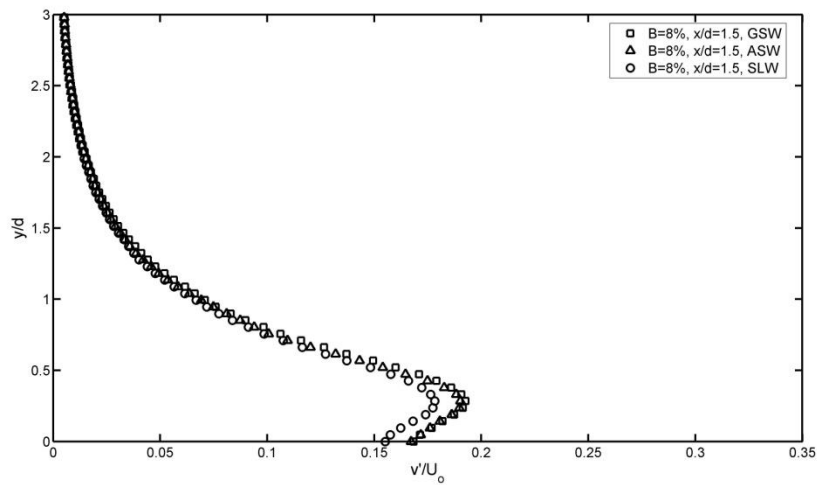


Figure 5.20 Vertical RMS velocity profiles for $B=8\%$ in the GSW, ASW, and SLW configurations.

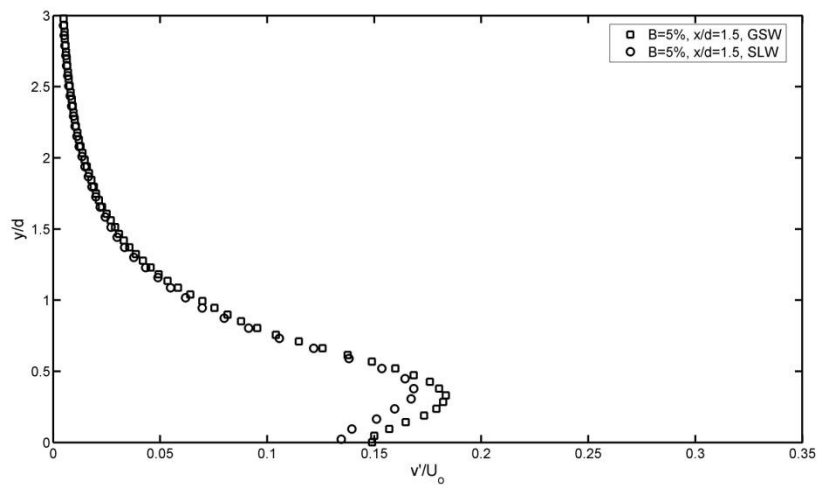


Figure 5.21 Vertical RMS velocity profiles for $B=5\%$ in the GSW, ASW, and SLW configurations.

For each blockage ratio the GSW configuration produces the highest magnitude of RMS in the vertical velocity profiles, similar to the streamwise profiles. The location of the maximum vertical RMS is $0.30d \pm 0.02d$ for all the investigated wall configurations and blockage ratios. This suggests that wall adaptation has negligible effect on peak RMS location, agreeing with the trend observed in streamwise RMS profiles.

Although the vertical distance between vortices is unaffected by the wall configurations tested for $B=5\%$, 8% , and 17% , one cannot necessarily imply that vortex strength remains invariant. To make this conclusion, flow visualization would have to be completed, so as to determine all parameters required for estimating vortex strength.

5.5 Vortex Formation Region

The goal of this section is to identify the effect of wall adaptation on the vortex formation region. The length of the vortex formation region is defined as the distance from the cylinder axis to the streamwise location of maximum turbulence intensity (u'/U_o) along the centerline of the cylinder, i.e., $y/d = 0$. All measurements were conducted using the normal hot-wire probe, since it has lower uncertainty associated with RMS velocity measurement in the near wake as compared to the cross-wire probe (Kawall et al., 1983). In the region near maximum u'/U_o the streamwise pitch of the traverse was refined to $0.02d$, compared to $0.05d$ in the region of RMS decay, in order to have a better resolution in the determination of vortex formation length. Figures 5.22a, 5.22b, and 5.22c show the corresponding streamwise u'/U_o profiles for $B=17\%$, 8% , and 5% , respectively. A 6th order polynomial curve fit was used for the RMS data sets shown in Figs. 5.22 a-c to estimate the location of maximum turbulence intensity. As shown in Fig. 5.22, each RMS distribution reaches a definitive peak, marking the

end of the vortex formation region. The calculated vortex formation lengths are summarized in Table 5.5.

Table 5.5 Vortex formation lengths for all blockage ratio and wall configuration combinations.

B [%]	GSW	ASW	SLW
17	1.37d	1.31d	1.30d
8	1.40d	1.42d	1.40d
5	1.48d	1.49d	1.50d

For the highest blockage tested, $B=17\%$ (Fig. 5.22a), the highest peak magnitude of u'/U_o occurs in the GSW configuration due to solid blockage effects. The formation length in the GSW configuration is measured to be $0.02d$ and $0.07d$ longer than the formation lengths measured in the ASW and SLW configurations, respectively. The formation length reduction from the GSW to SLW configurations is statistically significant, as it is beyond the resolution of $\pm 0.02d$. Recall from Fig. 5.1 that streamlining the walls decreases the base suction coefficient. Bearman (1965) concludes that the vortex formation length is inversely proportional to the base suction. If this relationship held true for the current study, it would be expected that the GSW configuration would have the shortest formation length, since it had a higher base suction coefficient relative to the ASW and SLW configurations. Clearly, for $B=17\%$, this is not the case as the formation length decreases with streamlining the walls (Table 5.3). The observed reduction in formation length from GSW to SLW may be due to the diminished near wake velocity gradients in the SLW configuration, as compared to that in the GSW configuration (Fig. 5.11a).

For $B=8\%$, similar to $B=17\%$, the GSW configuration features the highest magnitude of u'/U_o due to blockage effects (Fig. 5.22b). All formation lengths calculated for $B=8\%$ in each wall configuration are longer than the formation lengths measured for $B=17\%$. Care must be taken, however, when comparing the formation lengths calculated for $B=8\%$ to the

formation lengths calculated for $B=17\%$, since influencing parameters are not constant. Zdravkovich (2003) notes that decreasing the aspect ratio elongates the vortex formation region. This trend is not found in the current study as $B=17\%$ ($L/d=7$) has a shorter formation length relative to that measured for $B=8\%$ ($L/d=14$). In addition to aspect ratio, Reynolds number also influences vortex formation length. Linke (1931) and Bloor (1964) show that vortex formation length decreases with increasing Re_d within the current flow regime. Given the increased speeds (i.e., effectively increased Re_d) associated with blockage at $B=17\%$ relative to $B=8\%$, the change in formation lengths between the two blockage ratios may be due to the Re_d effects. Within the wall configurations for $B=8\%$, the differences in vortex formation lengths did not deviate more than the uncertainty associated with the measurement itself. This result suggests that, for $B=8\%$, wall adaptation has little effect on the vortex formation length.

At the lowest blockage, $B=5\%$, the differences in peak u'/U_o , relative to $B=17\%$ and $B=8\%$, between the GSW, ASW, and SLW configurations are the smallest. This finding reflects the diminished blockage effects. Similar to $B=8\%$, the differences in formation lengths for $B=5\%$ between the wall configurations investigated are within experimental uncertainty. This suggests that wall adaptation has negligible effect on vortex formation length for $B \leq 8\%$. On the average, the formation length measured in each wall configuration for $B=5\%$ is $0.08d$ longer than that measured in the same wall configuration for $B=8\%$. This indicates that increasing blockage ratio tends to decrease formation length for a fixed aspect ratio ($L/d = 14$), supporting the fact that the increased velocity (and hence, increased Re_d) due to blockage effects tends to decrease the vortex formation length.

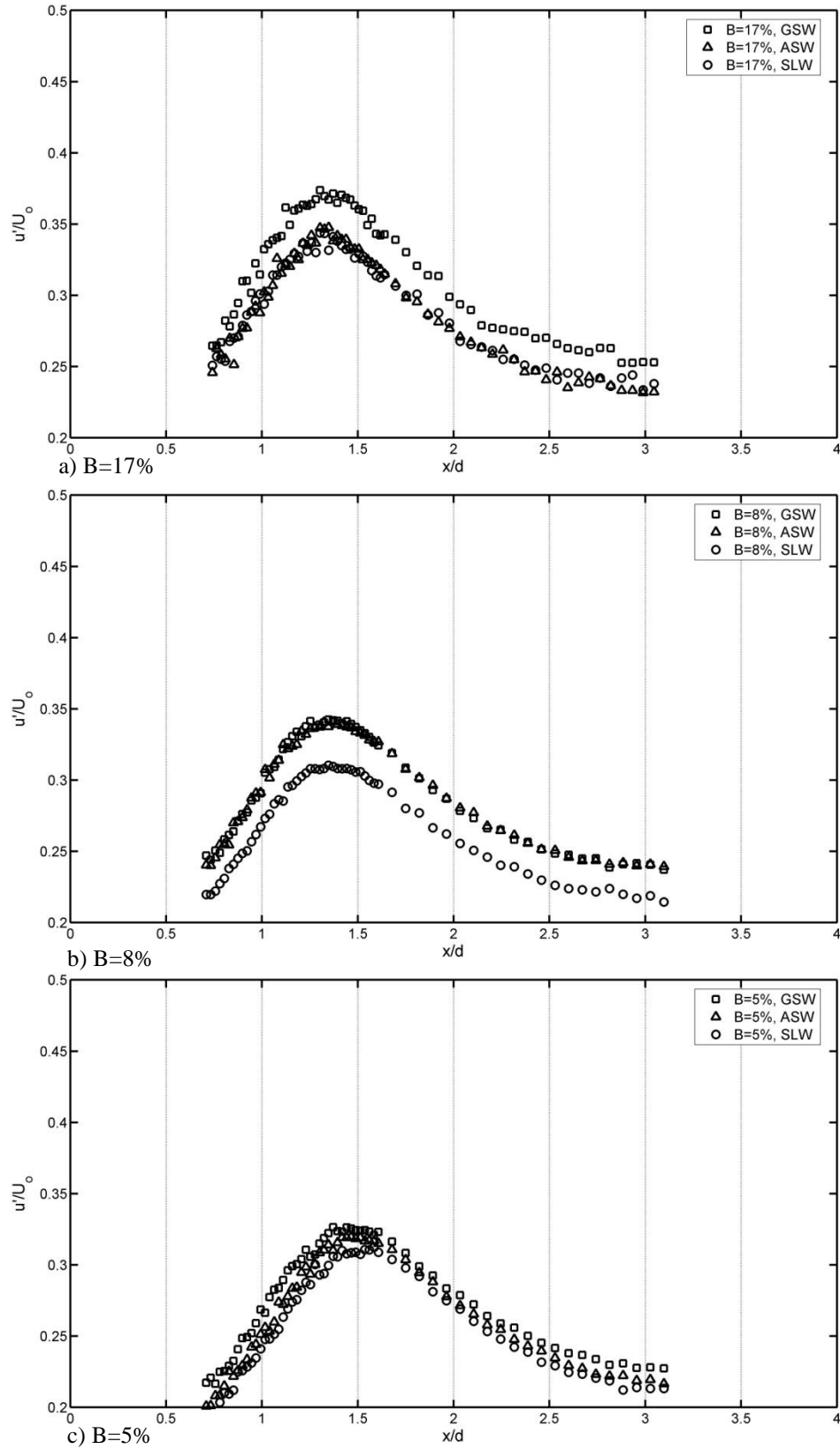


Figure 5.22 Evaluation of centerline streamwise RMS velocity with x/d in the GSW, ASW, and SLW configurations for a) B=17%, b) B=8%, and c) B=5%.

5.6 Wake Vortex Shedding Frequency

The goal of this section is to identify the effect of wall adaptation on wake vortex shedding frequency. Spectral analysis of instantaneous streamwise (u) and vertical (v) fluctuating velocity signals acquired with a cross-wire probe at $x/d = 2.5$ and $y/d = 0.5$ was employed to detect the wake vortex shedding frequency. The signal from the cross-wire probe was sampled for approximately seven minutes at a sampling rate of 5000 Hz. To aid in the accurate determination of the Strouhal number, the free-stream velocity was averaged over the duration of the seven minute sampling time. Based on 128 averages in the spectral analysis, the frequency resolution is 0.3 Hz.

Figures 5.23, 5.24, and 5.25 show spectra of streamwise (E_{uu}) and vertical (E_{vv}) velocity fluctuations for blockages of 17%, 8%, and 5%, respectively. For all the wall configurations, the velocity spectra display dominant peaks attributable to wake vortex shedding. In addition to the dominant peak centered at the shedding frequency (f_v), peaks centered at the first and second harmonics of the shedding frequency appear in the spectra. The frequencies associated with dominant peaks in the u -spectra compared to the v -spectra are within the frequency resolution of the spectral analysis. From Figs. 5.23-5.25, it is clear that peaks in the v -component spectra are more pronounced than the corresponding peaks in the u -component spectra. This is especially true for the first and second harmonic of the wake vortex shedding frequency.

For each blockage ratio investigated, the shedding frequency is the highest in the GSW configuration and is reduced in the ASW and SLW configurations. The deviation in the shedding frequency between wall configurations becomes more pronounced for higher

blockage ratios. Although small, a discernable difference in frequencies pertaining to different wall configurations is observed even at 5% blockage.

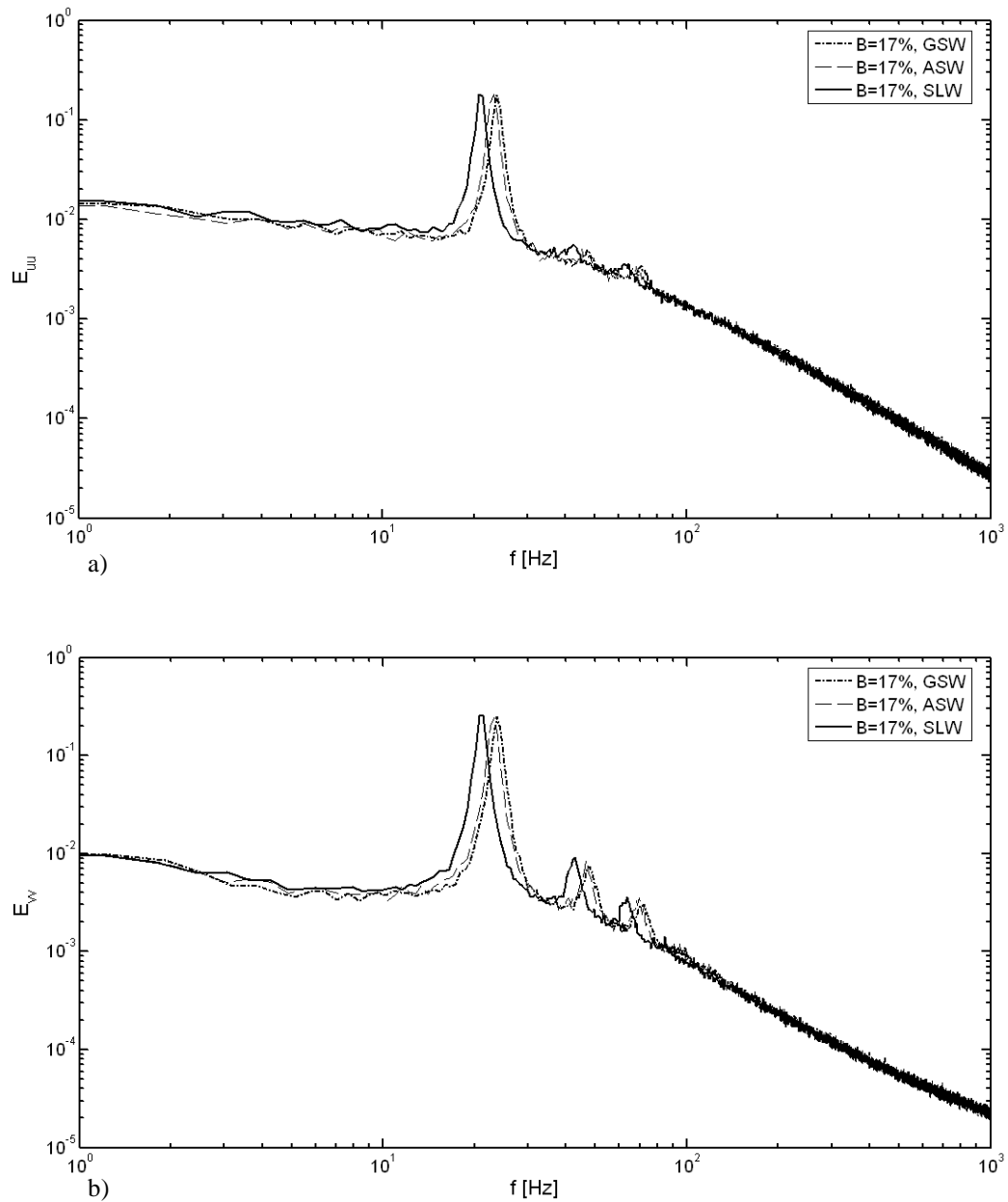


Figure 5.23 Velocity spectra for B=17% at $x/d=2.5$, $y/d=0.5$ based on a) streamwise fluctuating component and b) vertical fluctuating component.

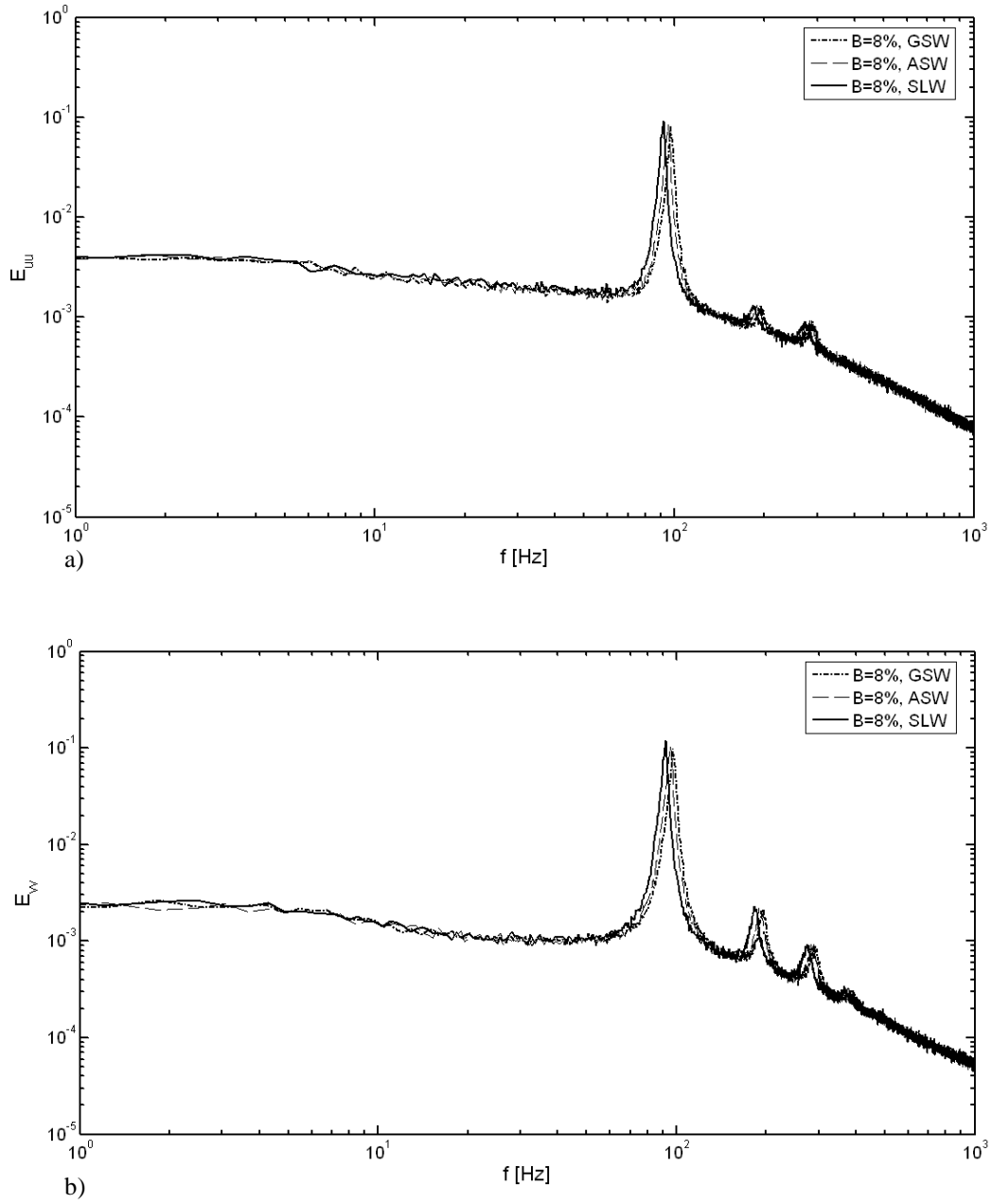


Figure 5.24 Velocity spectra for B=8% at $x/d=2.5$, $y/d=0.5$ based on a) streamwise fluctuating component and b) vertical fluctuating component.

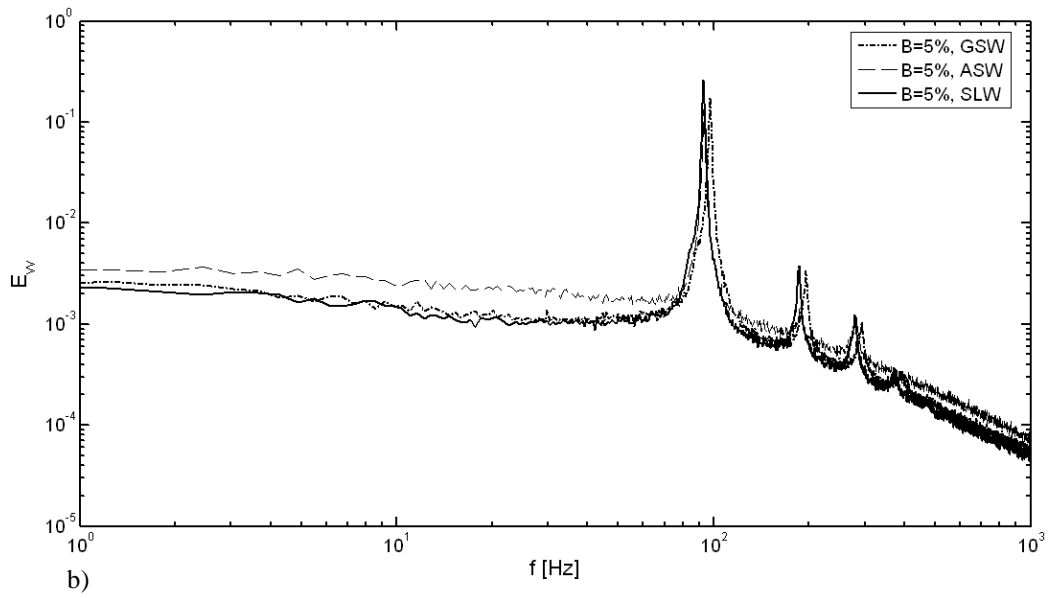
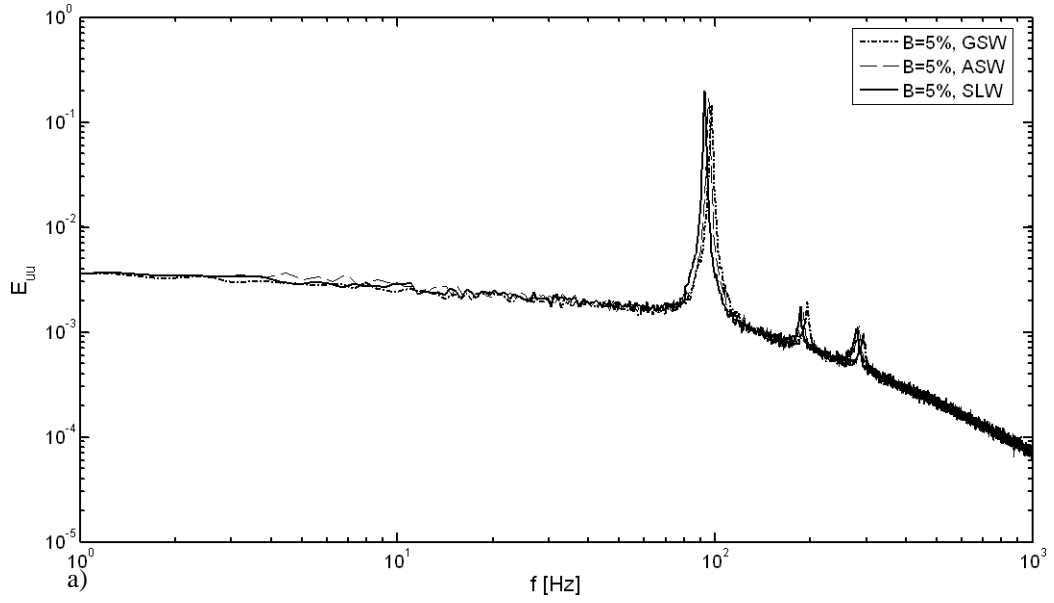


Figure 5.25 Velocity spectra for $B=5\%$ at $x/d=2.5$, $y/d=0.5$ based on a) streamwise fluctuating component and b) vertical fluctuating component.

Based on the spectra presented in Figs. 5.23-5.25, the corresponding Strouhal numbers are summarized in Table 5.6.

Table 5.6 Strouhal numbers for all wall configurations and blockage ratios investigated.

B [%]	GSW	ASW	SLW
17	0.22	0.21	0.19
8	0.21	0.20	0.19
5	0.20	0.20	0.19

Consistent with the experimental findings of Ramamurthy & Ng (1973) and Hiwada & Mabuchi (1981), the Strouhal number is found to increase with the blockage ratio when measured in the GSW configuration. The results show that the Strouhal number converged to 0.19 in the SLW configuration for all blockage ratios. Based on the compilation of results in Norberg (2003), the expected Strouhal number, for the current Re_d , should be in the range of $0.18 \leq St \leq 0.19$. Thus, it can be concluded that the adaptive-wall strategy adequately corrects Strouhal number at blockage ratios of up to and including 17%. It is interesting to note that, although the near wake width is observed to be invariant between the SLW and GSW configurations, the Strouhal number decreases in the SLW configuration relative to that in the GSW configuration. Thus, it is speculated that the mechanism responsible for the deviation of vortex shedding frequency is mainly due to the velocity change associated with solid blockage effects, i.e., a higher velocity around the model results in higher shedding frequencies. To explore this further, a new velocity scaling for the Strouhal number is investigated using the velocity outside of the wake at $x/d = 2.5$, where the data for the velocity spectra was obtained. The results are shown in Fig. 5.26 for all combinations of blockage ratios and wall configurations investigated. For reference, the values of the Strouhal number calculated using the traditional formulation of $St = f_v d / U_o$ are also shown in Fig.

5.26. Comparing the results, it can be seen that the new scaling results in Strouhal numbers collapsing to within 2.5% of the expected St value of 0.19, except for one outlier at $B=5\%$ in the ASW configuration. The error bars of 2.5% shown in Fig. 5.26 are associated with the uncertainty of the free-stream speed measurements. Thus, it can be concluded that indeed the main mechanism responsible for the increase of the Strouhal number in the GSW and ASW configurations is the increase of velocity around the cylinder due to solid blockage. By implementing the wall adaptation strategy, the effects of solid blockage are alleviated, and, thus, the value of St corresponds to that expected for low blockage ratios.

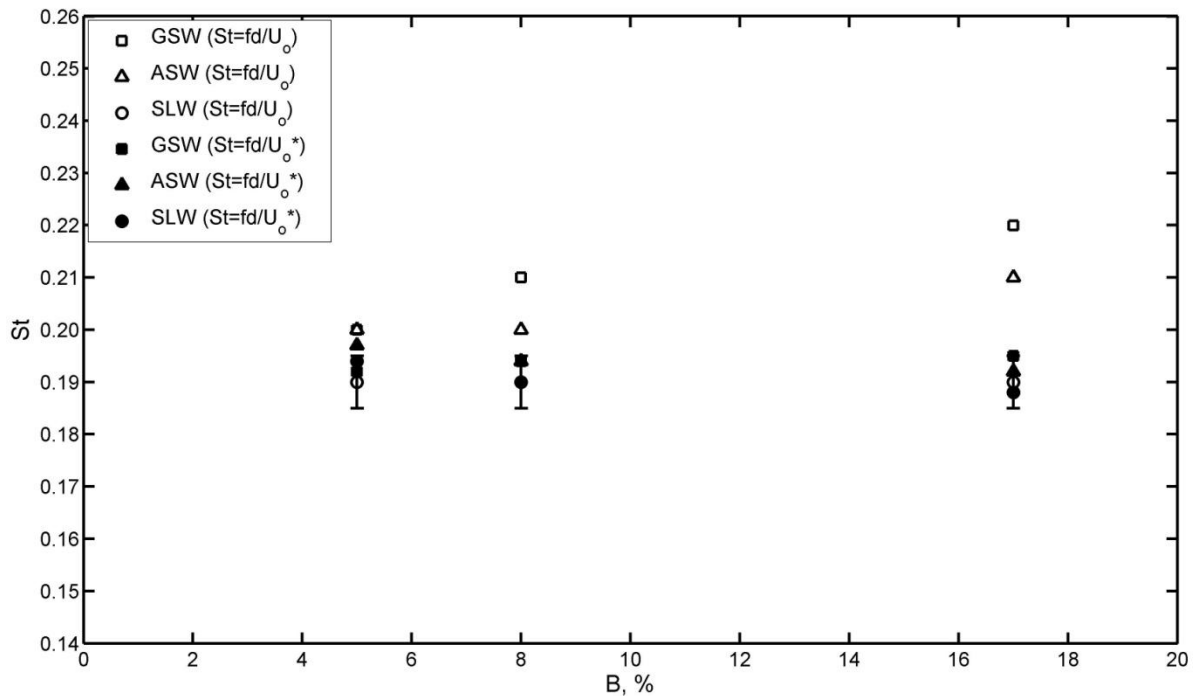


Figure 5.26 Strouhal number variation for all wall configurations and blockage ratios investigated.

To investigate a possible effect of the traversing mechanism on the measured wake vortex shedding frequency, spectral analysis of pressure fluctuations measured on the cylinder surface, with the traverse placed well downstream of the model, was performed. The signal from the pressure transducer positioned at the angle of $\theta=82^\circ$ was sampled for about 7

minutes at 5000 Hz. The obtained pressure spectrum in the SLW configuration for $B=17\%$ is shown in Fig. 5.27 along with the corresponding streamwise wake velocity spectrum obtained at $x/d = 2.5$, $y/d = 0.5$. The results show that the dominant peak in the pressure spectrum is centered at the same frequency as that in the wake velocity spectrum. In the GSW and ASW configurations, similar results were obtained, suggesting that the position of the traversing mechanism has negligible effect on the wake vortex shedding frequency.

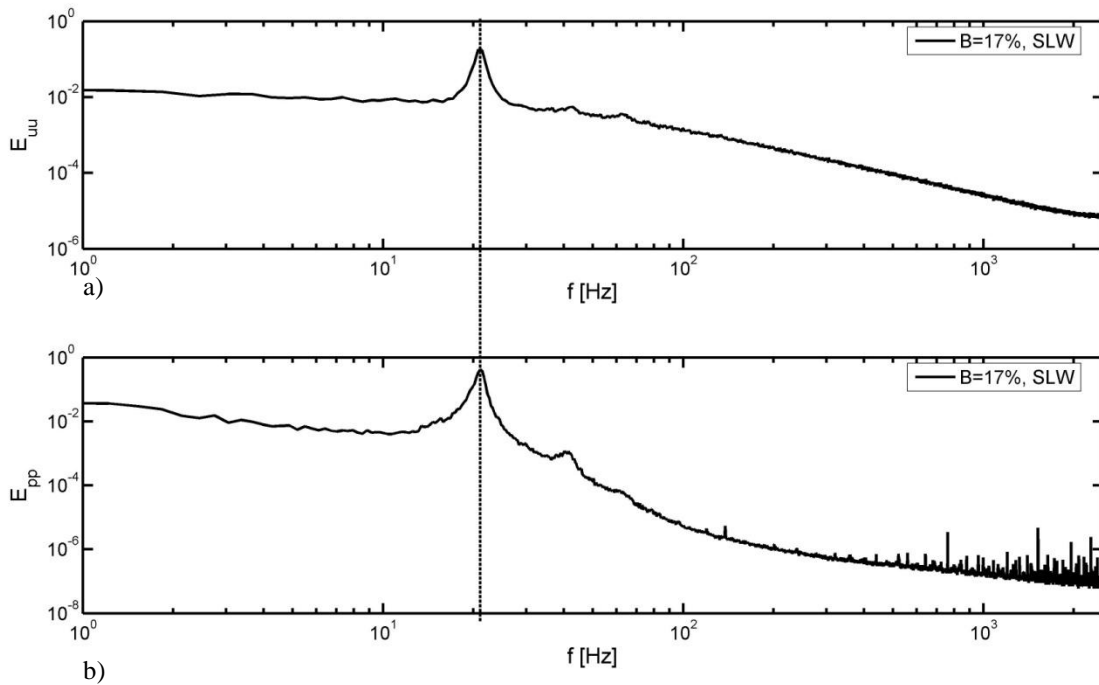


Figure 5.27 Comparison of a) velocity spectrum at $x/d=2.5$ and $y/d=0.5$ and b) pressure spectrum at $\theta=82^\circ$ in the SLW configuration for $B=17\%$.

5.7 Shear Layer Instability Frequency

The separated shear layer contains coherent structures, which have smaller time and length scales relative to those of the wake vortices (Bloor, 1964). The aim of this section is to identify the effect of wall adaptation on the frequency of these coherent structures. In literature, the frequency of shear layer structures is often referred to as ‘Bloor-Gerard frequency’, ‘Kelvin-Helmholtz frequency’, or ‘shear layer instability frequency’. The current study will use the term ‘shear layer instability frequency’, or ‘instability frequency’, denoted by f_{sl} .

Given the small length scales of the shear layer vortices, the spatial identification of these structures is not trivial (e.g., Rajagopalan & Antonia, 2005). To identify these structures, the hot-wire was traversed within the vortex formation region ($0 < x/d < 1.5$) and along the edge of the wake ($0.5 < y/d < 0.7$). Several velocity spectra of the streamwise fluctuating velocity component were acquired within the aforementioned flow region, until the shear layer instability frequency was identified. Due to the high frequency expected for the shear layer instability, the hot-wire signals were sampled at 10,000 Hz.

For each wall configuration, velocity spectra pertaining to $x/d = 0.25$ and $y/d = 0.62$ are shown in Figs. 5.28a, 5.28b, and 5.28c for blockages of 17%, 8%, and 5%, respectively. In addition to the dominant peak due to wake vortex shedding, two broad peaks appear in the velocity spectra. These two peaks are centered at frequencies significantly higher than the corresponding wake vortex shedding frequency, f_v (Fig. 5.28). These frequencies pertain to the shear layer instability frequency (f_{sl}) and its sub-harmonic ($0.5f_{sl}$), with the latter attributed to vortex pairing in the separated shear layer (e.g., Rajagopalan & Antonia, 2005; Ahmed & Wagner, 2003).

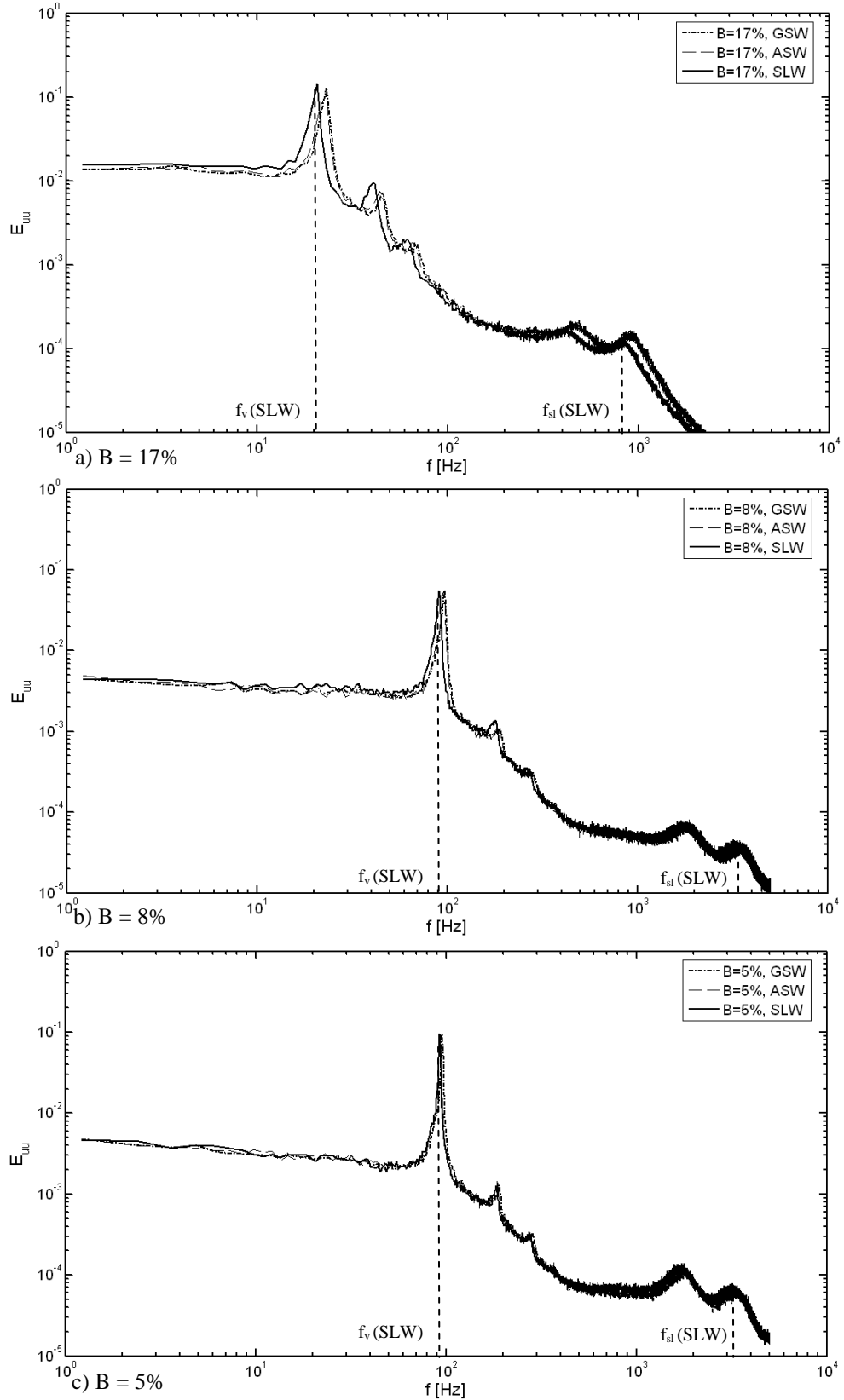


Figure 5.28 Velocity spectra obtained in the separated shear layer for the GSW, ASW, and SLW configurations at $x/d = 0.25$, $y/d = 0.62$.

Vortex pairing, as evident by the subharmonic ($0.5f_{sl}$) is the most common harmonic; however, the first harmonic ($2f_{sl}$) has been identified by some researchers (e.g., Rajagopalan & Antonia, 2005). The peak centered at the highest frequency is also confirmed as f_{sl} by using empirical correlations from research (e.g., Prasad & Williamson, 1997).

As shown in Fig. 5.28, the peaks associated with the primary instability frequency and its sub-harmonic frequencies are quite broad, relative to the peak associated with the wake vortex shedding frequency. To identify the central frequencies of the broad peaks, fourth order polynomial curves were fit to each peak. The frequency corresponding to the local maxima in each curve was deemed to be the instability frequency (f_{sl}), or the sub harmonic frequency ($0.5f_{sl}$). Consistent with data scaling employed by Bloor (1964), Norberg (1987), and Prasad & Williamson (1997), the shear layer instability frequency is normalized by the wake vortex shedding frequency (f_v). The instability frequency (f_{sl}) and normalized instability frequency (f_{sl} / f_v) for all the investigated combinations of wall configurations and blockage ratios are shown in Table 5.7. For each blockage ratio tested, the shear layer instability frequency is the largest in the GSW configuration, with the highest f_{sl} observed for the highest blockage tested ($B=17\%$). The results suggest that the shear layer instability frequency increases with blockage, similar to the discussed effect of blockage on vortex shedding frequency.

Table 5.7 Shear layer instability frequencies for all wall configurations and blockage ratios investigated.

B [%]	GSW			ASW			SLW		
	f_v	f_{sl}	f_{sl}/f_v	f_v	f_{sl}	f_{sl}/f_v	f_v	f_{sl}	f_{sl}/f_v
17	23	906	39	22	898	40	20.5	823	40
8	97	3541	37	95	3440	36	90.5	3260	36
5	95	3347	35	93	3173	34	92	3174	35

The normalized instability frequencies, summarized in Table 5.7, are also shown graphically in Fig. 5.29. The pioneering results of Bloor (1964) suggest that the normalized shear layer instability frequency is proportional to Re_d^n , where n is 0.5. Subsequent researchers have reported a wider range of exponents (n), namely, $0.5 \leq n \leq 0.87$ (Rajagopalan & Antonia, 2005). Prasad & Williamson (1997) conducted an investigation to classify the $f_{sl}/f_v - Re_d$ relationship over a wide range of Re_d ($1,200 < Re_d < 44,500$). By using data from their own experiments and data sets from other researchers, the following correlation was proposed, $f_{sl}/f_v = 0.0235 Re_d^{0.67}$. For a similar range of Reynolds numbers ($2,200 < Re_d < 44,500$) Norberg (1987) obtained the relationship of $f_{sl}/f_v = 0.0346 Re_d^{0.64}$. Based on the current Re_d , the f_{sl}/f_v values obtained using both the Norberg (1987) and Prasad & Williamson (1997) formulae are plotted in Fig. 5.29 for comparison.

As seen in Fig. 5.29, in a given wall configuration, f_{sl}/f_v increases with the blockage ratio. However, for a given blockage, streamlining the walls does not have a significant effect on f_{sl}/f_v , as the largest difference between wall configurations at a fixed blockage ratio is only 3.0%. It is interesting to note that, although both f_v and f_{sl} reduce when walls are streamlined, the ratio of f_{sl}/f_v remains relatively constant.

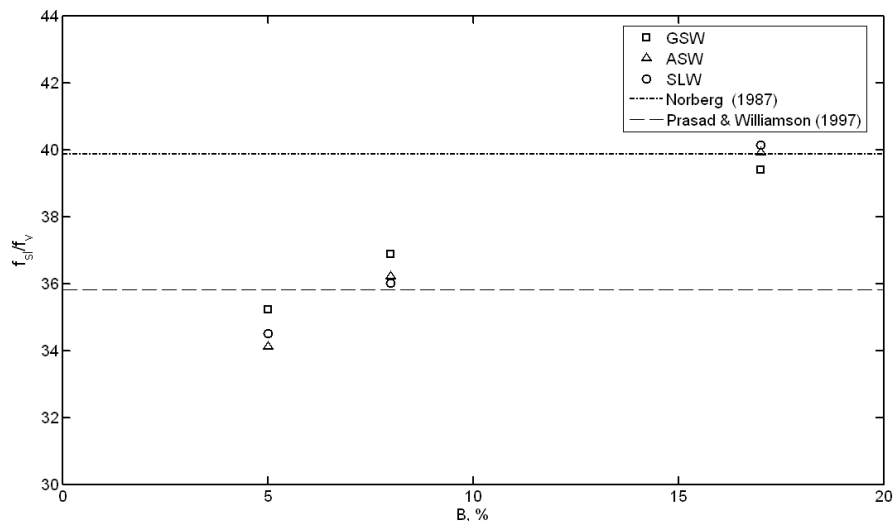


Figure 5.29 Normalized shear layer instability frequency for the GSW, ASW, and SLW configurations.

6 Conclusions

Successful research in fluid mechanics is based on the acquisition of high quality experimental data. The quality of such data depends on the adequacy of the experimental facility and the control of influencing parameters, which can adversely effect experimental results. The two main objectives of this research were to modernize the University of Waterloo Adaptive-Wall Wind Tunnel and to identify the effect of wall adaptation on flow development over a common engineering shape — the circular cylinder.

The quality of a wind tunnel testing facility depends on flow uniformity and free-stream turbulence intensity. Prior to the modifications detailed here, flow uniformity and free-stream turbulence intensity were measured to be 1.2% and 0.6%, respectively. Upon the installation of a new honeycomb and four screens, these values were measured to be less than 0.6% and 0.3%, respectively, surpassing the research objectives. In addition to settling chamber modifications, the wind tunnel was modernized with the design and installation of an automated three axis traverse and the implementation of automated electronic pressure scanner modules for the acquisition of wall surface pressures.

The second main objective of this thesis was to identify the effect of wall adaptation on the flow development over a circular cylinder as tested in an adaptive-wall wind tunnel. The predictive wall adjustment strategy of Wolf & Goodyer (1988) was incorporated into the control system of the wind tunnel. Tests were conducted in three wall configurations, namely, geometrically straight walls (GSW), aerodynamically straight walls (ASW), and streamlined walls (SLW). All tests were conducted at a Reynolds number (Re_d) of 57,000 for blockage ratios (B) of 5%, 8%, and 17%.

For all the blockage ratios investigated, the mean surface pressure distribution in the GSW configuration is highlighted by an increased suction peak and increased base suction, relative to those observed in the ASW and SLW configurations. The influence of blockage effects are the most pronounced for B=17%, as the pressure drag and the base suction coefficient are 17% and 24% higher than the expected values for low blockage ratios, respectively. Upon streamlining the walls, the adverse blockage effects in the pressure distributions are removed, with the distributions for B=5% and B=8% closely following those obtained in previous studies measured at low blockage ratios. It is speculated that the minor discrepancies observed between the pressure distributions for B=5% and B=8% with that for B=17% are caused by a variation in cylinder aspect ratio. Thus, it is concluded that wall adaptation successfully corrects cylinder pressure distributions up to and including B=17%.

Mean wake velocity measurements in the GSW configuration suggest that wake width growth is limited at 15 and 7.75 diameters downstream of the cylinder axis for blockages of 8% and 17%, respectively. Streamlining the walls corrects this limitation and allows the half wake width (b) to develop with streamwise distance (x) at the rate expected for low blockage ratios (i.e., $b \propto x^{0.5}$) for streamwise distances up to and including $x/d=19$. For B=5% blockage, wake width growth was uninhibited in both the GSW and SLW configurations.

In the very near wake ($x/d < 2.5$), wall adaptation has negligible effect on wake width growth. Similarly, RMS wake velocity profiles suggest that wall adaptation has no measurable effect on the vertical distance separating consecutive wake vortices shed from the top and bottom surfaces of the cylinder. Although these dimensions are known to be related to the

frequency of wake vortex shedding, the results suggest that wall adaptation has a substantial effect on vortex shedding frequency. Specifically, the vortex shedding frequency increases with the blockage ratio. For $B=17\%$, the Strouhal number of 0.22 observed in the GSW configuration is reduced to $St=0.21$ and $St=0.19$ in the ASW and SLW configurations, respectively. For all the cases investigated, streamlining the walls resulted in a Strouhal number falling within the range $0.18 \leq St \leq 0.19$ expected for low blockage ratios. The aforementioned invariance of the near wake half width development to blockage effects suggests that the mechanism responsible for the increase in vortex shedding frequency is likely due to the increased velocity caused by solid blockage effects. Indeed, normalizing the shedding frequency by the velocity measured outside of the wake, as opposed to the upstream free-stream velocity, results in the Strouhal numbers collapsing on $St \approx 0.19$ for all the cases investigated.

Similar to the vortex shedding frequency, the shear layer instability frequency is the highest in the GSW configuration, being slightly reduced in the ASW configuration, for $B=17\%$ and $B=8\%$. For $B=5\%$, the GSW configuration is again observed to have the highest value of f_{sl} , although the values measured in the ASW and SLW configuration are equivalent. It is interesting to note that although the shear layer instability frequency increases in the GSW configuration with blockage, the ratio of shear layer instability to vortex shedding frequency remains relatively constant for a given blockage ratio.

7 Recommendations

The two main objectives of this research have been accomplished, namely, i) modernization on the University of Waterloo Adaptive-Wall Wind Tunnel and ii) the identification of the effects of wall adaptation on flow development over a circular cylinder. This section provides recommendations to build on the foundation set by the successful completion of the outlined objectives.

Throughout the implementation and testing of the adaptive-wall strategy it is estimated that over 100 hours were spent in the manual movement required to set the flexible walls of the test section. If blockage studies continue to be a focus at the University of Waterloo, it is strongly recommended that wall movement be automated. A stepper motor system to control all 96 rack and pinions is estimated to cost about \$100,000.

The wind tunnel fan is powered from a DC generator whose AC input voltage is directly tied to the facility line voltage entering the lab. Thus, the voltage to the fan, and corresponding RPM of the fan, fluctuates with variation in the line voltage. Typically, this variation is minor, corresponding to a velocity deviation of less than $\pm 0.6\%$ from the set tunnel speed. However, the fan RPM has been occasionally observed to change abruptly, with the resulting deviation of up to 5% from the set tunnel speed. When this occurred in the present study, data collection was stopped and was restarted once the fan RPM stabilized. To avoid this downtime, it is highly recommended that the cause of the line voltage variation be identified and corrected and/or a control system be implemented with active feedback control to regulate the DC voltage to the wind tunnel fan.

To expand on the experimental findings for the effect of wall adaptation on flow development over a circular cylinder, it is recommended that the Reynolds number (Re_d) effect be investigated since blockage effects are a function of Re_d . Assuming the same blockage range is covered ($5\% < B < 17\%$), the achievable range of Reynolds number is $12,000 < Re_d < 110,000$, based on the attainable wind tunnel speeds of 2 to 40 m/s. These Reynolds numbers cover both the shear layer transition regime and the pre-critical regime, marking the beginning of the transition to turbulence in the boundary layer.

In addition to Re_d effects, flow visualization is recommended to obtain additional information on the effect of wall adaptation on flow development. The test section of the wind tunnel is ideal for smoke-wire visualization since one side of the rigid side walls is matte black, and the other is transparent. Flow visualization will provide insight into wake development and aid in the determination of vortex shedding characteristics.

References

- Ahmed, N.A., and Wagner, D.J. (2003) "Vortex Shedding and Transition Frequencies Associated with Flow Around Circular Cylinder," AIAA Journal, Vol.41, pp. 542-544.
- Allen, H.J., and Vincenti, W.G. (1948). "Wall Interference in a Two-Dimensional-Flow Wind Tunnel, with Consideration of the Effect of Compressibility," Nat. Adv. Committee Aero., NACA Tech. Rep. 782. Vol. 23.
- Bearman, P.W. (1965). "Investigation of the Flow Behind a Two-Dimensional Model with a Blunt Trailing Edge and Fitted with Splitter Plates," Journal of Fluid Mechanics, Vol. 21, pp. 241.
- Bishop, M., Gerakopulos, R., and Yarusevych, S. (2009) "Effect of Wall Adaptation on Flow Development over a Circular Cylinder," 39th AIAA Fluid Dynamics Conference, June 22-26, San Antonio, Texas.
- Bloor, M.S. (1964) "The Transition to Turbulence in the Wake of a Circular Cylinder," Journal of Fluid Mechanics, Vol.19, pp. 290-304.
- Bottin, B., Carbonaro, M., and Schroder, W. (1997) "First Runs of the Adaptive Wind Tunnel T'3 at VKI: Calibration and Application of a Flexible Wall Adaptation Technique on a NACA0012 Airfoil," 4th Belgian Congress on Theoretical and Applied Mechanics, May 22-23, Leuven, Belgium.
- Bradshaw, P., and Mehta, R. (2003) "Wind Tunnel Design" <http://www.htglstanford.edu/bradshaw/tunnel/wadiffuser.html>
- Brundrett, E., and Kankainen, P. (1991) "The Construction and Passive Wall Testing of the U of W 610 by 910mm Flexible Walled Wind Tunnel," Department of Mechanical Engineering, University of Waterloo Technical Report, FWWT 91-1.
- Brundrett, E., and Kankainen, P. (1991) "The Construction and Commissioning of a Flexible Walled Wind Tunnel," Canadian Aeronautics and Space Journal, Vol. 37, No. 3, pp. 108-119.
- Chue, S.H. (1975) "Pressure Probes for Fluid Measurements," Prog. Aerospace Sci., Vol. 16, pp. 147-223.
- Corrsin, S. (1963) "Turbulence: Experimental Methods. Handbook of Physics," Springer, Vol. 8, Part 2, pp. 524-590.
- Dryden, H.L., and Schubauer, G.B. (1947) "The Use of Damping Screens for the Reduction of Wind Tunnel Turbulence," Journal of Aeronautical Sciences, Vol. 14, pp. 221-228.

- Everhart, J.L. (1983) "A Method for Modifying Two-Dimensional Adaptive Wind Tunnel Walls Including Analytical and Experimental Verification," NASA TP-2081
- Ewald, B.F.R. (1998) "Wind Tunnel Wall Correction," Advisory Group for Aerospace Research and Development, France, AGARD 336.
- Fage, A. (1929) "On the Two-Dimensional Flow Past a Body of Symmetrical Cross-Section Mounted in a Channel of Finite Breadth," Brit. Aero. Res. Council, Rep. and Memo. Vol. 23, pp. 1223.
- Gerakopoulos, R. (2008) "Wind Tunnel Traversing Mechanism Integration and Flow Quality Assessment," University of Waterloo ME 482 report.
- Goodyer, M.J., and Saquib, M. (2007) "Blockage Limits in a Two-Dimensional Self-Streamlining Wind Tunnel," 25th AIAA Applied Aerodynamics Conference, June 25-28, Miami, Florida.
- Groth, J., and Johansson, A. (1988) "Turbulence Reduction by Screens," Journal of Fluid Mechanics, Vol. 197, pp. 139-155.
- Hiwada, M., and Mabuchi, I. (1981) "Flow Behavior and Heat Transfer Around the Circular Cylinder at High Blockage Ratios," Heat Transfer Jap. Res., Vol. 10, pp.17-39.
- Judd, M. et al. (1981) "Application of the Computer for On-site Definition and Control of Wind Tunnel Shape for Minimum Boundary Interference," AGARD CP-210, Paper 6, N77-11975.
- Kankainen, P., Brundrett, E., and Kaiser, J.A. (1994) "A Small Wind Tunnel Significantly Improved by a Multi-Purpose, Two-Flexible-Wall Test Section," Journal of Fluids Engineering, Vol. 116, pp. 419-423.
- Kawall, J.G., Shokr, M., and Keffer, J.F. (1983) "A Digital Technique for the Simultaneous Measurements of Streamwise and Lateral Velocities in Turbulent Flows," Journal of Fluid Mechanics, Vol. 133, pp. 83-112.
- Laws, E.M., and Livesey, J.L. (1978) "Flow Through Screens," Ann. Rev. Fluid Mech. Vol. 10, pp. 247-266.
- Lim, H., and Lee, S. (2004) "Flow Control of a Circular Cylinder with O-Rings," Fluid Dynamics Research, Vol. 35, pp. 107-122.
- Linke, W. (1931) "New Measurements on Aerodynamics of Cylinders Particularly their Friction Resistance," Physikalische Zeitschrift, Vol. 32, pp. 900-914.
- Maskell, E.C. (1963) "A Theory of the Blockage Effects on Bluff Bodies and Stalled Wings in a Closed Wind Tunnel," Roy. Aircraft Establ., Farnborough, RAE Rep. 2685.

- Mehta, R.D., and Bradshaw, P. (1979) "Design Rules for Small Low Speed Wind Tunnels," *Aeronautical Journal*, pp. 443-449.
- Meyer, O., and Nitsche, W. (2004) "Update on Progress in Adaptive Wind Tunnel Wall Technology," *Progress in Aerospace Sciences*, Vol. 40, pp. 119-141.
- Modi, V.J., and El-Sherbiny, S.E. (1971) "Effect of Wall Confinement on Aerodynamics of Stationary Circular Cylinders," *Proc. 3rd Inst. Conf. Wind Effects on Buildings and Structures*, Tokyo, Vol. 23, pp. 365-375.
- Moffat, R.J. (1988) "Describing the Uncertainties in Experimental Results," *Experimental Thermal and Fluid Science Journal*, Vol. 1, pp. 3-17.
- Norberg, C. (1987) "Effect of Reynolds Number and a Low-Intensity Freestream Turbulence on the Flow Around a Circular Cylinder," *Dept. Applied Thermodynamics and Fluid Mechanics*, Chalmers University of Technology.
- Norberg, C. (1994) "An Experimental Investigation of the Flow Around a Circular Cylinder: Influence of Aspect Ratio," *Journal of Fluid Mechanics*, Vol. 258, pp. 287-316.
- Norberg, C. (2003) "Fluctuating Lift on a Circular Cylinder: Review and New Measurements," *Journal of Fluids and Structures*, Vol. 17, pp. 57-96.
- Okamoto, T., and Takeuchi, M. (1975) "Effect of Side Walls of Wind Tunnel on Flow Around Two-Dimensional Circular Cylinder and its Wake," *Bull. JSME*, Vol. 18, pp. 1011-1017.
- Ong, L., and Wallace, J. (1996) "The velocity field of the turbulent very near wake of a circular cylinder," *Experiments in Fluids*, Vol. 20, pp. 443-453.
- Pope, A. (1966) "Low-Speed Wind Tunnel Testing," John Wiley and Sons, New York.
- Prandtl, L. (1933) "Attaining a Steady Air Stream in Wind Tunnels," *NACA TM 726*.
- Prasad, A., and Williamson, C.H.K. (1997) "The Instability of the Shear Layer Separating from a Bluff Body," *Journal of Fluid Mechanics*, Vol. 333, pp. 375-402.
- Ramamurthy, A.S., and Ng, C.P. (1973) "Effect of Blockage on Steady Force Coefficients," *ASCE Journal Engg Mech. Div.* Vol. 99, pp.1050-1051.
- Rajagopalan, S., and Antonia, R.A. (2005) "Flow Around a Circular Cylinder – Structure of the Near Wake Shear Layer," *Experiments in Fluids*, Vol. 38, pp. 393-402.
- Roshko, A., and Fiszdon, W. (1969) "On the persistence of transition in the near wake, *Problems of Hydrodynamics and Continuum Mechanics*," Soc. Industrial and Appl. Math., Philadelphia, pp.606-616.

- Roshko, A. (1993) "Perspectives of Bluff Body Aerodynamics," *Journal of Wind Engineering and Industrial Aerodynamics*, Vol. 49, pp.79-100.
- Russo, G.P, Zuppari, G., and Basciani, M. (1995) "An experimental comparison of two adaptation strategies in an adaptive-walls wind tunnel," *Experiments in Fluids*, Vol. 19 pp. 274-279.
- Schlichting, H. (1930) "On the Plane Wake Problem," (Publication in German), *Ingenieur Archiv*, Vol. 1, pp. 533-571.
- Scheiman., J., and Brooks, J.D. (1981) "A Comparison of Experimental and Theoretical Turbulence Reduction from Screens and Honeycomb-Screen Combinations," *Journal of Aircraft*, Vol. 18, pp. 638-643.
- Sumner, D. (1994) "An Experimental Investigation of 3-D Models in a 2-D Adaptive Wall Test Section," University of Waterloo MASC Thesis.
- Sumner, D., and Brundrett, E. (1995) "Testing Three-Dimensional Bluff-Body Models in a Low-Speed Two-Dimensional Adaptive Wall Test Section," *Transactions of the ASME*, Vol. 117, pp. 546-551.
- Tan-Atichat, J., and Najib, H.M. (1982) "Interaction of Free-Stream Turbulence with Screens and Grids: A Balance Between Turbulence Scales," *Journal of Fluid Mechanics*, Vol. 114, pp. 501-528.
- Tavoularis, Stavros. (2005) "Measurement in Fluid Mechanics," Cambridge University Press.
- Thomson, K.B., and Morrison, D.F. (1971) "The Spacing, Positioning, and Strength of Vortices in the wake of Slender Cylindrical Bodies at Large Incidence," *Journal of Fluid Mechanics*, Vol. 50, pp. 751-783.
- West, G.S., and Apelt, C.J. (1982) "The Effects of Tunnel Blockage and Aspect Ratio on the Mean Flow past a Circular Cylinder with Reynolds numbers between 10^4 and 10^5 ," *Journal of Fluid Mechanics*, Vol. 114, pp. 361-377
- White, F. (2008) "Fluid Mechanics," Sixth Edition, McGraw Hill Higher Education, New York.
- Wiegardt. (1953). "On the Resistance of Screens," *Aero. Quarterly*, Royal Aero. Society., Vol. 4.
- Williamson, C.H.K. (1996) "Vortex Dynamics in the Cylinder Wake," *Annual Rev. Fluid. Mech.*, Vol. 28, pp. 477-539.

Wolf, S.W.D., and Goodyer, M.J. (1988) "Predictive Wall Adjustment Strategy for Two-Dimensional Flexible Walled Adaptive Wind Tunnel – A Detailed Description of the First One-Step Method," NASA CR 181635.

Wolf, S.W.D. (1995) "Adaptive Wall Technology for Improved Wind Tunnel Testing Techniques – A Review," Prog. Aerospace. Sci., Vol. 31, pp. 85-136.

Yarusevych, S., Sullivan, P.E., and Kawall, J.G. (2008) "Smoke-wire Flow Visualization on an Airfoil at Low Reynolds Numbers," 38th AIAA Fluid Dynamics Conference and Exhibit, June 23-26, Seattle, Washington, USA.

Zdravkovich, M.M. (1997a) "Flow Around Circular Cylinders, Vol 1: Fundamentals," Oxford University Press, Vol.1.

Zdravkovich, M.M. (2003) "Flow Around Circular Cylinders, Vol 2: Applications," Oxford University Press, Vol.2.

Appendix A: Settling Chamber Modifications

Original Settling Chamber

Figure A.1 shows the layout and spacing of the turbulence manipulating devices in the original settling chamber in the University of Waterloo Adaptive-Wall Wind Tunnel.

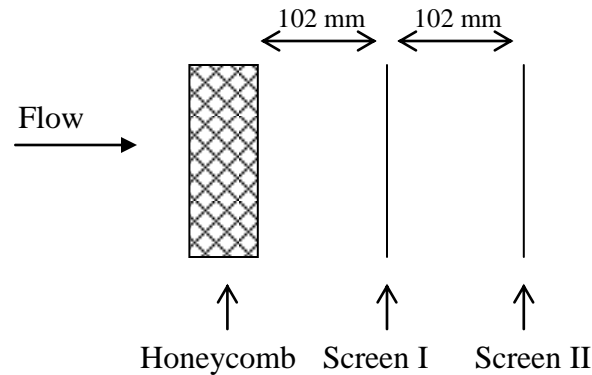


Figure A.1 Original settling chamber.

The honeycomb was comprised of corrugated fiberglass sheets, forming a hydraulic diameter of 42 mm and a length of 205 mm. The corresponding length to diameter ratio of 4.9 is outside the recommended range of 6-8 proposed by Mehta & Bradshaw (1979). The characteristics of the installed screens in the original settling chamber are summarized in Tab. A.1. The pressure drop coefficient (K) was calculated using the empirical correlation developed by Wieghardt (1953), assuming a free-stream test section velocity (U_o) of 15 m/s.

Table A.1 Characteristics of screens in original settling chamber.

Screen	M (openings per lineal inch)	Wire diameter [in]	Wire diameter [mm]	Mesh spacing [in]	Mesh spacing [mm]	β [%]	K
I	8	0.025	0.635	0.100	2.54	0.56	1.86
II	16	0.014	0.356	0.048	1.23	0.60	1.82

With a normal hot-wire placed in the midspan of an empty test section, the free-stream turbulence intensity was measured to be 0.6% at $U_o=15$ m/s. Also, in an empty test section, the vertical free-stream velocity profile was measured and the result is shown in Fig. A.2. Based on these results, flow uniformity was calculated to be $\pm 1.2\%$.

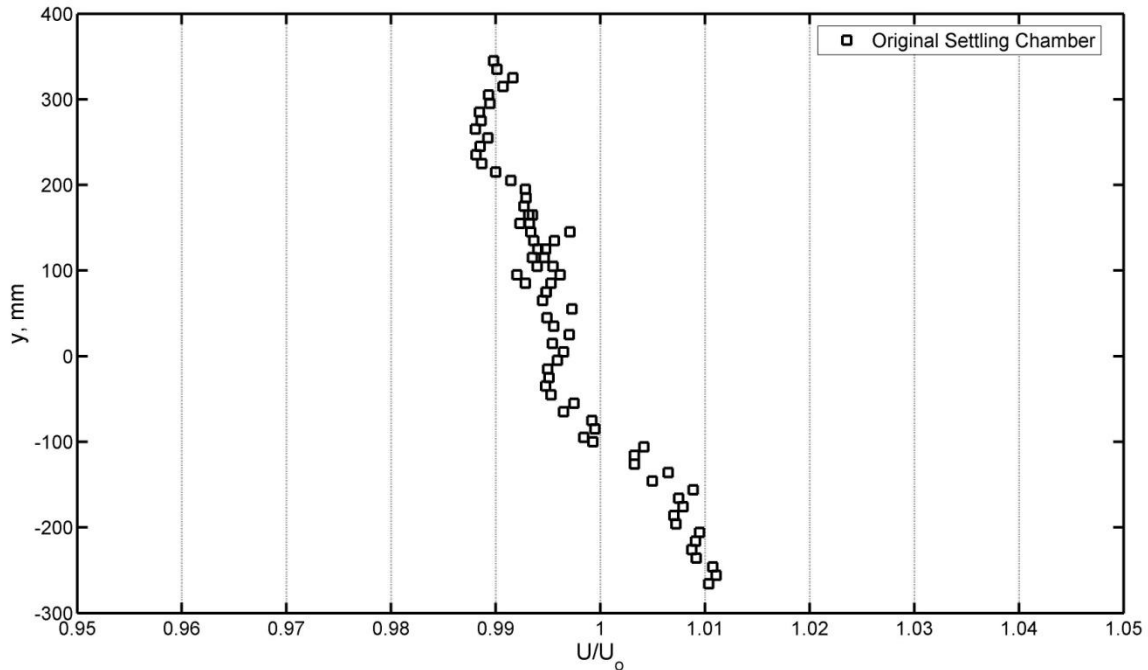


Figure A.2 Free-stream vertical velocity profile in the original settling chamber at $U_o=15$ m/s.

New Settling Chamber

The original honeycomb, screens, and supporting frames were carefully disassembled from the settling chamber. The primary concerns of the original settling chamber were a large hydraulic diameter (42mm) and small length to diameter ratio (4.9). Based on the design recommendations of Mehta & Bradshaw (1979) a new honeycomb was selected. The selected material was aircraft grade aluminum hexagonal honeycomb with a hydraulic diameter of 12.7mm and a length to diameter ratio of 8. A single sheet of honeycomb that could cover the entire settling chamber area (1.91m x 2.97m) could not be sourced; thus,

three 1.2m x 2.4m (4' x 8') were interlaced together. The honeycomb sheets were mounted in a welded aluminum frame.

Based on the objective to achieve a free-stream turbulence intensity of less than 0.5%, new screens had to be selected and installed. The original settling chamber consisted of three wooden frames on each of which a screen could be mounted. Although the original settling chamber had three wooden frames, only two screens were installed. New screens were selected in order to achieve $T_u < 0.5\%$. The pressure drop coefficient (K) for each proposed screen was calculated using Wieghardt's (1953) correlation, and the subsequent turbulence reduction factor was calculated using Prandtl's (1933) correlation. A constraint of screen selection was to have a screen open area ratio (β) of more than 0.58 (Mehta & Bradshaw, 1979). It was calculated that a combination of three screens was sufficient to achieve the desired turbulence reduction. The layout and spacing of turbulence manipulating devices in the new settling chamber are shown in Fig. A.3. The characteristics of the selected screens are shown in Table A.2.

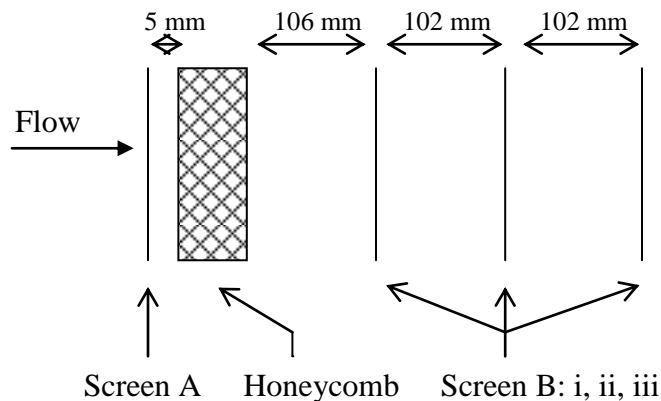


Figure A.3 New settling chamber.

Table A.2 Characteristics of screens in new settling chamber.

Screen	M (openings per lineal inch)	Wire diameter [in]	Wire diameter [mm]	Mesh spacing [in]	Mesh spacing [mm]	β [%]	Re_d (15m/s)	K
A	30	0.0065	0.1651	0.0268	0.68072	0.648	17.3	1.82
B	28	0.0075	0.1905	0.0282	0.71628	0.624	19.9	1.98

Based on the free-stream velocities utilized in this study and the screen wire diameters in Table A.2, the Reynolds number (Re_{dw}) is below the critical value of 40. Due to this fact turbulence is not generated in excess of the upstream flow therefore screen spacing is not critical. However, at the maximum free-stream velocity of 40 m/s achievable in the nominal test section, Re_{dw} is equal to 53 for screen B. The turbulence generated downstream of screen B at this velocity decays below the upstream turbulence intensity at a distance below 50cm (Groth & Johansson, 1988). This length of turbulence is much smaller than the screen spacing of 102mm as shown in Table A.2.

One screen was installed upstream of the honeycomb to serve as a filter for dirt entering the wind tunnel. To enable cleaning, the settling chamber incorporates removable access plugs located between screens. The access plugs are made from expanded polystyrene foam and are designed to be slightly compressed within the access slots to ensure a tight seal. Since the width of the settling chamber inlet was larger than the widest screen available, screens inevitably had to be stitched together. Utmost care was taken to achieve a high quality stitch so as to ensure a tight seam, while minimizing flow intrusion. The stitch was completed using Kevlar fishing line, chosen for its high strength and small diameter. To the same effect, three sheets of honeycomb had to be interlaced and installed in order to cover the area of the inlet.

Following settling chamber modifications, the free-stream turbulence intensity was measured to be less than 0.3% at a free-stream speed of $U_0=15$ m/s. The free-stream velocity profile measured with the settling chamber installed is shown in Fig. A.4. Based on these results, flow uniformity was calculated to be $\pm 0.6\%$. The new values for free-stream turbulence intensity and flow uniformity satisfied and exceeded the design objectives listed above.

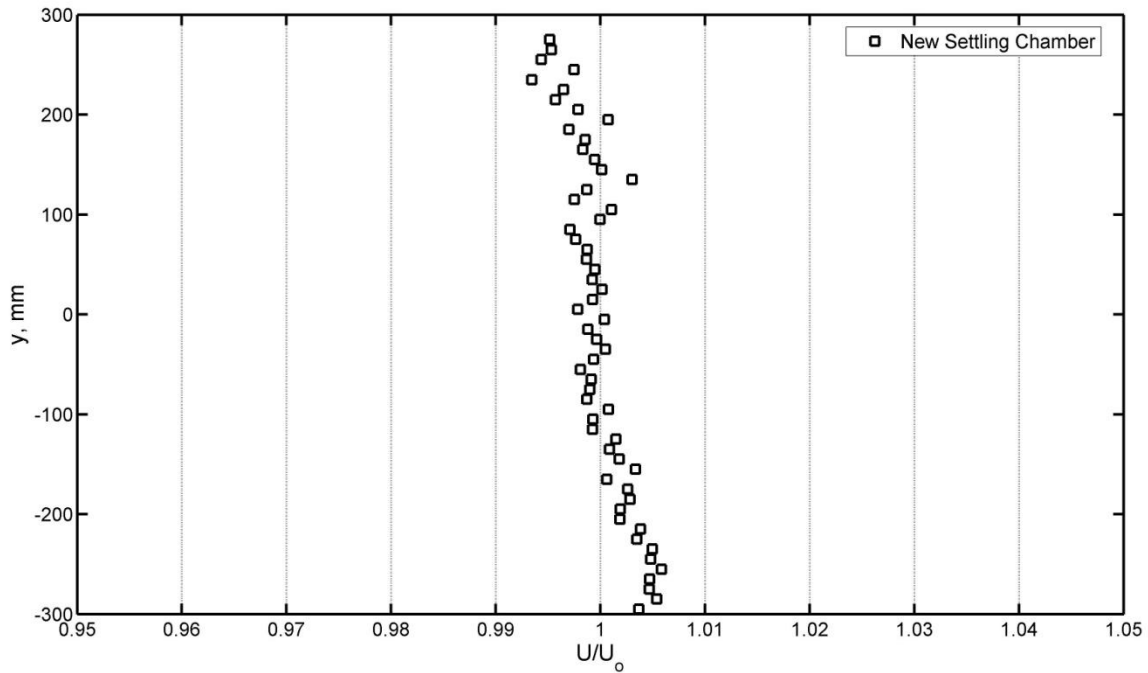


Figure A.4 Free-stream vertical velocity profile in the new settling chamber at $U_0=15$ m/s.

Appendix B: Measurement and Automation

Hot-wire Calibration

The normal and cross-wire probes were calibrated against a pitot-static tube in an empty test section, or well outside of the cylinder wake. The free-stream speed was set to nine different values and the corresponding mean voltages were computed based on the hot-wire anemometer signals. The anemometer voltage was related to the free-stream speed (U) by using a 4th order least squares polynomial fit (Eq. B.1):

$$U = \sum_{i=1}^4 a_i E^i \quad (\text{B.1})$$

Typical calibration curves for the normal and cross-wire probes are shown in Figs. B.1 a-c. The normal probe measures streamwise velocity (U), which can be directly determined by using a calibration curve such as the one shown in Fig. B.1a. In contrast, to obtain streamwise and vertical velocity components from the cross-wire probe, a second mathematical step must be completed. From Kawall et al., (1983), the effective velocities (U_{E1} and U_{E2}) can be converted to U and V using Eqs. B.2 and B.3, respectively.

$$U = \frac{U_{E1} + U_{E2}}{2} \quad (\text{B.2})$$

$$V = \frac{U_{E1} - U_{E2}}{2} \quad (\text{B.3})$$

A new calibration was completed anytime the streamwise velocities measured by the hot-wire probes deviated by more than 2% from the velocity measured by the pitot-static tube. Due to frequent temperature fluctuations in the lab, a typical calibration lasted 2 to 3 days.

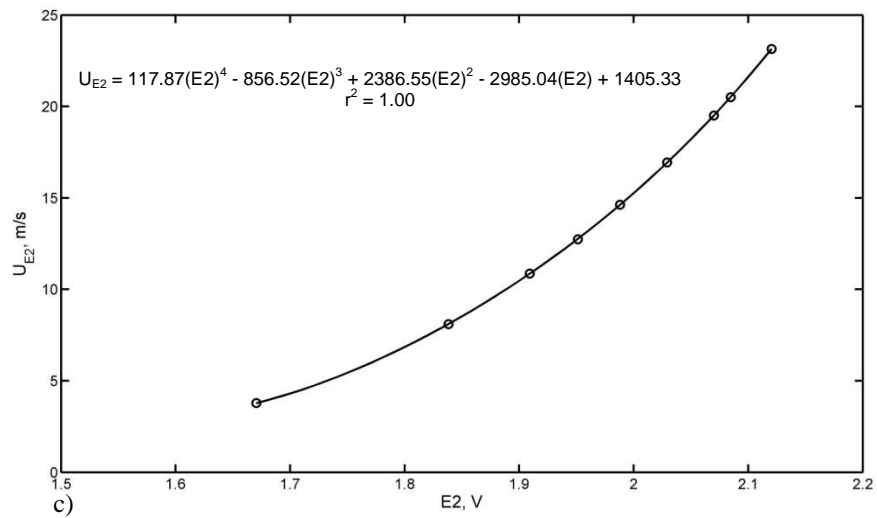
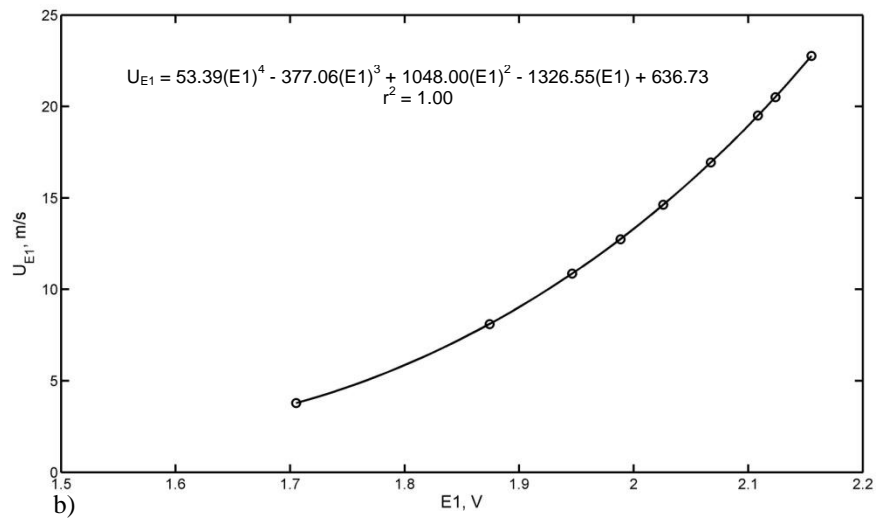
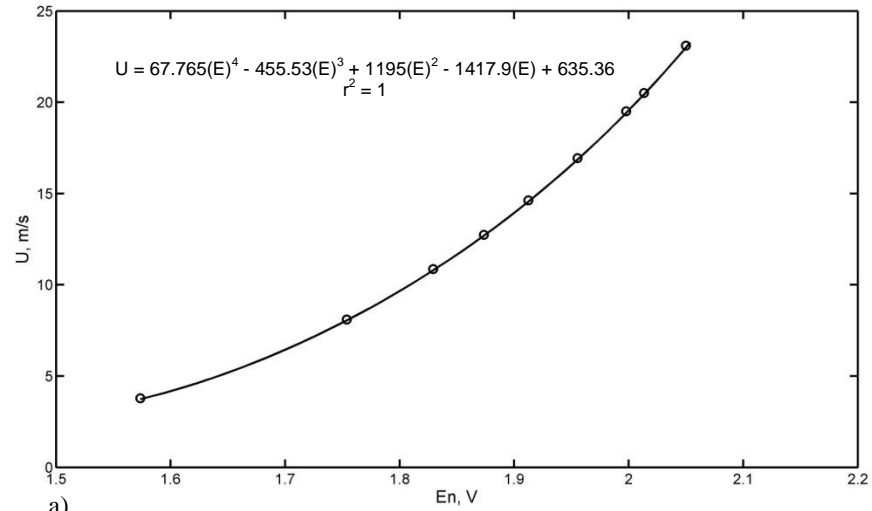


Figure B.1 Typical hot-wire calibration curves for a) normal probe (U vs E), b) cross-wire probe (UE1 vs E1), and c) cross-wire probe (UE2 vs E2).

Free-stream velocity was set by measuring the pressure drop across the fixed contraction (9.55 ratio) of the wind tunnel. The dynamic pressure ($0.5\rho U_o^2$) measured using the pitot-static tube placed at the model location in an empty test section was related to the contraction pressure drop through the calibration curves shown in Fig. B.2a and Fig. B.2b for the nominal and contracted test sections, respectively. These calibration curves can be used to compute the free-stream velocity (U_o) corresponding to a given dynamic pressure.

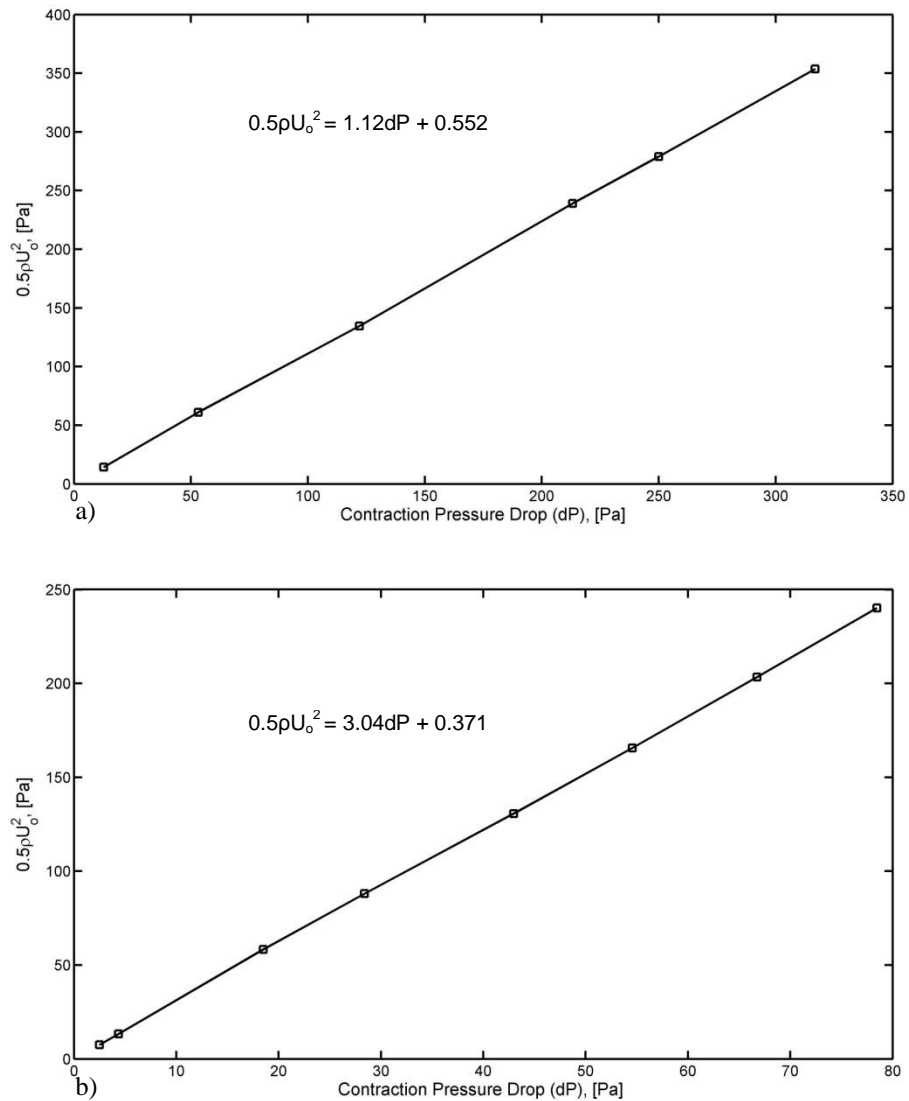


Figure B.2 Free-stream velocity calibration curves in the a) nominal and b) contracted test sections.

Electrical Drawings

Drawings for the electrical hardware required for the traverse automation and wall pressure measurements are included in this section. Figure B.3 shows both the data acquisition cards (PCI-6024E and PCI-6259) and the electrical equipment controlled by them. The motion of the three-axis traverse mechanism was controlled by the PCI-6024E card and driven by the stepper motor drives (GECKO G210) shown in Fig. B.4. An electrical box, i.e., “Black Box”, shown in Fig. B.5, was built to house hardware required for wall pressure measurements. Specifically, the box contained the solid state relay (SSR) board (Fig. B.6), required for ZOC33 operation mode selection, and the CMOS to TTL board required for ZOC33 binary addressing.

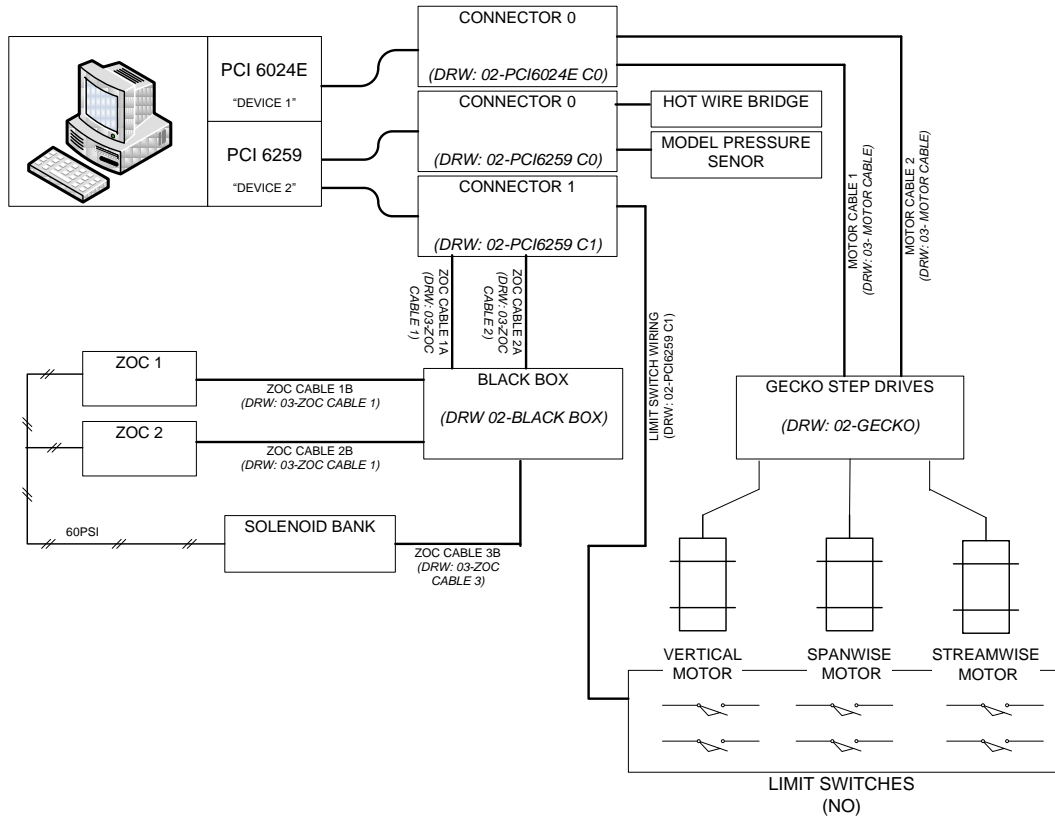
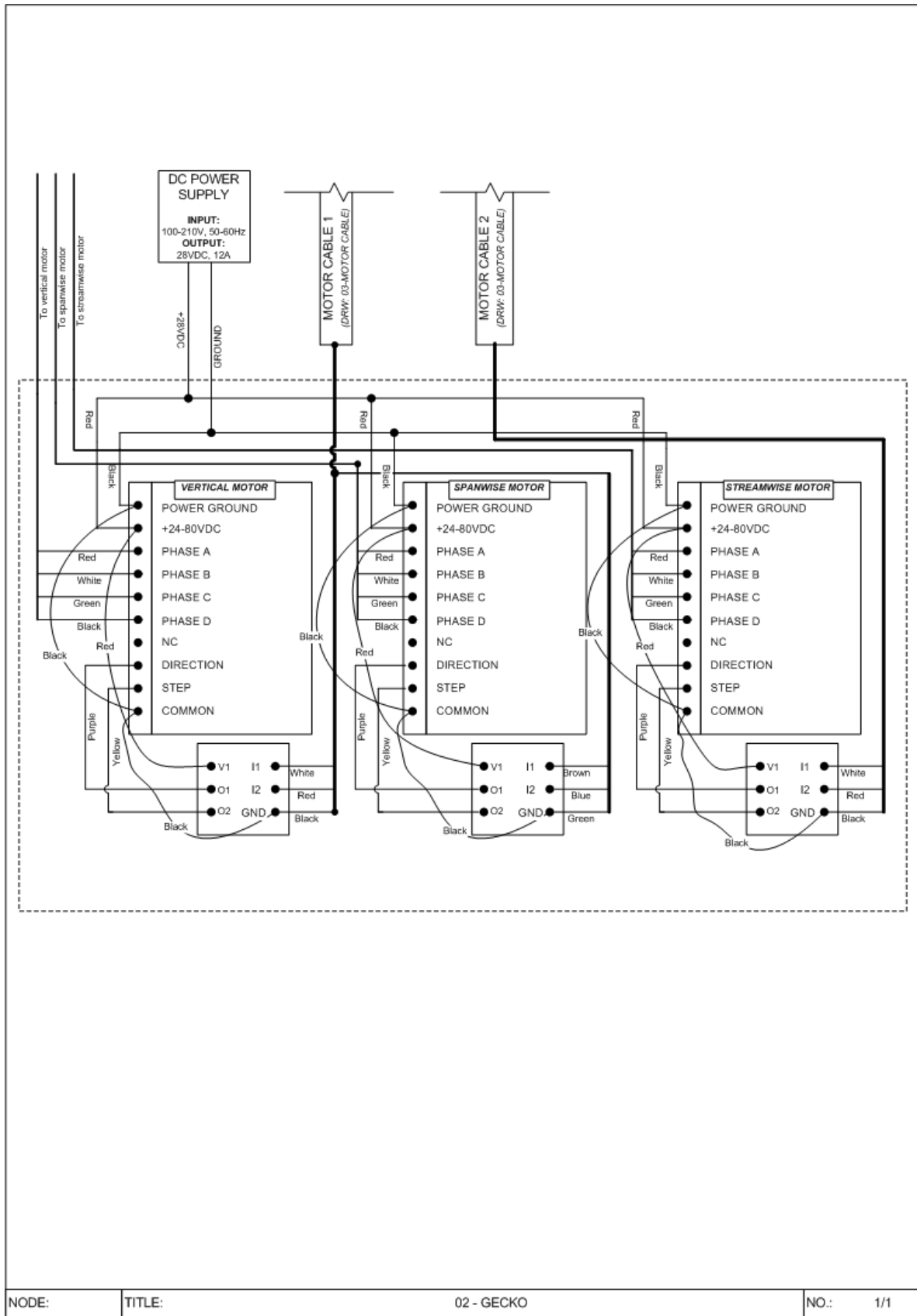


Figure B.3 Drawing summary for wind tunnel control system.



NODE:	TITLE:	02 - GECKO	NO.: 1/1
-------	--------	------------	----------

Figure B.4 Stepper motor drives for three-axis traverse.

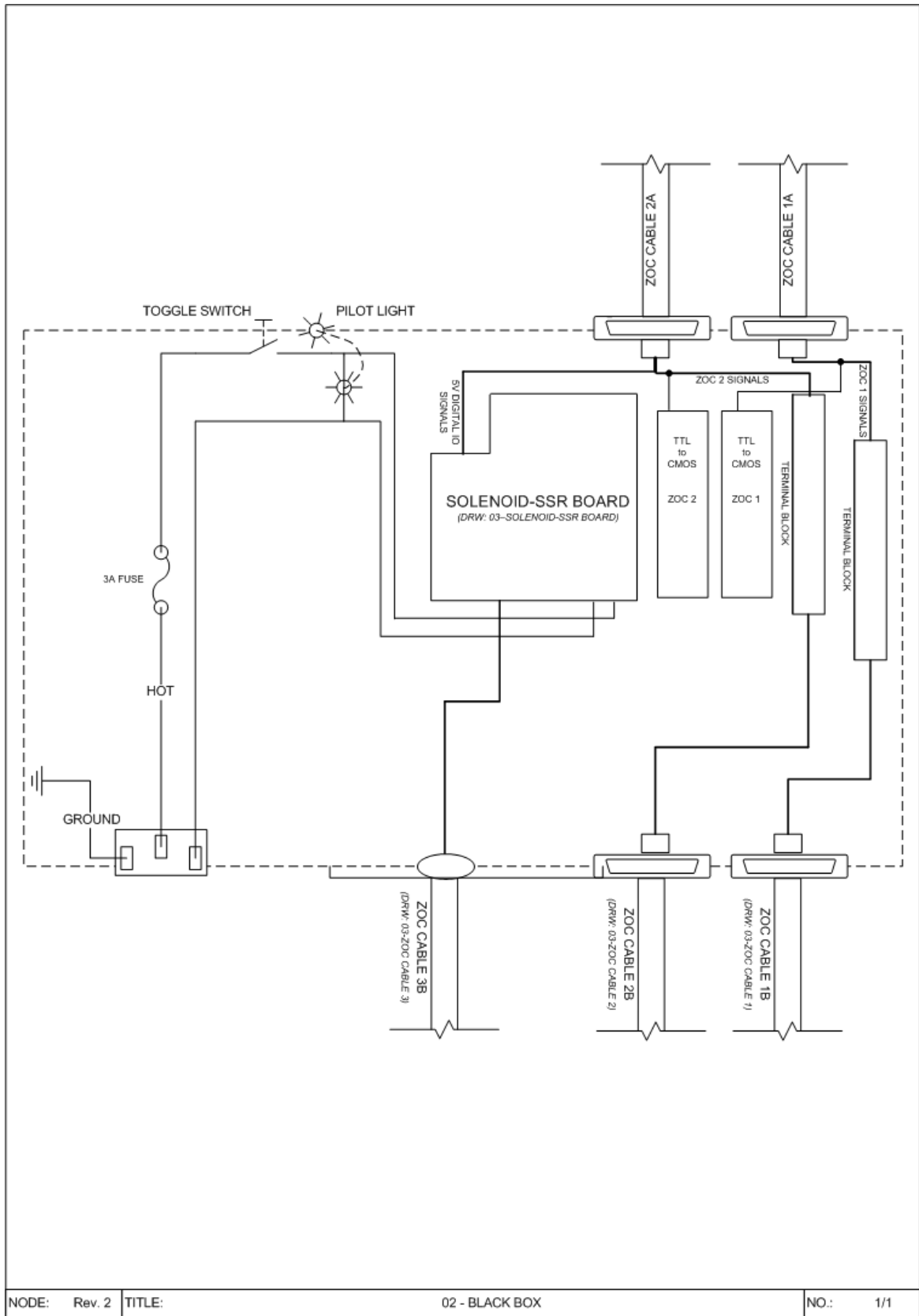


Figure B.5 Electrical housing for ZOC33 hardware.

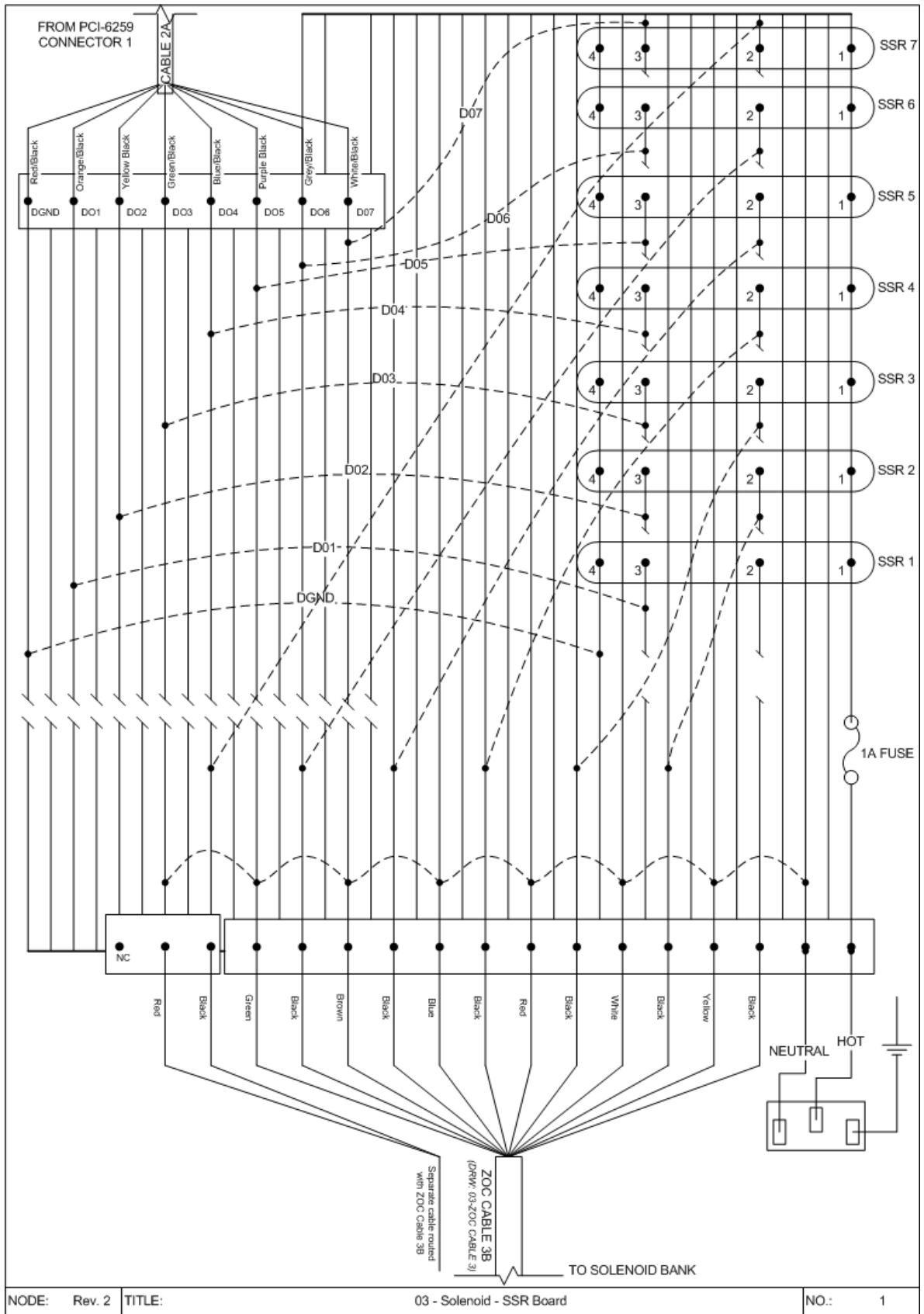


Figure B.6 Solid state relay board for ZOC33 operation mode selection.

Appendix C: MATLAB Code

The adaptive wall strategy is outlined as a flow chart in Fig. C.1. The execution of the adaptive wall strategy relies on a computer code written in MATLAB. The core of the strategy is found in the “WAS_main.m” program, which utilizes several sub-functions. The source code for the main program and sub-functions are included in this Appendix. In addition to the main program, the program which determines the ASW configuration wall contour (ASW.m) and the program which determines jack locations (SET_JACK.m) are included.

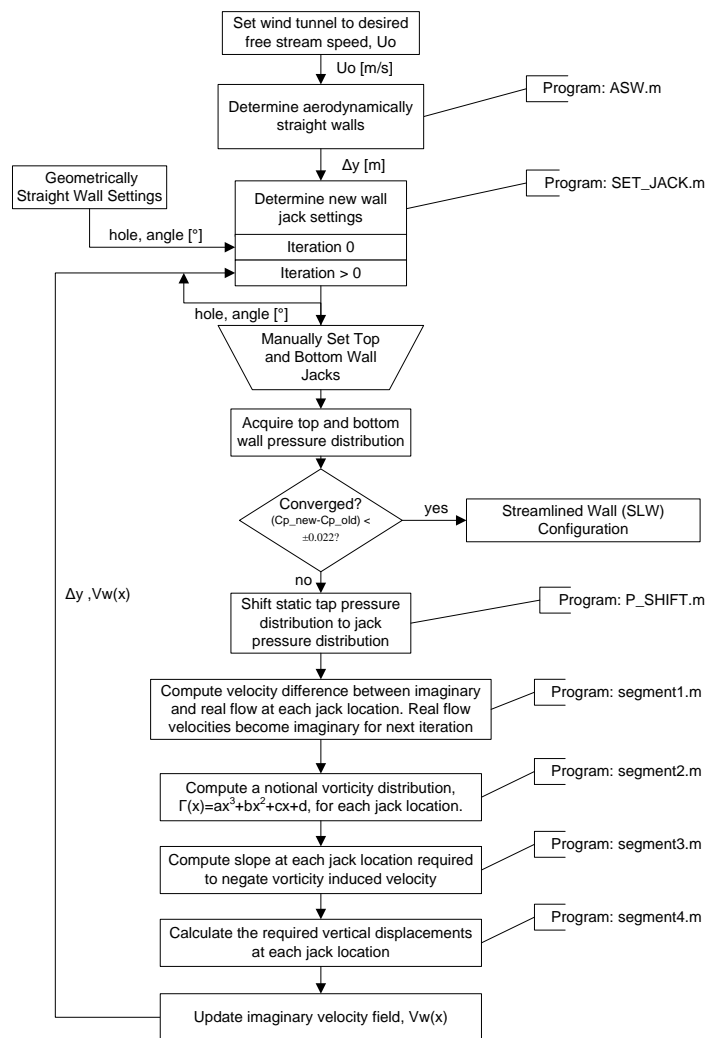


Figure C.1 Flow chart of wall adaptation strategy.

```

%-----WAS_main-----

%Goal: This is the main program which runs the "Predictive Wall adjustment
Strategy for Two-Dimensional Flexible Walled Adaptive Wind Tunnel" by Wolf
and Goodyer. NASA CR-181635

%Author: Michael Bishop
%Created: Feb 4, 2009

function imag_vel = WAS(Uo, XJACK, XTAP)

move1 = 10; %first jack available for streamlining
moveN = 32; %last jack available for streamlining
nadj = move1-3;
NOCPT = (moveN - move1 + 1) + 4;
NCPT1 = NOCPT - 2;
NCPT2 = NOCPT - 3;
NCPT3 = NOCPT - 4;
ycontrac = 181.68; %displacement required to get to straight walls in core
%-----
%-----SCALING FACTORS -----
SF = 0.8;
CPLF = 0.35;
%Note: scaling and coupling factors are for the top and bottom walls are
%assumed to be the same

%-----Cp VALUES-----
%Read in pressure data from roof
cp_roof = input('Please enter file name of CURRENT ROOF pressure data:
','s');
g_roof=xlsread(cp_roof);
N_roof = length(g_roof);
for i=1:N_roof
    TWCp(i) = g_roof(i,3);
end

%Read in pressure data from floor
cp_floor = input('Please enter file name of CURRENT FLOOR pressure data:
','s');
g_floor=xlsread(cp_floor);
N_floor = length(g_floor);
for i=1:N_floor
    BWCp(i) = g_floor(i,3);
end

%-----
%Translate the pressures measured at each tap location to pressures
located at each jack location.
TOPWP = P_SHIFT(XJACK, XTAP, TWCp);
BOTWP = P_SHIFT(XJACK, XTAP, BWCp);

%Adjust the Cp values for the first two dummy jacks to be equal to
%CP(move1) and the last two dummy jacks to be equal to CP(moveN)
for i=1:2
    TOPWP(move1-i) = TOPWP(move1);
    TOPWP(moveN+i) = TOPWP(moveN);
end

```

```

        BOTWP(move1-i) = BOTWP(move1);
        BOTWP(moveN+i) = BOTWP(moveN);
end
%-----SEGMENT 1-----
%Compute velocity differences and store imaginary velocities for the next
%iteration at each computing point

%Prompt user for file location of current imaginary velocities
input_file = input('Please enter file name of CURRENT imaginary velocites:
','s');
output_file = input('Please create file name for NEW imaginary velocites:
','s');

segment1_output = segment1(Uo, TOPWP, BOTWP, NOCPT, nadj, SF, CPLF, input_file,
output_file);

%formatting the output data
for i=1:NOCPT
    TWVDIFF(i) = segment1_output(i,1);
    BWVDIFF(i) = segment1_output(i,2);
    iTWVEL_new(i) = segment1_output(i,3);
    iBWVEL_new(i) = segment1_output(i,4);
    TWVEL(i) = segment1_output(i,5);
    BWVEL(i) = segment1_output(i,6);
    E_roof(i) = segment1_output(i,7);
    E_floor(i) = segment1_output(i,8);
end

%-----SEGMENT 2-----
%Computes a piecewise vorticity distribution at every computing point by
%using the velocity difference at the current computing point as well as
%the velocity difference at the next 3 adjacent downstream computing
points
%The coefficients of the least squares cubic curve fit is outputted to the
%matrix CUBCOE

segment2_output = segment2(TWVDIFF, BWVDIFF, XJACK, NCPT2, nadj);
CUBCOE = segment2_output;

%-----SEGMENT 3-----
%Compute the required change in slope of the top and bottom wall to negate
%the vorticity induced velocity which is locally normal to the wall. The
%required change in slopes are calculated at each mid-jack location.

%Calculate the midjack locations. At each midjack location, the required
%change in slope is calculated. The first midjack point is equal to the
%anchor point (i.e. jack 8)
XMIDJ(1) = XJACK(move1-1);
for i=2:NCPT1
    XMIDJ(i) = (XJACK(i+nadj)+XJACK(i+1+nadj))/2;
end

segment3_output = segment3_wolf(CUBCOE, XJACK, XMIDJ, NCPT1, NCPT2, nadj);

```

```

%formatting the output data

for i=1:NCPT1
    TSLOPE(i) = segment3_output(i,1);
    BSLOPE(i) = segment3_output(i,2);
end
%-----SEGMENT 4-----
%Determines the required vertical displacement at each jack location based
%on the required change in slope at each mid-jack location

segment4_output = segment4(TSLOPE,BSLOPE,XJACK,XMIDJ,NCPT3,nadj,SF,CPLF);

%formatting the output data
for i=1: NCPT3
    TWMOV(i) = segment4_output(i,1);    %required vertical displacement[m]
    BWMOV(i) = segment4_output(i,2);    %required vertical displacement[m]
end

%-----SET JACK-----
%Based on required vertical displacements and current jack settings, this
%function determines the new jack configuration (HOLE and ANGLE ARM
%locations).
input_file = input('Please enter file name of CURRENT ROOF jack settings:
','s');
output_file = input('Please create file name for NEW ROOF jack settings:
','s');
jack_data_roof = SET_JACK_c_mod(XJACK,TWMOV, NCPT3, move1,moveN,
input_file, output_file);
input_file = input('Please enter file name of CURRENT FLOOR jack settings:
','s');
output_file = input('Please create file name for NEW FLOOR jack settings:
','s');
jack_data_floor = SET_JACK_c_mod(XJACK,BWMOV, NCPT3, move1,moveN,
input_file, output_file);

%-----
%dy_mov = horzcat(iTWVEL, iBWVEL);
iTWVEL_new = reshape(iTWVEL_new, length(iTWVEL_new), 1);
iBWVEL_new = reshape(iBWVEL_new, length(iBWVEL_new), 1);
imag_vel = horzcat(iTWVEL_new, iBWVEL_new);

%-----CREATE PLOTS-----

set(0,'Units','pixels') ;
scnsize = get(0,'ScreenSize');
H = scnsize(4);
W = scnsize(3);

pos1 = [25, H/2-50, W/3.3, H/2.3];

```

```

figure('Name', 'Cp', 'position', pos1);
hold on
plot(XTAP, TWCp, 'Marker','^','DisplayName','Roof');
plot(XTAP, BWCp, 'Marker','v','DisplayName','Floor');
ymaxmin = y_limit(TWCp, BWCp);
plot_cylinder(0.089, ymaxmin(2), ymaxmin(1));
ylim(ymaxmin);
legend('show');
xlabel('x [m]');
ylabel('Cp');
title('Cp Plot');
grid('on');
hold off

pos1 = [25+W/3, 50, W/3.3, H/2.3];
figure('Name', 'Real Side Velocity', 'position', pos1);
hold on
%N = NOCPT
%computed at jack locations
for i=1:NOCPT
    x_NOCPT(i) = XJACK(nadj+i);
end
plot(x_NOCPT, TWVEL, 'r', 'Marker','^','Marker','^',
'DisplayName','Roof');
plot(x_NOCPT, BWVEL, 'b','Marker','v', 'DisplayName','Floor');
ymaxmin = y_limit(TWVEL, BWVEL);
plot_cylinder(0.089, ymaxmin(2), ymaxmin(1));
ylim(ymaxmin);
legend('show');
xlabel('x [m]');
ylabel('u/Uo');
title('Real Side Velocity');
grid('on');
hold off

pos2 = [25+W/3, H/2-50, W/3.3, H/2.3];
figure('Name', 'Velocity Difference', 'Position', pos2);
hold on
%computed at jack locations
%N = NOCPT
plot(x_NOCPT, TWVDIFF, 'r', 'Marker','^', 'DisplayName','Roof');
plot(x_NOCPT, BWVDIFF, 'b','Marker','v', 'DisplayName','Floor');
ymaxmin = y_limit(TWVDIFF, BWVDIFF);
plot_cylinder(0.089, ymaxmin(2), ymaxmin(1));
ylim(ymaxmin);
legend('show');
xlabel('x [m]');
ylabel('Velocity Diff');
title('Velocity Difference');
grid('on');
hold off

pos3 = [25+2*W/3,H/2-50, W/3.3, H/2.3];
figure('Name', 'Wall Slope', 'Position', pos3);
hold on
%computed at midjack locations

```

```

plot(XMIDJ, TSLOPE, 'r', 'Marker','^', 'DisplayName','Roof');
plot(XMIDJ, BSLOPE, 'b', 'Marker','v', 'DisplayName','Floor');
ymaxmin = y_limit(TSLOPE, BSLOPE);
plot_cylinder(0.089, ymaxmin(2), ymaxmin(1));
ylim(ymaxmin);
legend('show');
xlabel('x [m]');
ylabel('WALL SLOPE');
title('Required Slope Change');
grid('on');
hold off

```

```

pos4 = [25, 50, W/3.3, H/2.3];
figure('Name', 'Y Displacment', 'Position', pos4);
hold on
%N=NCPT3
for i=1:NCPT3
    x_NCPT3(i) = XJACK(i+nadj+1);
end

```

```

plot(x_NCPT3, TWMOV, 'r', 'Marker','^', 'DisplayName','Roof');
plot(x_NCPT3, BWMOV, 'b', 'Marker','v', 'DisplayName','Floor');
ymaxmin = y_limit(TWMOV, BWMOV);
plot_cylinder(0.089, ymaxmin(2), ymaxmin(1));
ylim(ymaxmin);
xlim([0,6]);
legend('show');
xlabel('x [m]');
ylabel('Y Displacement [m]');
title('Required Wall Displacement');
grid('on');
hold off

```

```

pos2 = [25+W/3, H/2-50, W/3.3, H/2.3];
figure('Name', 'Wall Setting Error', 'Position', pos2);
hold on
%computed at jack locations
%N = NOCPT
plot(x_NOCPT, E_roof, 'r', 'Marker','^', 'DisplayName','Roof');
plot(x_NOCPT, E_floor, 'b', 'Marker','v', 'DisplayName','Floor');
ymaxmin = y_limit(E_roof, E_floor);
plot_cylinder(0.089, ymaxmin(2), ymaxmin(1));
ylim(ymaxmin);
legend('show');
xlabel('x [m]');
ylabel('E');
title('Wall Setting Error');
grid('on');
hold off

```

```

%-----SEGMENT 1-----
%Goal: The purpose of this segment is to compute the real and imaginary
%velocities at each of the computing points (i.e. jack locations).

%This function is written so that it can be common to all wall
%configurations

%Author:      Mike Bishop
%Created:     January 29, 2009
%Date Modified: April 8, 2009: Updated code to read and write iVEL

%-Inputs-:
%Uo           <--Free Stream Velocity
%XJACK(i)     <--Array of streamwise (x) jack locations [m]
%TOPWP(i),BOTWP(i) <--Array of Cp values @ each computing point
%iTWVEL(i),iBWVEL(i)<--Array of imaginary velocities @ each computing
point

%-Outputs-:
%TWVDIFF(i), BWVDIFF(i) <--Array of notional vorticities
%iTWVEL(i),iBWVEL(i)   <--Array of new imaginary velocities

%-----

function segment1_output = segment1(Uo,TOPWP,BOTWP,NOCPT, nadj,SF,CPLF,
input_file, output_file)

%read imaginary velocity file and populate the imaginary velocity arrays
g_in=xlsread(input_file);
for i=1:NOCPT
    iTWVEL(i) = g_in(i,1);
    iBWVEL(i) = g_in(i,2);
end

%Function Constants
rou = 1.2;                %kg/m3
dyn_p = 0.5*rou*Uo^2;    %dynamic pressure

for i = 1: NOCPT

    %Top Wall Calcs
    TW_Cp = TOPWP(i+nadj);    %pressure coefficient
    TWVEL(i) = sqrt(1-TW_Cp); %calculate real normalized
velocity
    TWVDIFF(i) = TWVEL(i) - iTWVEL(i); %diff. b/w real and imag velocity

    %Bottom Wall Calcs
    BW_Cp = BOTWP(i+nadj);    %pressure coefficient
    BWVEL(i) = sqrt(1-BW_Cp); %calculate real velocity
    BWVDIFF(i) =iBWVEL(i) - BWVEL(i); %diff. b/w imag and real velocity

    %Calculate the Imaginery Velocity with integrated Scaling and Coupling
    %--Scaling Factors--
    iTWVEL_S(i) = iTWVEL(i) + SF*(TWVDIFF(i)/2);

```

```

    iBWVEL_S(i) = iBWVEL(i) - SF*(BWVDIFF(i)/2);

    %--Coupling Factors--
    iTWVEL_C(i) = iTWVEL_S(i) + CPLF*(iBWVEL_S(i) - BWVEL(i));
    iBWVEL_C(i) = iBWVEL_S(i) + CPLF*(iTWVEL_S(i) - TWVEL(i));
end

%calculate the average wall setting error, Eavg
Esum_roof =0;
Esum_floor = 0;
for i=1: NOCPT
    Cp_real_roof = 1 - (TWVEL(i))^2;
    Cp_imag_roof = 1 - (iTWVEL(i))^2;
    Cp_real_floor = 1 - (BWVEL(i))^2;
    Cp_imag_floor = 1 - (iBWVEL(i))^2;
    E_roof(i) = abs(Cp_real_roof-Cp_imag_roof);
    Esum_roof = Esum_roof + E_roof(i);
    E_floor(i) = abs(Cp_real_floor-Cp_imag_floor);
    Esum_floor = Esum_floor + E_floor(i);
end
Eavg_roof = Esum_roof/NOCPT;
Eavg_floor = Esum_floor/NOCPT;
'The average roof setting error is:',Eavg_roof
'The average floor setting error is:', Eavg_floor

%Set the new imaginary velocities for the next iteration
iTWVEL = iTWVEL_C;
iBWVEL = iBWVEL_C;

%Output data to WAS.m
TWVDIFF = reshape(TWVDIFF, NOCPT, 1);
BWVDIFF = reshape(BWVDIFF, NOCPT, 1);
iTWVEL = reshape(iTWVEL, NOCPT, 1);
iBWVEL = reshape(iBWVEL, NOCPT, 1);
TWVEL = reshape(TWVEL, NOCPT, 1);
BWVEL = reshape(BWVEL, NOCPT, 1);
E_roof = reshape(E_roof, NOCPT, 1);
E_floor = reshape(E_floor, NOCPT,1);

%Send new imaginary velocities to a file for use in next iteration
g_out = horzcat(iTWVEL, iBWVEL);
xlswrite(output_file,g_out);

segment1_output = horzcat(TWVDIFF, BWVDIFF, iTWVEL, iBWVEL, TWVEL, BWVEL,
E_roof, E_floor);

%eof

```

```

%-----SEGMENT 2-----
% Goal: The goal of this segment is to compute a piecewise vorticity
%       distribution at every computing point by using the velocity
%       difference at the current computing point as well as the velocity
%       difference at the next 3 adjacent downstream computing points. A
%       least squares cubic curve is determined for each piecewise
%       vorticity distribution, and the cubic coefficients are stored into
%       a matrix for use in Segment 3.
%Author:   Mike Bishop
%Created:  January 29, 2009

%-Inputs-:
%TWVDIFF(i), BWVDIFF(i)    <--Array of notional vorticities
%XJACK(i)                  <--Array of streamwise (x) jack locations
%-Outputs-:
%CUBCOE(i,j)              <--Matrix of cubic coefficients
%-----
function segment2_output = segment2(TWVDIFF,BWVDIFF, XJACK, NCPT2, nadj)

for iL=1:NCPT2
    i = iL - 1;
    %load four sets of xjack locations and vdiff's
    for j=1:4
        x(j) = XJACK(i+j+nadj);
        TW_vor(j) = TWVDIFF(i+j);
        BW_vor(j) = BWVDIFF(i+j);

    end

    %call function to compute least squares cubic curve fit
    %vor = ax^3 + bx^2 + cx +d
    coeff = my_cubic(x, TW_vor);
    d = coeff(1);
    c = coeff(2);
    b = coeff(3);
    a = coeff(4);
    CUBCOE(iL, 1)= d;
    CUBCOE(iL, 2)= c;
    CUBCOE(iL, 3)= b;
    CUBCOE(iL, 4)= a;

    coeff = my_cubic(x, BW_vor);
    d = coeff(1);
    c = coeff(2);
    b = coeff(3);
    a = coeff(4);
    CUBCOE(iL, 5)= d;
    CUBCOE(iL, 6)= c;
    CUBCOE(iL, 7)= b;
    CUBCOE(iL, 8)= a;
end

segment2_output = CUBCOE;
%eof

```

```

%-----SEGMENT 3-----
% Goal: The goal of this segment is to compute the required change in
% slope at each midjack location. First the piecewise vorticity
% distributions are integrated to determine the local induced velocity %at
% each midjack locations. The induced velocity is normal to the wall. %The
% required change in slope to negate the vorticity induced velocity %is then
% calculated and stored in an array to be used in Segment 4.

%Author:    Michael Bishop
%Created:   January 29, 2009

%-Inputs-:
%CUBCOE(i,j)    <--Matrix of cubic coefficients
%XJACK(i)       <--Array of streamwise (x) jack locations

%-Outputs-:
%TSLOPE(i)     <--Req'd change in slope at each top wall midjack location
%BSLOPE(i)     <--Req'd change in slope at each bottom. wall midjack
location

%-----
function segment3_output =
segment3_wolf(CUBCOE,XJACK,XMIDJ,NCPT1,NCPT2,nadj)

TSLOPE(1) = 0; %set the slope equal to zero at the anchor location
BSLOPE(1) = 0;
length(CUBCOE);
for j=2:NCPT1
    X0 = XMIDJ(j);
    TW_velsum = 0;
    BW_velsum = 0;
    X0SQ = X0^2;
    X0CUB = X0^3;
    for i=1:NCPT2
        %limits of integration
        X1 = XJACK(i+1+nadj+1);
        X2 = XJACK(i+2+nadj+1);

        %-----TOP WALL-----
        d = CUBCOE(i, 1);
        c = CUBCOE(i, 2);
        b = CUBCOE(i, 3);
        a = CUBCOE(i, 4);

        %integrate the current vorticity patch
        X2SQ = X2*X2;
        X1SQ = X1*X1;
        SUM0 = d + c*X0 + b*X0SQ + a*X0CUB;
        X3 = abs(X2-X0)/abs(X1-X0);
        X4 = log(X3);
        SUM1 = (c + b*X0 + a*X0SQ)*(X2-X1);
        SUM2 = (b + a*X0)*(X2SQ - (X1SQ))/2;
        SUM3 = a*((X2SQ*X2) - (X1SQ*X1))/3;
        TW_velsum = TW_velsum + SUM0*X4 + SUM1 + SUM2 + SUM3;
    end
end

```

```

%-----BOTTOM WALL-----
d = CUBCOE(i, 5);
c = CUBCOE(i, 6);
b = CUBCOE(i, 7);
a = CUBCOE(i, 8);

%integrate the current vorticity patch
SUM0 = d + c*X0 + b*X0SQ + a*X0CUB;
X3 = abs(X2-X0)/abs(X1-X0);
X4 = log(X3);
SUM1 = (c + b*X0 + a*X0SQ)*(X2-X1);
SUM2 = (b + a*X0)*((X2SQ) - (X1SQ))/2;
SUM3 = a*((X2SQ*X2) - (X1SQ*X1))/3;
BW_velsum = BW_velsum + SUM0*X4 + SUM1 + SUM2 + SUM3;
end

%slope at the current midjack location
TSLOPE(j) = TW_velsum/(2*pi);
BSLOPE(j) = BW_velsum/(2*pi);
end

% TSLOPE(40) = 0;
% BSLOPE(40) = 0;

TSLOPE = reshape(TSLOPE, NCPT1, 1);
BSLOPE = reshape(BSLOPE, NCPT1, 1);

segment3_output = horzcat(TSLOPE, BSLOPE);

%eof

```

```

%-----SEGMENT 4-----
% Goal: The goal of this segment is compute the vertical displacements
% required at each computing location (jack location) based on the %slopes
%calculated at each mid-jack location from Segment 3.

%Author:    Michael Bishop
%Created:   January 30, 2009

%-Inputs-:
%TSLOPE(i)    <--Req'd change in slope at each top wall midjack location
%BSLOPE(i)    <--Req'd change in slope at each bottom. wall midjack
location
%XJACK(i)     <--Array of streamwise (x) jack locations
%XMIDJ(i)     <--Array of midjack locations
%-Outputs-:
%TWMOV(i)     <--Req'd change in displacement at each top wall jack
%BWMOV(i)     <--Req'd change in displacement at each bottom wall jack

%-----

function segment4_output = segment4(TSLOPE,BSLOPE,XJACK,XMIDJ,NCPT3,nadj,
SF, CPLF)
TMOV = 0;
BMOV = 0;

for i=1:NCPT3
    i1 = i+1;
    i2 = i+2;

    %fill array of three adjacent midjack locations
    k=i-1;
    for j=1:3
        X(j) = XMIDJ(k+j);
        TW_dy_dx(j) = TSLOPE(k+j);
        BW_dy_dx(j) = BSLOPE(k+j);
    end

    %quadratic curve fit for three adjacent MIDJ locations
    %coeff = (a,b,c)
    %dy_dx = ax^2+bx+c;
    TW_coeff = my_quadratic(X, TW_dy_dx);
    BW_coeff = my_quadratic(X, BW_dy_dx);

    %integrate the quadratic to determine vertical displacements
    %limits of integration
    X1 = XJACK(i1+nadj);
    X2 = XJACK(i2+nadj);
    %---TOP WALL---
    a = TW_coeff(1);
    b = TW_coeff(2);
    c = TW_coeff(3);
    TW_dis = (a*X2^3)/3+(b*X2^2)/2+(c*X2) - ((a*X1^3)/3+(b*X1^2)/2+(c*X1));

    %---BOTTOM WALL---

```

```

a = BW_coeff(1);
b = BW_coeff(2);
c = BW_coeff(3);
BW_dis = (a*X2^3)/3+(b*X2^2)/2+(c*X2)-((a*X1^3)/3+(b*X1^2)/2+(c*X1));

TMOV = TMOV + TW_dis;
BMOV = BMOV + BW_dis;

%Scale the jack movement demands using the scaling factors.
STMOV = SF*TMOV;
SBMOV = SF*BMOV;

%Couple the jack movement demand using the coupling factors.
TWMOV(i) = STMOV+(CPLF*SBMOV);
BWMOV(i) = SBMOV+(CPLF*STMOV);
end

TWMOV = reshape(TWMOV, NCPT3, 1);
BWMOV = reshape(BWMOV, NCPT3, 1);

segment4_output = horzcat(TWMOV, BWMOV);
%eof

```

```

%-----SET JACK-----

%Goal: The goal of this program is to output:
%      1) New Hole Positions
%      2) New Angle Arm Positions

%Author: Michael Bishop
%Created: June 19, 2008
%Modified: January 30, 2009: Updated radius of pinion
%Modified: March 23, 2009: Updated code
%Modified: April 7, 2009: Updated JACK settings to be from file
%Modified: May 20, 2009: Corrected small deflection bug

%Note: 125.58 [mm] of jack movement per jack shaft revolution

%-Inputs-:
%XJACK(i)      <--Array of streamwise (x) jack locations
%TWMOV(i)      <--Req'd change in displacement at each top wall jack
%BWMOV(i)      <--Req'd change in displacement at each bottom wall jack
% --- Note: TWMOV or BWMOV is represented as "dy" below ---

%y(i)          <--Current wall location
%hole(i)       <--Current hole the pinion is set to
%aa(i)         <--Current angle the angle arm is set to
% --- Note: CW=1 denotes CW rotation, CW=0 denotes CCW rotation ---

%-Outputs-:
%TWMOV(i)      <--Req'd change in displacement at each top wall jack
%BWMOV(i)      <--Req'd change in displacement at each bottom wall jack
%CW(i)         <--Direction of pinion movement (clockwise turn ==> CW=1)
%turn(i)       <--Number of complete revolutions
%hole(i)       <--New hole for which the shear pin should be place
%aa(i)         <--New setting for the angle arm position

function cw_turn_hole_angle = SET_JACK_c_mod(XJACK,dy_core, NCPT3, move1,
moveN, input_file, output_file)

%prompt user for file location containing current jack settings
g=xlsread(input_file);
N = length(g);
for i=1:N
    x(i) = g(i,1);
    y(i) = g(i,2);
    OH(i) = g(i,5);
    OAA(i) = g(i,6);
end
rp = 0.01999; %[m] radius of the pinion gear. 125.58[mm] per 1 revolution.

for i=1:(move1-1)
    y_new(i) = y(i);
end

for i=move1:moveN
    y_new(i) = y(i) + dy_core(i-move1+1);
end

```

```

for i=39:48
    y_new(i) = y(i);
end

xjack = XJACK;

yNtop = y_new(moveN);
xNtop = xjack(moveN);
mNtop = (yNtop - y_new(moveN-1))/(xNtop-xjack(moveN-1));
blend0 = 39;
blend1 = 40;
blend2 = 41;
m42top = (y_new(blend2) - y_new(blend1))/(xjack(blend2) - xjack(blend1));

%populate the 't' matrix
t(1, 1) = 1;
t(1, 2) = xNtop;
t(1, 3) = xNtop * xNtop;
t(1, 4) = t(1, 3) * xNtop;
t(2, 1) = 1;
t(2, 2) = xjack(blend1);
t(2, 3) = xjack(blend1) * xjack(blend1);
t(2, 4) = t(2, 3) * xjack(blend1);
t(3, 1) = 0;
t(3, 2) = 1;
t(3, 3) = 2 * xNtop;
t(3, 4) = 3 * xNtop * xNtop;
t(4, 1) = 0;
t(4, 2) = 1;
t(4, 3) = 2 * xjack(blend1);
t(4, 4) = 3 * xjack(blend1) * xjack(blend1);
%populate the 't' matrix
c = [yNtop; y_new(blend1); mNtop; m42top];

z = t\c;
%compute the y location of the blended region (JACKS 33-->39)
for i=(moveN+1):blend0
    x = xjack(i);
    y_new(i) = z(1) + z(2)*x + z(3)*x^2+ z(4)*x^3;
end

%calculate the required dy movement at every jack location
for i=1:48
    dy(i) = y_new(i) - y(i);
end

for i = 1: 48

    %calcuatue the total pinion angle required to translate the rack dy
    beta = (dy(i)/rp)*180/pi; %[deg]

    if beta ~ 0;

```

```

%determine if the pinion has to move CW or CCW
beta = beta + OAA(i); %reset the arm angle to zero degrees
if beta > 0
    CW(i)=1;
    % beta = beta + OAA(i); %reset the arm angle to zero degrees
elseif beta < 0
    CW(i) = 0;
    %beta = beta + OAA(i); %reset the arm angle to zero degrees
end

turn(i) = floor(abs(beta)/360); %total number of full revolutions
theta = round((abs(beta) - turn(i)*360)/15)*15;
alpha = abs(beta) - theta - turn(i)*360;

if CW(i) == 1
    anglearm(i) = alpha;
    hole(i) = OH(i) - theta/15;
    if hole(i) < 0
        hole(i) = hole(i) + 24; %map back to hole 0-->23
    end
else
    anglearm(i) = alpha*-1;
    hole(i) = OH(i) + theta/15;
    if hole(i)>=24
        hole(i) = hole(i) -24;
    end
end
else
    CW(i) = 0;
    turn(i)=0;
    hole(i)=OH(i);
    anglearm(i)=OAA(i);
end
end

x_new = reshape(xjack, 48, 1);
y_new = reshape(y_new, 48, 1);
CW = reshape(CW, 48, 1);
turn = reshape(turn, 48, 1);
hole = reshape(hole, 48, 1);
anglearm = reshape(anglearm, 48, 1);

cw_turn_hole_angle = [x_new y_new CW turn hole anglearm];
xlswrite(output_file,cw_turn_hole_angle);

%eof

```

```

%-----ASW-----
%Goal: The goal of this program is to compute contour of the roof and
%floor that give aerodynamically straight walls. Aerodynamically straight
%walls are defined such that the negative pressure gradient in the tunnel
%test section is removed. A 1/7th power law boundary layer is assumed. An
%empirical correction factor determined by Sumner (1994) is used.

%Note: Displacement thickness is calculated using a using a 1/7th power
%      law velocity profile for a turbulent boundary layer on a flat
%      plate.

%Author: Michael Bishop
%Created: Feburary 2, 2009

%-Inputs-:
%XJACK(i)      <--Array of streamwise (x) jack locations [m]
%Uo            <--Free Stream Velocity [m/s]

function y_cont = ASW(XJACK)

%-----PROMPT USER FOR INPUTS-----
wall_selection = input('roof or floor?: ', 's')
roof = strcmp(wall_selection, 'roof');
if (roof == 1)
    asw_mult = 1;
    gsw_mult = -1;
else
    asw_mult = -1;
    gsw_mult = 1;
end

asw_gsw = input('asw or gsw?: ', 's')
ASW = strcmp(asw_gsw, 'asw');

Uo = input('please enter the freestream speed in [m/s]: ')

%-----
move1 = 13; %first jack available for wall adaptation
moveN = 32; %last jack available for wall adaptation ASW_c

set(0, 'Units', 'pixels') ;
scnsize = get(0, 'ScreenSize');
H = scnsize(4);
W = scnsize(3);
%-----CONTRACTION-----
%all y() coordinates (in [mm]) below are relative to wall displacements
%from straight walls in the nominal configuration. i.e. Configuration A,
%i.e., "Nominal Configuration"

ycontrac = 181.68; %displacement required to get to straight walls in core
scale_mult = 0.85682; %multiplication factor to scale contraction to new
ycontrac
y(1) = 0*scale_mult;
y(2) = 1.0849*scale_mult;

```

```

y(3) = 8.6795*scale_mult;
y(4) = 29.2933*scale_mult;
y(5) = 69.4359*scale_mult;
y(6) = 124.3566*scale_mult;
y(7) = 164.8155*scale_mult;
y(8) = 190.3967*scale_mult;
y(9) = 206.0863*scale_mult;
y(10) = 212.0398*scale_mult;
y(11) = ycontrac;
y(12) = ycontrac;
y(13) = ycontrac;

%-----STRAIGHT WALLS-----
for i=move1:moveN
    y(i) = ycontrac;
end
%-----DIFFUSER-----
y(48) = 15.79;
y(47) = 31.8079;
y(46) = 47.8258;
y(45) = 63.8437;
y(44) = 79.8615;
y(43) = 95.8794;
y(42) = 111.8973;
y(41) = 127.9152;
y(40) = 143.9331;
y(39) = 159.951;
y(38) = 175.9689;
%=====
%-----ASW-----
%=====
if (ASW==1)
    factor = 1.65;
    norigin = 8;
%-----CONTRACTION-----
    %no change from XJACK(1) through XJACK(norigin-1)
    for i=1:(norigin-1)
        y(i) = y(i)*gsw_mult;
        x(i) = XJACK(i);
    end
%-----CORE-----
    %calculate the displacement thickness based on distance from the
virtual
    %norigin
    for i = norigin: moveN
        delstar = (factor*0.004118*(XJACK(i) -
XJACK(norigin))^(6/7))/Uo^(1/7)*1000;
        y(i) = y(i)*gsw_mult + delstar*asw_mult;
        x(i) = XJACK(i);
    end
%-----DIFFUSER-----
    for i=40:48
        y(i) = y(i)*gsw_mult;
        x(i) = XJACK(i);
    end
else
%=====

```

```

%-----GSW-----
%=====

%-----CONTRACTION+CORE-----
    for i=1:moveN
        y(i) = y(i)*gsw_mult;
    end
%-----DIFFUSER-----
    for i=40:48
        y(i) = y(i)*gsw_mult;
        x(i) = XJACK(i);
    end
end
%=====
%-----ASW+GSW-----
%=====
%-----BLEND REGION-----
%This algorithm for the blended region was developed by Sumner (1994),
%'EMPTY-C.BAS' It is simply translated into MATLAB code below.

xjack = XJACK;

yNtop = y(moveN);
xNtop = xjack(moveN);
mNtop = (yNtop - y(moveN-1))/(xNtop-xjack(moveN-1));
blend0 = 39;
blend1 = 40;
blend2 = 41;
m42top = (y(blend2) - y(blend1))/(xjack(blend2) - xjack(blend1));

%populate the 't' matrix
t(1, 1) = 1;
t(1, 2) = xNtop;
t(1, 3) = xNtop * xNtop;
t(1, 4) = t(1, 3) * xNtop;
t(2, 1) = 1;
t(2, 2) = xjack(blend1);
t(2, 3) = xjack(blend1) * xjack(blend1);
t(2, 4) = t(2, 3) * xjack(blend1);
t(3, 1) = 0;
t(3, 2) = 1;
t(3, 3) = 2 * xNtop;
t(3, 4) = 3 * xNtop * xNtop;
t(4, 1) = 0;
t(4, 2) = 1;
t(4, 3) = 2 * xjack(blend1);
t(4, 4) = 3 * xjack(blend1) * xjack(blend1);
%populate the 't' matrix
c = [yNtop; y(blend1); mNtop; m42top];

z = t\c;
%compute the y location of the blended region (JACKS 33-->39)
for i=(moveN+1):blend0
    x = xjack(i);
    y(i) = z(1) + z(2)*x + z(3)*x^2+ z(4)*x^3;
end

```

```

%=====
%-----PLOTS-----
-
%=====
=
%convert displacements in [mm] to [m]
y = y/1000;

pos1 = [25, H/2-50, W/3.3, H/2.3];

if (ASW==1)
    figure('Name', 'Config C: ASW', 'position', pos1);
    hold on
    plot(XJACK, y, 'Marker','o');
    xlabel('x [m]');
    ylabel('y');
    title('Config-C: ASW');
    grid('on');
    hold off
else
    figure('Name', 'Config C: GSW', 'position', pos1);
    hold on
    plot(XJACK, y, 'Marker','o');
    xlabel('x [m]');
    ylabel('y');
    title('Config-C: GSW');
    grid('on');
    hold off
end
%-----
-
y_cont=y; %returns the required displacements [m]
%eof

```

```

%-----P_SHIFT-----
%Goal: The goal of this program is to transform the pressure coefficient
%measurements (Cp) from the 70 streamwise pressure taps to the locations
of
%48 jack locations.

%Author: Michael Bishop
%Created: Feb 4, 2009

%-Inputs-:
%XJACK(i)      <--Array of streamwise (x) jack locations [m]
%XTAP(i)       <--Array of streamwise (x) pressure tap locations [m]
%CP_TAP(i)     <--Array of pressure measurements at each tap location

%-Outputs-:
%TOPWP(i),BOTWP(i) <--Array of Cp values located at each computing point

function P_JACK = P_SHIFT(XJACK, XTAP, CP_TAP)

NJ = length(XJACK) %total number of jacks
NT = length(XTAP) %total number of pressure taps

%Loop to calculate pressures at each jack location. The pressure values
%for the first two and last two jacks will be calculated individually at
%the end of function

for i=3:(NJ-2)

    search=1;
    k=i;
    %loop to find pressure tap location which is immediately downstream to
    %jack location "i". This location will be XTAP(k)
    while (search==1)
        if XJACK(i) > XTAP(k)
            search=1;
            k=k+1;
        else
            search=0;
        end
    end

    %use a cubic curve fit to determine a pressure distribution for jack
    %"i", using two taps upstream and two taps downstream of jack "i".

    for j=1:4
        x(j) = XTAP(k-2+j-1);
        y(j) = CP_TAP(k-2+j-1);
    end

    %call function to determine least squares cubic curve fit
    p_coeff = my_cubic(x,y);
    %P=ax^3+bx^2+cx+d
    P_JACK(i) = p_coeff(4)*XJACK(i)^3 + p_coeff(3)*XJACK(i)^2 +
    p_coeff(2)*XJACK(i) + p_coeff(1);
end

```

end

%Set static pressure coefficient (Cp) values for the first two and
%the last two jack stations. It is noted that the values at these
%x-locations will never be used by the Wall Adaptive Strategy (thus
%the values are not critical).

P_JACK(1) = CP_TAP(1);

P_JACK(2) = (CP_TAP(1)+CP_TAP(2))/2;

P_JACK(NJ) = CP_TAP(NT);

P_JACK(NJ-1) = (CP_TAP(NT-1)+CP_TAP(NT))/2;

%eof

Appendix D: Experimental Uncertainty Analysis

This appendix aims to estimate the uncertainty associated with the experimental measurements conducted for this investigation. The uncertainty analysis included is grouped as follows:

- i) Pressure and mean free-stream flow measurements
- ii) Hot-wire measurements
- iii) Velocity probe and cylinder pressure tap positioning

Pressure and Mean Free-stream Flow Measurements

An uncertainty analysis aims to estimate the error associated with experimental measurements, and the estimation of the precision error (S) and bias error (Bi) is required (Moffat, 1988). The contribution of these errors leads to the estimation of a total root mean square uncertainty ($U_{0.95}$) shown in Eq. D.1.

$$U_{0.95} = \sqrt{Bi^2 + (2S)^2} \quad (D.1)$$

The total uncertainty $U_{0.95}$ represents a 95% confidence level in the measurement; that is, the obtained measurement will be within $\pm U_{0.95}$ of the true value 95 times out of 100. The precision error (S) is statistical and is based on the standard deviation (σ) and number of sample (N) in the measurement data set as shown in Eq. D.2.

$$S = \frac{\sigma}{N} \quad (D.2)$$

The bias (Bi) is a fixed error mainly related to calibration (Bi_{CAL}) and probe (or tap) geometry and position (Bi_{PROBE}). The total bias error, which accounts for the individual bias errors (Moffat, 1988) is determined using Eq. D.3.

$$Bi = \sqrt{Bi_{CAL}^2 + Bi_{PROBE}^2} \quad (D.3)$$

The dynamic pressure of the free-stream velocity, wall pressure, and cylinder surface pressure were all measured using separate pressure transducers shown in Table D.1.

Table D.1 List of pressure transducers used in experiment.

Measurement	Pressure Transducer	Model No.	Pressure Range [Pa]
Dynamic pressure	Lucas Schaevitz	P3061-2WD	0-498
Cylinder pressure (d=0.089m)	All Sensors	1 INCH D2-4V MINI	0-249
Cylinder pressure (d=0.0423m)	Lucas Schaevitz	P3061-2WD	0-498
Wall pressure	Scanivalve	ZOC33 S- SENSOR	0-1245

The precision and bias errors associated with the corresponding measurements are shown in Table D.2. For all measurements in Table D.1, the analog output from the respective pressure transducer was sampled at 5000Hz for a duration of 20 seconds. Given the large sample size (N=100,000), the precision errors are significantly lower compared to the corresponding bias errors as shown in Table D.2. All calibration bias errors were based on the precision of the smallest division of the inclined manometer used in calibration and zero offset voltage drift measured at the start and end of each measurement. The uncertainty associated with positioning (i.e., yaw angle) and geometry of the static-pitot tube (for dynamic pressure measurements) was estimated to be 0.3% (Pope, 1966). From the work of Chue (1975), the uncertainty in mean pressure measurements associated with a pressure tap geometry is estimated to be 0.2%. The resulting bias errors, computed using Eq. D.3, as well as total uncertainties are summarized in Table D.2.

Table D.2 Total uncertainty associated with free-stream speed and pressure measurements.

Measurement	S	Bi	$U_{0.95}$
U_o [m/s]	0.000	0.213	0.213
C_p	0.001	0.022	0.022
C_{p_w}	0.000	0.022	0.022

Hot-wire Measurement Uncertainty

The uncertainties associated with hot-wire velocity measurements were determined based on the extensive evaluation by Kawall et al. (1983). Estimated error (ϵ) for mean and instantaneous velocities are included for both the normal and cross-wire hot-wire probes. Table D.3 shows the errors associated with measurements outside the wake, inside the wake near the cylinder ($x/d \leq 9$), and inside the wake away from the cylinder ($x/d > 9$). The error values in Table D.3 represent the total uncertainty (i.e., error due to turbulence intensity, calibration, and statistics). In general, the accuracy of velocity measurement via hot-wire depends on the level of turbulence intensity in the flow; the accuracy decreases as turbulence intensity increases. Thus, in the current study, the accuracy of the hot-wire measurements is the highest outside of the wake and lowest in the near wake of the cylinder. As shown in Table D.3, the normal-probe has less error in the near wake relative to the cross-wire probe for both mean and instantaneous velocities. The limitation of the normal probe, however, is that it cannot resolve the vertical velocity component that is present in the near wake (Fig. 5.12), and the associated added wire cooling from the vertical velocity component yields an over estimation of U . Due to this fact, the cross-wire probe was used simultaneously with the normal probe to utilize the desirable characteristics of both.

Table D.3 Error estimates for velocity measurements.

Type of Measurement	Probe	Relevant Figures	Error (%)
Mean streamwise velocity (outside wake)	Normal	A.2, A.4	2.1
	Cross-wire		2.2
Mean streamwise velocity (inside wake, $x/d \leq 9$)	Normal		5.2
	Cross-wire	5.4(a,b,c), 5.5(a,b,c), 5.6(a,b,c), 5.10, 5.11	10.8
Mean streamwise velocity (inside wake, $x/d > 9$)	Normal		2.9
	Cross-wire	5.5(a,b,c), 5.6(a,b,c)	4.8
Mean vertical velocity (outside wake)	Cross-wire		2.1
Mean vertical velocity (inside wake, $x/d \leq 9$)	Cross-wire	5.12(a,b,c)	48.0
Mean vertical velocity (inside wake, $x/d > 9$)	Cross-wire		3.9
RMS streamwise velocity (outside wake)	Normal		2.4
	Cross-wire		2.7
RMS streamwise velocity (inside wake, $x/d \leq 9$)	Normal	5.22(a,b,c)	3.4
	Cross-wire	5.13(a,b,c), 5.14(a,b,c), 5.15(a,b), 5.16, 5.17, 5.18	3.8
RMS streamwise velocity (inside wake, $x/d > 9$)	Normal		2.4
	Cross-wire	5.14(a,b,c), 5.15(a,b)	2.4
RMS vertical velocity (outside wake)	Cross-wire	5.19, 5.20, 5.21	2.6
RMS vertical velocity (inside wake, $x/d \leq 9$)	Cross-wire		14.1
RMS vertical velocity (inside wake, $x/d > 9$)	Cross-wire		5.3
Streamwise velocity (outside wake)	Pitot-static tube	4.7(a,b,c), 5.7, 5.8, 5.9	2.1

Velocity Probe and Cylinder Pressure Tap Positioning

The velocity probes (hot-wire probes and pitot-static tube) were positioned in streamwise (x), vertical (y), and spanwise (z) locations via an automated three-axis traverse mechanism. Motion in each axis was driven by direct current stepper motors controlled by stepper motor drives (Appendix B). The stepper motors for the spanwise and vertical axes were coupled to $\frac{1}{4}$ "-20 lead screws, while the streamwise motor was coupled to a $\frac{3}{4}$ "-6 lead screw. The stepper motor drives (Gecko G210) were configured in half-step mode, such that one motor pulse corresponds to 0.9° of angular movement. The control system was capable

of sending individual motor pulses, translating to 0.003175 mm and 0.01058 mm linear distance per pulse for the $\frac{1}{4}$ "-20 and $\frac{3}{4}$ "-6 lead screws, respectively. The linear distance per pulse represents the optimal precision of movement. To test the actual precision, each axis was programmed to move 100mm and the subsequent distance traveled was measured via a digital vernier caliper. This procedure was repeated five times for each axis. Results showed that the traverse was capable of positioning the velocity probe along the vertical and spanwise axis to within ± 0.1 mm and the streamwise axis to within ± 0.2 mm. It is expected that the difference between the actual accuracy versus the maximum achievable accuracy is due to motor shaft translation relative to the motor housing, attributable to thrust loads.

A precision digital protractor (PRO 360) was used to set the angular positioning of the cylinder static tap. The digital protractor was rigidly mounted to a flat-machined surface on the model support mechanism. The model support mechanism, concentrically connected to the cylinder axle via setscrews, was rotated by hand to the desired angle (θ). Based on manufacturers specifications, the digital protractor had an angular resolution of 0.1° , resulting in the accuracy of $\pm 0.1^\circ$ in the cylinder tap positioning.